

基于 $^{171}\text{Yb}^+$ - $^{138}\text{Ba}^+$ 离子阱系统的
量子信息科学研究

**Quantum information science with
trapped $^{171}\text{Yb}^+$ - $^{138}\text{Ba}^+$ ions**

(申请清华大学理学博士学位论文)

培 养 单 位 : 交叉信息研究院

学 科 : 物理学

研 究 生 : 王 鹏 飞

指 导 教 师 : Kim Kihwan (金奇奂)副教授

二〇二一年五月

**Quantum information science with
trapped $^{171}\text{Yb}^+$ - $^{138}\text{Ba}^+$ ions**

Thesis Submitted to

Tsinghua University

in partial fulfillment of the requirement

for the degree of

Doctor of Science

in

Physics

by

Wang Pengfei

Thesis Supervisor: Associate Professor Kihwan Kim

May, 2021

学位论文答辩委员会名单

答辩委员会名单

主席	尤力	教授	清华大学
委员	Kim Kihwan (金奇奂)	副教授	清华大学
	马雄峰	副教授	清华大学
	李颖	研究员	中国工程物理研究院
	袁骁	助理教授	北京大学
秘书	苏晓禄	助理研究员	清华大学

关于学位论文使用授权的说明

本人完全了解清华大学有关保留、使用学位论文的规定，即：

清华大学拥有在著作权法规定范围内学位论文的使用权，其中包括：（1）已获学位的研究生必须按学校规定提交学位论文，学校可以采用影印、缩印或其他复制手段保存研究生上交的学位论文；（2）为教学和科研目的，学校可以将公开的学位论文作为资料在图书馆、资料室等场所供校内师生阅读，或在校园网上供校内师生浏览部分内容；（3）按照上级教育主管部门督导、抽查等要求，报送相应的学位论文。

本人保证遵守上述规定。

（保密的论文在解密后遵守此规定）

作者签名： _____

导师签名： _____

日 期： _____

日 期： _____

摘要

相比于经典体系，量子体系具有很多神奇的性质，如量子相干性、量子纠缠、量子互文性等。这些由量子力学所揭示的客观世界的神奇性质大多源自于量子态叠加效应。量子态叠加效应使得任意量子态可以在一个量子体系中同时存在，或者说叠加在一起。当两个单比特量子态叠加在一起时，就牵涉到体系的量子相干性。当关联的多比特量子态叠加在一起时，就涉及到量子体系间的纠缠。自量子力学诞生起，量子态叠加究竟是相干叠加还是统计上的混合，也就是说测量结果是预先确定的还是在测量发生瞬间确定的，一直都是一个最基本的问题。针对这个问题，贝尔不等式提供了一种数学手段和实验方法来判断究竟哪种观点更符合客观事实。但是贝尔测试只能在类空间隔或者非定域性前提下进行验证。然而量子互文性可以在不要求类空间隔的情况下来验证量子的本质。本论文以 $^{171}\text{Yb}^+$ - $^{138}\text{Ba}^+$ 混合离子阱系统为实验平台，从实验的角度探索了量子相干性、量子纠缠和量子互文性。

对于量子相干性，我们首先研究了单个 $^{171}\text{Yb}^+$ 量子比特的退相干过程。然后通过抑制退相干将其相干时间延长到 1 小时以上，该成果相比于之前的最长相干时间记录提高了一个数量级。之前，单个 $^{171}\text{Yb}^+$ 量子比特的相干时间最长记录是 660 s，在这个基础上，我们明确了其限制因素主要为微波信号相位噪声，残余磁场涨落以及微波信号泄漏。我们针对各个因素对系统进行了改进，最终将量子比特相干时间提升到了 5500 秒。除了足够长的相干时间外，双比特纠缠操作对离子量子计算也至关重要。因此我们利用激光对两个离子进行操作，实现了 $^{171}\text{Yb}^+$ - $^{138}\text{Ba}^+$ 离子间保真度高达 98% 的双量子比特纠缠。最后，基于离子间的纠缠态，我们又对量子互文性进行了验证。实验中同时关闭了探测性漏洞以及兼容性/sharpness 漏洞，在实验上首次无漏洞地演示了可重复且无串扰 (repeatable and nondisturbing) 测量间的互文性关联。实验结果表明我们的量子测量具有高达 98.1% 的可重复性，而且互文不等式实现了 15 个标准差的违背，这些结果都完美验证了量子力学的正确性。我们的研究将有助于进一步加深人们对于量子力学的理解，也将推动量子信息科学相关应用的发展。

关键词：离子阱；量子信息科学；相干时间；量子互文性；量子计算

ABSTRACT

Compared with the classical system, the quantum system has some magic features, such as coherence, entanglement, and quantum contextuality. The magic features of nature revealed by quantum mechanics mainly result from the fundamental principle of quantum superposition. It means that any quantum states can exist simultaneously or can be superposed together. When two quantum states of a single qubit are superposed, the property is characterized as coherence. If correlated multi-qubit states are superposed, they are entangled. Since the birth of quantum mechanics, it has been the major fundamental problem whether the quantum superposition is indeed a coherent superposition or a statistical mixture, which is, the measurement results are predetermined or determined at the incident of measurement. Bell inequality provides the mathematical and experimental method to distinguish which scenario agrees with the real world. However, the Bell test reveals the quantum nature when the property of nonlocality or space-like separation exists. On the other hand, quantum contextuality can reveal the nature of such quantumness without the requirement of nonlocality. In this thesis, using two species of ions, $^{171}\text{Yb}^+$ and $^{138}\text{Ba}^+$, we experimentally address the problem of quantum coherence, entanglement, and quantum contextuality.

For the coherence of the quantum system, we study the decoherence process of $^{171}\text{Yb}^+$ ion qubit and extend the coherence time to more than one hour, which is one order of magnitude longer than the previous world record. Until now, the longest coherence-time of a single qubit was reported as 660 s. Here, we identify and suppress the limiting factors, which are the remaining magnetic-field fluctuations, frequency instability of the microwave reference-oscillator, and leakage of microwave. Then, we observe the coherence time of around 5500 s for the $^{171}\text{Yb}^+$ ion-qubit. In addition to the long coherence time, high fidelity entanglement gate is also essential for ion trap based quantum computers. We realize a two-qubit entanglement operation between $^{171}\text{Yb}^+$ and $^{138}\text{Ba}^+$ ions with fidelity up to 98%. Based on the entanglement state, we report the first experimental observation of contextual correlations between the outcomes of repeatable and nondisturbing measurements which are free of the detection and compatibility/sharpness loopholes simultaneously. The experimental results show measurement repeatability of 98.1% and a violation of the noncontextuality inequality by 15 standard deviations, in agreement

ABSTRACT

with the predictions of quantum mechanics. We believe our study is helpful for a deeper understanding of quantum physics and will accelerate practical applications of quantum information science.

Keywords: ion trap; quantum information science; coherence time; quantum contextuality; quantum computation

TABLE OF CONTENTS

摘 要.....	I
ABSTRACT.....	II
TABLE OF CONTENTS	IV
LIST OF FIGURES AND TABLES	VII
LIST OF SYMBOLS AND ACRONYMS	XV
CHAPTER 1 INTRODUCTION	1
1.1 Quantum information science.....	1
1.2 Coherence	2
1.2.1 Quantum channel.....	2
1.2.2 Resource theory of quantum coherence	4
1.3 Quantum contextuality.....	4
1.3.1 Contextuality inequality	5
1.3.2 Compatibility, non-disturbance and ideal measurement	5
1.3.3 Detection loophole and compatibility/sharpness loophole.....	6
1.4 Thesis organization.....	7
CHAPTER 2 ION TRAP	8
2.1 Ion trap system.....	8
2.2 Four-rod Paul trap	9
2.3 Multi-species trapped ion system.....	10
CHAPTER 3 $^{171}\text{YB}^+$ ION.....	12
3.1 Ion loading.....	12
3.2 Ion qubits	13
3.3 Doppler cooling, state initialization, state detection	13
3.4 Laser systems	16
3.4.1 370 nm and 935 nm lasers	16
CHAPTER 4 $^{138}\text{BA}^+$ ION.....	19
4.1 Ion loading.....	19

TABLE OF CONTENTS

4.2 Ion qubits	20
4.2.1 Zeeman qubits	20
4.2.2 Optical qubits	20
4.3 Doppler cooling, state initialization, state detection	22
4.4 Laser systems	22
4.4.1 493 nm and 650 nm lasers	22
4.4.2 1762 nm laser	23
4.4.3 Raman lasers	28
 CHAPTER 5 SINGLE ION QUBIT WITH COHERENCE TIME EXCEEDING ONE HOUR	 30
5.1 Introduction	30
5.2 Experiment details.....	31
5.2.1 Ion qubit	31
5.2.2 Suppression of ambient magnetic field.....	31
5.2.3 Improvements of microwave frequency-stability.....	33
5.2.4 Suppression of microwave power-leakage.....	33
5.2.5 Dynamical decoupling pulse sequence.....	34
5.3 Experiment results.....	35
5.3.1 Coherence time	35
5.3.2 Experimental study of decoherence process.....	35
5.3.3 Benchmark of quantum memory and quantum coherence.....	39
5.3.4 Coherence time without dynamical decoupling pulses.....	42
5.4 Expected limitations of coherence time	42
5.5 Software-based auto-relock system for laser frequency lock.....	46
5.6 Discussion	48
 CHAPTER 6 ENTANGLEMENT GENERATION BETWEEN $^{171}\text{YB}^+$ AND $^{138}\text{BA}^+$ IONS	 51
6.1 Ion qubits	51
6.2 EIT cooling and sideband cooling.....	53
6.3 Motional mode.....	55
6.3.1 Axial mode.....	55
6.3.2 Radial mode.....	57

TABLE OF CONTENTS

6.4 Mølmer-Sørensen (M-S) interaction	60
6.4.1 0.75 MHz axial trap frequency case	62
6.4.2 0.95 MHz axial trap frequency case	62
CHAPTER 7 LOOPHOLE-FREE CONTEXTUALITY TEST	65
7.1 Introduction	65
7.2 Loophole free contextuality test theory	66
7.2.1 Loophole free	66
7.2.2 4-cycle quantum contextuality inequality	66
7.3 Experiment result	68
7.3.1 Contextuality inequality violation	68
7.3.2 Repeatability of measurements	68
7.3.3 Compatibility of measurements	70
7.3.4 Crosstalk between qubits and their undesirable Raman beams	70
7.4 Summary	73
CHAPTER 8 QUANTUM FLUCTUATION THEOREMS AND QUANTUM TRA- JECTORIES MEASUREMENT	74
8.1 Classical fluctuation theorems	74
8.2 Quantum fluctuation theorems	75
8.2.1 $\theta = 0$ case in Petz recovery map	75
8.2.2 $\theta \neq 0$ case in Petz recovery map	77
8.3 Two point measurement (TPM) for quantum fluctuation theorems	77
8.4 Quantum trajectories measurement	79
CHAPTER 9 SUMMARY AND OUTLOOK	81
REFERENCES	82
APPENDIX A	91
ACKNOWLEDGEMENTS	95
声 明	96
RESUME	97
COMMENTS FROM THESIS SUPERVISOR	98
RESOLUTION OF THESIS DEFENSE COMMITTEE	100

LIST OF FIGURES AND TABLES

Figure 2.1	Schematic diagram of four-rod trap.	9
Figure 2.2	Four-rod trap.....	9
Figure 3.1	Ionization process of Yb atom. Electron is first excited to 1P_1 state by 399 nm laser and then to continuum by 370 nm laser. The figure is quoted from Ref. [85].	12
Figure 3.2	Energy levels of $^{171}\text{Yb}^+$	14
Figure 3.3	Repump scheme of $^{171}\text{Yb}^+$	15
Figure 3.4	Detection photon-count distribution for $^{171}\text{Yb}^+$ dark and bright state.	15
Figure 3.5	Laser scheme.	16
Figure 3.6	Optical paths of 370 nm and 935 nm laser.....	17
Figure 3.7	Iodine reference for laser frequency stabilization.	18
Figure 4.1	Two different ionization process of Ba atom: 413 nm laser only or combine with 553 nm laser. This figure is from Ref. [91].	19
Figure 4.2	Energy levels of $^{138}\text{Ba}^+$	20
Figure 4.3	Relative 1762 nm Rabi frequencies for different Δm	21
Figure 4.4	Basic operations of $^{138}\text{Ba}^+$ ion.....	22
Figure 4.5	Detection photon-count distribution for $^{138}\text{Ba}^+$ dark and bright state.	23
Figure 4.6	Optical paths of 493 nm laser.	24
Figure 4.7	Optical paths of 650 nm laser.	24
Figure 4.8	1762 nm laser cavity lock system.....	25
Figure 4.9	Schematic diagram of 1762 nm laser cavity lock system.....	25
Figure 4.10	Lock frequency of 1762 nm laser.	26
Figure 4.11	Power-lock module of 1762 nm laser.....	27
Figure 4.12	Mode spectrum measured by 1762 nm laser.....	27
Figure 4.13	Beam path of Raman lasers.	28
Figure 4.14	Schematic diagram of Raman lasers beam path.....	29
Figure 4.15	Repetition rate drift lock loop.....	29

- Figure 5.1 Experimental setup. (a), Energy levels of $^{171}\text{Yb}^+$ and $^{138}\text{Ba}^+$ ion and cut-away view of the μ -metal shielding enclosing octagon chamber. The shielding has ten holes, where two holes for connection of the vacuum pump and helical resonator and the other eight holes with diameter from 20 mm to 40 mm for the access of laser beams, microwave and imaging system. (b), The schematic diagram for the control of microwave and laser beams. We use a crystal oscillator (SIMAKE SMK3627OCHFMOCXO) to reference the microwave generator and Direct Digital Synthesize (DDS) through a 1 GHz signal generator. The microwave of 12.6 GHz is generated by mixing 200 MHz signal from DDS and 12.4 GHz from the microwave generator, which is amplified and applied to ions through a horn. All three microwave switches are used to reduce microwave leakage. For 369 nm laser beams, we use acousto-optic modulators (AOMs) to generate basic operating lasers. We use Electro-Optic pulse picker (EOPP), mechanical shutter and single-mode fiber to reduce laser leakage. The magnetic field direction is in the radial direction. We detect the qubit state with a photomultiplier tube (PMT). ...32
- Figure 5.2 Magnetic field shielding.33
- Figure 5.3 Suppression of magnetic-field noise. To check the noise suppression of magnetic-field shielding, we use 31 CPMG (Carr, Purcell, Meiboom and Gill) pulses to accumulate the AC magnetic-field noise^[37]. The figure shows Ramsey contrast as a function of the inter-DD pulse spacing τ . Black and red points represent data without and with shielding and permanent magnet^[37], respectively. Before the improvement of magnetic field stability, there are two dips at $\tau = 3.3$ ms and $\tau = 10$ ms which correspond to 150 Hz and 50 Hz noise, respectably, which disappeared after the improvement. We further increase the CPMG pulses number to 190, and get fringe contrasts of 0.97 and 0.98 at $\tau = 10$ ms and 3.3 ms, respectively. This indicates that the level of the noise at 50 Hz and 150 Hz are below 16 μG and 32 μG , respectively.34

Figure 5.4 Experimental sequence. Cooling laser beams for the $^{138}\text{Ba}^+$ ion are applied during the whole sequence. For $^{171}\text{Yb}^+$ ion, we first initialize the qubit and then start to apply the microwave pulses. All the KDD_{xy} (Knill dynamical decoupling) pulses are inserted between two $\pi/2$ pulses of Ramsey sequence. Blue and brown blocks represent Doppler cooling and optical pumping pulses for $^{171}\text{Yb}^+$ ion. EOPP and shutter are closed after state initialization and opened before state readout, where the time delays between them are shown as $\Delta t \approx 10$ ms, which is mainly caused by the limited speed of the mechanical shutter. Gray blocks represent KDD_{xy} units. T is the total measurement time, and τ is the interval of pulses. Each KDD_{xy} unit has ten π pulses, where the first and the second five pulses represent σ_x - and σ_y -rotation, respectively. Therefore, the second five pulses have 90° phase shift from the first five. We choose the total number of KDD_{xy} units even to make sure all the KDD_{xy} pulses are identity operation in the ideal case. In the end, we use a detection laser pulse to measure the qubit state.36

Figure 5.5 The evolution of Ramsey fringe contrast. Blue points are from the initial states of $|0\rangle$ and $|1\rangle$, and red points are from $|0\rangle + |1\rangle$, $|0\rangle + i|1\rangle$, $|0\rangle - |1\rangle$, and $|0\rangle - i|1\rangle$, where $\phi = 0, \frac{\pi}{2}, \pi$, and $\frac{3\pi}{2}$, respectively. Error bars are standard deviations. Each initial state at each data point repeats 30 to 100 times. The solid lines are the fitting results by the exponential decay function. Inset shows extrapolations of fits in a longer time range. The shadow indicates the enlarged area in the figure. The red-dashed line indicates the previous result of superposition states^[37]. The black-dashed line indicates the $1/e$ threshold. The red and blue arrows indicate times when threshold are reached.37

Figure 5.6 Fitting of process matrix elements evolution. Blue and black points are experimental results of χ_{IZ} and χ_{XY} , respectively. The solid lines are their fitting results.....39

Figure 5.7 Results of quantum process tomography. (a), Red and blue points represent process and mean fidelities, respectively. Error bars are standard deviations. The red line is the fitting result of Eq. (5.1). The blue line is the fitting result of the exponential decay function. Inset shows extrapolations of fits in a longer time range. The shadow indicates the enlarged area in the figure. The red and blue dashed horizontal lines indicate the process fidelity and mean fidelity of the final state, where the system lost all the quantum information. The blue vertical line indicates the time point when mean fidelity decays to $1/e$ threshold. (b), The real part of the process matrix after a storage time of (i): 4 min, (ii): 8 min and (iii): 16 min. The largest diagonal element of the process matrix is the identity operation part, χ_{11}^{exp} , which is the process fidelity F_p . (c), State evolution represented in the Bloch sphere after a storage time of (i): 4 min, (ii): 8 min and (iii): 16 min. Gray meshed spheres represent the initial pure states, which form the Bloch sphere. And blue spheres represent the output states after corresponding storage time, which are the same as the input state at $T = 0$ but shrink into the Bloch sphere later and transition to a dot in the center for $T \gg \min(T_1, T_2)$. Given the input state, the corresponding output state is calculated by the process matrix χ^{exp} . . . 40

Figure 5.8 Benchmark of quantum memory and coherence. Red and blue points are data of the robustness of quantum memory (RQM) and the mean ratio of the relative entropy of coherence (REC), respectively. Error bars are standard deviations. The red line is the theoretical result of the RQM calculated from the process matrix of Eq. (5.1) and the blue line is the exponential fitting result of the mean ratio of the REC. Inset shows extrapolations of fits in a longer time range. The shadow indicates the enlarged area in the figure. The blue vertical line indicates the time point when the mean REC ratio decays to $1/e$ 42

Figure 5.9 Coherence time obtained from Ramsey measurements. (a) without dynamical decoupling pulses and (b) with one spin echo pulse. Blue points are experimental results and each point repeats 100 times. The solid lines are their fitting by the Gaussian decay function. (a) A small detuning between microwave frequency and qubit energy splitting is used here to observe the oscillation signal rather than the fringe contrast signal to wipe out the frequency drift effect. The coherence time is 1.6 ± 0.22 s. (b) The red dashed line indicates the $1/e$ threshold. The coherence time is 11.1 ± 0.38 s. 43

Figure 5.10 Expected limitations of coherence time. The left boundaries of different color-bars indicate expected limitations caused by corresponding decoherence-sources as follows: (i) Phase noise of local oscillator; (ii) Magnetic-field fluctuation; (iii) Ion hopping; (iv) Scattering of $^{138}\text{Ba}^+$ lasers; (v) Leakage of the microwave; (vi) Collision of background gas; (vii) Lifetime of hyperfine ground-state. Currently, the coherence time is mainly limited by the phase noise of the local oscillator and the ultimate coherence time limited by the lifetime of the hyperfine state is estimates as around 5×10^{11} s. 44

Figure 5.11 Labview auto-relock program for laser frequency lock. 47

Figure 5.12 Auto-relock system hardware connection. 48

Figure 5.13 Auto-relock system logic block diagram. 49

Figure 6.1 Experimental setup. (a) and (b) are the energy level diagrams of $^{171}\text{Yb}^+$ and $^{138}\text{Ba}^+$ ion, respectively. Only relevant Raman transitions are shown here. (c), Ion trap in the octagon chamber and schematic diagram for Raman beams. Solid and dashed arrows indicate the directions and the polarizations of 532 nm and 355 nm laser beams, respectively. In the figure, $f_{\text{Yb},0}$ and $f_{\text{Ba},0}$ are the qubit frequencies of $^{171}\text{Yb}^+$ and $^{138}\text{Ba}^+$, respectively, $f_z = 1.67$ MHz is the frequency of the axial out-of-phase (OOP) mode, and δ is 22.0 kHz. (d), Frequencies of vibrational modes of a single $^{171}\text{Yb}^+$ and a single $^{138}\text{Ba}^+$ ions. Axial OOP mode is used for the Mølmer-Sørensen (M-S) interaction. IP stands for in-phase mode. 52

LIST OF FIGURES AND TABLES

Figure 6.2 Fano profile of EIT cooling. The horizontal axis is the RF frequency of the probe laser double pass AOM. The left side is the red side and the main peak is close to the resonant frequency. The small peak around 145 MHz is the Fano profile caused by the EIT effect. The vertical axis is the count of $^{138}\text{Ba}^+$ ion.....53

Figure 6.3 Fano profile for different probing beam power. Increasing probe beam power can improve peak count but also background count.54

Figure 6.4 Fano profile for different coupling beam frequency. Increasing coupling beam frequency can reduce background count but also reduce peak count.54

Figure 6.5 Sideband cooling scheme. The blue lines are the blue sideband Raman π pulses and the black solid lines are the optical pumping pulses. The black dashed lines are the spontaneous emission from $6P_{1/2}$55

Figure 6.6 Two ions axial IP mode amplitudes for different mass ratio. For our case, $\alpha = 138/171 = 0.807$. $^{171}\text{Yb}^+$ - $^{138}\text{Ba}^+$ ions axial IP mode amplitudes are (0.669, 0.744).....58

Figure 6.7 Two ions axial OOP mode amplitudes for different mass ratio. For our case, $\alpha = 0.807$. $^{171}\text{Yb}^+$ - $^{138}\text{Ba}^+$ ions axial OOP mode amplitudes are (-0.809, 0.587).....58

Figure 6.8 Two ions radial IP mode amplitudes for different mass ratio. For our case, $\alpha = 138/171 = 0.807$, $^{171}\text{Yb}^+$ - $^{138}\text{Ba}^+$ ions radial IP mode amplitudes are (0.409, 0.912).....59

Figure 6.9 Two ions radial OOP mode amplitudes for different mass ratio. For our case, $\alpha = 0.807$, $^{171}\text{Yb}^+$ - $^{138}\text{Ba}^+$ ions radial OOP mode amplitudes are (-0.874, 0.486).....60

Figure 6.10 MS gate scheme for $^{171}\text{Yb}^+$ - $^{138}\text{Ba}^+$. $|a_1 a_2, n\rangle = |a_1\rangle |a_2\rangle |n\rangle$ is the state of two ion qubit and motional state, $|a_1\rangle$ is state of $^{171}\text{Yb}^+$ qubit, $|a_2\rangle$ is state of $^{138}\text{Ba}^+$ qubit, $|n\rangle$ is motional state. Detuning between laser and motional level is δ , all the sideband Rabi frequency need to be balanced by adjusting the RF signal power of each AOM.....61

- Figure 6.11 Evolution of the M-S interaction and oscillation of parity signal when axial mode is 0.75 MHz. Each data point is the average of 100 repetitions and all the error bars are standard deviation. The first figure is the time evolution of the M-S interaction. P_{ij} is the population of state $|ij\rangle$, where $|i, j\rangle = |i\rangle_{\text{Yb}} |j\rangle_{\text{Ba}}$. $P_{11} + P_{00} = 0.89$ at the end of the gate. The second figure is the parity scan of the entangled state. Parity of a state is defined as $P_{11} + P_{00} - P_{10} - P_{01}$, which is the population difference between the two qubits being in same or opposite states. Parity contrast is 0.84 here. 63
- Figure 6.12 Evolution of the M-S interaction and oscillation of parity signal when axial mode is 0.95 MHz. Each data point is the average of 100 repetitions and all the error bars are standard deviation. (a) The time evolution of the M-S interaction. The duration of a single M-S gate is $45.4 \mu\text{s}$ and $P_{11} + P_{00} = 0.960 \pm 0.018$ at the end of the gate. (b) The parity scan of the entangled state. Parity contrast is 0.919 ± 0.021 64
- Figure 7.1 The four observables and compatibility relations. The observables \hat{O}_0, \hat{O}_2 are measured on the first qubit, and \hat{O}_1, \hat{O}_3 on the second qubit. The connected observables are compatible (jointly measurable). Here $\hat{\sigma}_x, \hat{\sigma}_y$ are Pauli operators and I_2 is the identity operator. 67
- Figure 7.2 Repeatability measurement sequence. Whole sequence include six steps: 1, Pump two qubits to $|0\rangle$ and then prepare the entangled state with M-S gate; 2, Rotate the measurement basis to the observable basis; 3, Projective measurement; 4, Rotate the measurement basis back; 5, Rotate the measurement basis to the observable basis again; 6, Projective measurement again. $R\left(\frac{\pi}{2}, \phi_{\text{Yb}}\right)$ in the pink box and $R\left(\frac{\pi}{2}, \phi_{\text{Ba}}\right)$ in the green box are $\pi/2$ rotations between $\hat{\sigma}_z$ basis and observable basis for $^{171}\text{Yb}^+$ qubit and $^{138}\text{Ba}^+$ qubit, respectively. Only rotations in the pink box will be applied when observable \hat{O}_0 or \hat{O}_2 are measured since they only performed on $^{171}\text{Yb}^+$ ion. $\phi_{\text{Yb}} = 5\pi/4$ and $3\pi/4$ for observable \hat{O}_0 and \hat{O}_2 . On the other hand, only rotations in the green box will be applied for observable \hat{O}_1 and \hat{O}_3 , where $\phi_{\text{Ba}} = 3\pi/2$ and π , respectively. 69
- Figure 7.3 Repeatability of four observable measurements. Each observable measurement repeat 1000 times. Error bar is the standard error of the mean (SEM). 69
- Figure 7.4 Crosstalk of $^{171}\text{Yb}^+$ carrier transition to $^{138}\text{Ba}^+$ ion. 71

LIST OF FIGURES AND TABLES

Figure 7.5	Crosstalk of $^{138}\text{Ba}^+$ carrier transition to $^{171}\text{Yb}^+$ ion.	71
Figure 8.1	Fluctuation theorem model.	74
Figure 8.2	Two point measurement scheme.	77
Figure 8.3	Measurements in the two point measurement.	78
Figure 8.4	Experiment scheme to measure quantum trajectory. The yellow box shows the dynamics of the system. ρ_0 is the input mixed state. \mathcal{N}_1 and \mathcal{N}_2 and so on are the unitary or noise quantum channel. ρ_1 and ρ_2 are the states after channels. For the measurement protocol, a ancilla qubit is used to get the information of operation qubit. A C-NOT type gate is applied between two qubits and then the ancilla qubit is measured in an overcomplete set.	80
Table 7.1	Experiment data.	67

LIST OF SYMBOLS AND ACRONYMS

AOM	acousto-optic modulator
EOM	electro-optic modulator
OOP	out-of-phase
IP	in-phase
PBS	polarizing beam splitter
BS	beam splitter
DDS	direct digital synthesizer
FPGA	field programmable gate array
PMT	photomultiplier tube
CCD	charge couple device
Yb	ytterbium
Ba	barium
AWG	arbitrary wave generator
MS	Mølmer-Sørensen
RQM	robustness of quantum memory
REC	relative entropy of coherence
PD	photo diode
EOPP	electro-optic pulse picker
KDD	Knill dynamical decoupling
SHG	second harmonic generation
SNR	signal noise ratio
CPMG	(Carr, Purcell, Meiboom and Gill)
MP	measure and prepare
EIT	electromagnetically induced transparency
SEM	standard error of the mean
WLM	wavelength meter
PDH	Pound-Drever-Hall
ULE	ultra-low expansion
WDM	wavelength division multiplexing
BOA	booster optical amplifiers
DAC	data acquisition card

CHAPTER 1 INTRODUCTION

1.1 Quantum information science

As a new method to describe the physical world, quantum physics can explain some phenomena that can't be explained by classical physics. Based on the magic features of quantum physics, such as coherence, superposition, entanglement, and contextuality, quantum information science has developed important applications, including quantum computation^[1-4], quantum communication^[5-10], and quantum metrology^[11-13] and so on.

Computation based on quantum mechanics was first proposed by Richard Feynman in 1982^[14]. Qubit is the basic unit of a quantum computer, which can be in the “0” and “1” state at the same time. It is so-called the superposition state, which is impossible for classical bits. Superposition makes it possible for a quantum computer to manipulate multiple input states simultaneously, which will significantly increase the speed of the computer. But once the quantum state is detected in the end, the output will collapse into one of the eigenstates. It means only one of the results can be seen and makes the speed-up of the quantum computer meaningless. Fortunately, some genius algorithms have been developed which can maintain the speed-up even in the collapse case. The two most famous algorithms are Shor's algorithm^[15-17] and Grover's algorithm^[18-19]. Until now, many systems have been explored and utilized to realize the power of quantum computation, including photonic system^[20], NV center system^[21], trapped ion system^[22-23], superconducting system^[24], and cold atom system^[25]. Quantum states in atom, photon or superconducting circuit are used to encode quantum bit (qubit). The platform used to build a quantum computer should meet the requirements nowadays known as the DiVincenzo criteria^[3]:

- (1) A scalable physical system with well-characterized qubits;
- (2) The ability to initialize the state of the qubits to a simple fiducial state, such as $|000\dots\rangle$;
- (3) Long relevant decoherence time, much longer than the gate operation time;
- (4) A universal set of quantum gates;
- (5) A qubit-specific measurement capability.

Quantum communication is another application of quantum physics, which has the capability to realize secure communication. The no-cloning feature of the quantum state

lies in the center of quantum communication security. Distribution of entangled states over a long distance is the starting point of quantum communication, where photon's attenuation problem limits the communication distance. One of the most promising protocols to solve this problem is quantum repeater^[5], which divides the communication distance into shorter ones. But the repeater should have a long coherence time to obtain a high success probability.

Quantum metrology is another important application of quantum mechanics. The measurement precision is highly limited by the measurement duration and qubit number in the entanglement state, which makes coherence time of the system and entanglement between qubits play an important role in quantum metrology.

1.2 Coherence

Coherence of qubit is one of the most fundamental bases for any quantum information science. But the coupling of environment noise and operation imperfection will always cause decoherence. The loss of coherence in the qubit can lead to the infidelity of quantum information processing, the inefficiency of a quantum repeater, and low sensitivity of quantum sensors and undermine quantum-information applications such as quantum money^[26-27]. Therefore, prolonging the coherence of the qubit quantum-memory is a major challenge of current quantum technology. Numerous experimental attempts have been made to extend the coherence time in a variety of quantum systems^[28-37].

1.2.1 Quantum channel

Decoherence process can be described by combination of quantum channels, a quantum channel is a completely positive trace-preserving map and can be written as Kraus operator form^[38]:

$$\varepsilon(\rho) = \sum_i A_i \rho A_i^\dagger. \quad (1.1)$$

A frequently-used quantum channel is the **Pauli channel**:

$$\varepsilon_{dep}(\rho) = (1 - p_x - p_y - p_z)\rho + p_x X \rho X + p_y Y \rho Y + p_z Z \rho Z, \quad (1.2)$$

where

$$I = \begin{pmatrix} 1 & 0 \\ 0 & 1 \end{pmatrix}, X = \begin{pmatrix} 0 & 1 \\ 1 & 0 \end{pmatrix}, Y = \begin{pmatrix} 0 & -i \\ i & 0 \end{pmatrix}, Z = \begin{pmatrix} 1 & 0 \\ 0 & -1 \end{pmatrix} \quad (1.3)$$

are Pauli operators of single qubit.

There are several other channels related to decoherence process:

Depolarization channel: describes a quantum channel where the input state has a probability of p to change to completely mixed state and a probability of $1 - p$ to keep the same. Map of the depolarization channel is:

$$\varepsilon_{dep}(\rho) = (1 - \frac{3}{4})\rho + \frac{1}{4}(X\rho X + Y\rho Y + Z\rho Z). \quad (1.4)$$

Dephasing channel: describes a quantum channel where the energy level of qubit or drive field frequency is not stable. This situation will cause relative phase fluctuation between two qubit bases and loss of the phase information. After this channel, the input state has a probability of p to completely lose the phase information and a probability of $1 - p$ to keep the same. Map of the dephasing channel is:

$$\varepsilon_Z(\rho) = (1 - \frac{1}{2})\rho + \frac{1}{2}Z\rho Z. \quad (1.5)$$

Amplitude damping channel: describes a quantum channel where population at the higher energy level has some chance to decay to the lower one. One of the examples is the spontaneous emission of ions or atoms. The higher energy level population of the input state has a probability of p to decay to the lower energy level, and a probability of $1 - p$ to keep the same. Map of the amplitude damping channel is:

$$\varepsilon_Z(\rho) = \begin{pmatrix} 1 & 0 \\ 0 & \sqrt{1-p} \end{pmatrix} \rho \begin{pmatrix} 1 & 0 \\ 0 & \sqrt{1-p} \end{pmatrix} + \begin{pmatrix} 0 & \sqrt{p} \\ 0 & 0 \end{pmatrix} \rho \begin{pmatrix} 0 & 0 \\ \sqrt{p} & 0 \end{pmatrix}. \quad (1.6)$$

Combination of amplitude damping and dephasing channel^[39-40]:

$$\varepsilon_{depZ_t}(\rho) = (1 - p_x - p_y - p_z)\rho + p_x X\rho X + p_y Y\rho Y + p_z Z\rho Z, \quad (1.7)$$

where $p_x = p_y = \frac{1-e^{-t/T_1}}{4}$ and $p_z = \frac{1}{2} - p_x - \frac{e^{-t/T_2}}{2}$, T_1 and T_2 are depolarizing and total dephasing time, respectively. This is called a ‘‘Pauli-twirled’’ channel since the ideal channel for combination of amplitude damping and dephasing channel has a form of:

$$\varepsilon_{depZ} \left(\begin{pmatrix} 1 - \rho_{11} & \rho_{01} \\ \rho_{10} & \rho_{11} \end{pmatrix} \right) = \begin{pmatrix} 1 - \rho_{11}e^{-t/T_1} & \rho_{01}e^{-t/T_2} \\ \rho_{10}e^{-t/T_2} & \rho_{11}e^{-t/T_1} \end{pmatrix}, \quad (1.8)$$

which can't be written in a Pauli channel form in Eq. 1.2. Formula in Eq. 1.7 is obtained by a twirling method to map a complicated channel to a simple one^[41].

1.2.2 Resource theory of quantum coherence

Coherence time and quantum channel can be used to describe the coherence performance of a quantum process or quantum system, but not a quantum state. Then the resource theory of state coherence has also been developed^[42-43] to provide tools for the systematic study of the decoherence process. Basic quantifier concepts include “distillable coherence” and “coherence cost”^[42].

The distillable coherence^[42] is related to the coherence distillation process, where pure state is extracted from a mixed state by incoherent process. Distillable coherence of a state is the maximum probability to extract a pure state through the coherence distillation process. It has the same formula as relative entropy of coherence:

$$C_d(\rho) = S(\Delta(\rho)) - S(\rho), \quad (1.9)$$

where $\Delta(\rho) = \sum_i \langle i | \rho | i \rangle | i \rangle \langle i |$, $\{|i\rangle\}$ is the qubit basis, and $S(\rho) = -\text{Tr}(\rho \log_2 \rho)$ is the Von Neumann entropy.

The coherence cost is related to an incoherent process where pure states are used to prepare a mixed state. The coherence cost of a target state $\rho = \sum_i p_i |\psi_i\rangle \langle \psi_i|$ is the minimum rate for the consumption of pure state to prepare the target state. It has the same formula as coherence of formation:

$$C_{cost}(\rho) = \min \sum_i p_i S(\Delta(\psi_i)). \quad (1.10)$$

1.3 Quantum contextuality

In classical physics, all the measurements have a pre-existing value and their output won't be affected by the fact that other compatible measurements are performed or not. But quantum physics has different rules, even compatible measurements have correlations. This feature is called quantum contextuality. One of the famous examples of quantum contextuality is the Bell test^[44-47], but in which, space-like separation of two subsystems is necessary to test the Bell inequality. Then Kochen and Specker^[48] introduced a more general way to demonstrate quantum contextuality even in a single quantum system. The space-like separation is no more necessary and any quantum system whose Hilbert space dimension is bigger than two can be used to test the quantum contextuality.

Testing contextuality requires observing the violation of noncontextuality inequalities^[49-50] involving correlations between ideal measurements that can be jointly per-

formed. The critical points in a contextuality test are assuring that the measurements are repeatable and do not disturb other measurements (i.e., that they are “sharp”^[51] or “ideal”^[52-53]), that all measurements are jointly measurable with any of the other measurements with which correlations are considered^[53]. It also requires that the detection efficiency should be above a certain threshold^[54] that guarantees that no noncontextual-hidden-variables model can simulate the experimental data.

1.3.1 Contextuality inequality

To test the contextuality of a quantum system experimentally, contextuality inequality is developed to distinguish contextuality system and non-contextuality system, which is deduced from the assumption of non-contextuality. It means that the inequality holds well for all the non-contextuality systems. Then a violation of the inequality indicates the contextuality of the system. Two famous contextuality inequalities are Clauser-Horne-Shimony-Holt (CHSH) inequality^[55-58] and KlyachkoCan-Binicioglu-Shumovsky (KCBS) inequality^[49,59].

CHSH inequality:

$$\langle A_0 B_0 \rangle + \langle A_0 B_1 \rangle + \langle A_1 B_0 \rangle - \langle A_1 B_1 \rangle \leq 2. \quad (1.11)$$

KCBS inequality:

$$\langle A_0 A_1 \rangle + \langle A_1 A_2 \rangle + \langle A_2 A_3 \rangle + \langle A_3 A_4 \rangle + \langle A_4 A_0 \rangle \geq -3. \quad (1.12)$$

Then all the inequality are generalized to N-cycle inequality for $n \geq 4$ ^[60]:

$$\Omega = \sum_{i=0}^{n-1} \gamma_i \langle A_i A_{i+1} \rangle^{\text{NCHV}} \leq n - 2, \quad (1.13)$$

where $\gamma_i \in \{1, -1\}$, and the number of $\gamma_i = -1$ is odd. $n-2$ is the violation bound. CHSH inequality is corresponding to $n = 4$ and KCBS inequality is corresponding to $n = 5$.

1.3.2 Compatibility, non-disturbance and ideal measurement

There are several important definitions^[61] for contextuality test that need to be clarified here. Assume a measurement x is measured on the state $|\psi\rangle$, then the possibility to get an output of a is denoted as $P(x = a|\psi)$.

Coarse-graining: If $c \in C$ is the outcomes of measurement z and $a \in A$ is the outcomes

of measurement x , if there is $A_c \in A$ for all $c \in C$ and all states $|\psi\rangle$ such that:

$$P(z = c|\psi) = \sum_{a \in A_c} P(x = a|\psi) \quad (1.14)$$

and $A_c \cap A_{c'} = \emptyset$ if $c \neq c'$, then measurement z is a coarse-graining of measurement x .

Compatible: Two coarse-grainings of the same measurement are compatible.

Non-disturbing: Assume a set of measurements $X = \{x_i\}$ have respective outcome of $a_i \in A_i$. Another set of measurements $Y = \{y_i\}$ have respective outcome of $b_j \in B_j$. And every pair of measurements (x_i, y_j) are compatible. If for all $x_i \in X$, $a_i \in A_i$ and $y_j, y_k \in Y$,

$$\sum_{b_j \in B_j} P(x_i = a_i, y_j = b_j|\psi) = \sum_{b_k \in B_k} P(x_i = a_i, y_k = b_k|\psi) \quad (1.15)$$

and, for all $y_i \in Y$, $a_i \in A_i$ and $y_j, y_k \in Y$,

$$\sum_{a_j \in A_j} P(x_j = a_j, y_i = b_i|\psi) = \sum_{a_k \in A_k} P(x_k = a_k, y_i = b_i|\psi), \quad (1.16)$$

then X and Y are mutually non-disturbing.

Ideal (or sharp): If a measurement satisfies:

- (i) It gives the same outcome when measured consecutively on the same system,
- (ii) It does not disturb compatible measurements,
- (iii) All its coarse-grainings satisfy (i) and (ii).

Then the measurement is ideal^[51].

1.3.3 Detection loophole and compatibility/sharpness loophole

In the experimental test of quantum contextuality, several loopholes need to be closed. The first one is the detection loophole^[62-64]. Detection loophole refers to the problem that the observed correlations can be explained by a hidden variable model if only a subensemble of experiment results are detected. Detection loophole is a challenging problem for photon-related experiments due to the low detection efficiency of single-photon^[18-19,65]. But for the atom or ion related platforms where single-shot fluorescence detection technique can be applied^[66-67], the detection loophole can be closed easily due to the high detection efficiency.

The second loophole is the compatibility/sharpness loophole^[68] which refers to not perfectly compatible observables and unsharp measurement. It is usually caused by imperfections in operations and measurements. The contextuality theory is based on the fact

that all the measurements are sharp and the measurements in a context are compatible. Contextuality inequalities can be violated by unsharp measurements even no contextuality is involved.

1.4 Thesis organization

My Ph.D. study focuses on the $^{171}\text{Yb}^+ - ^{138}\text{Ba}^+$ trapped ion system. In the last five years, I was involved in three projects. One of them is enhancing the coherence time of single $^{171}\text{Yb}^+$ ion. The other two are entanglement generation between $^{171}\text{Yb}^+$ and $^{138}\text{Ba}^+$ ions and loophole-free contextuality inequality test. This thesis is organized as follows: Chapter 1 is an overall introduction to the quantum information science theories related to quantum coherence and quantum contextuality. Chapter 2 talks about the trapped ion system; Chapter 3 and 4 talk about the detail of $^{171}\text{Yb}^+$ and $^{138}\text{Ba}^+$ trapped ion setup, including all the ion qubit energy levels, the basic operations of ion qubit, and related lasers. Chapter 5 focuses on enhancing the single $^{171}\text{Yb}^+$ ion qubit coherence time to hour level^[69]. And Chapter 6 talks about the generation of entanglement between $^{171}\text{Yb}^+ - ^{138}\text{Ba}^+$ ions. Based on the entanglement state, Chapter 7 demonstrates the first experimental loophole-free test of contextual correlations between the outcomes of repeatable and nondisturbing measurements. Chapter 8 briefly talks about the undergoing experiment about quantum fluctuation theorems and quantum trajectories measurement. Chapter 9 is the summary and outlook.

CHAPTER 2 ION TRAP

2.1 Ion trap system

Trapped ion systems use RF and DC electric fields and magnetic fields to trap charged ions in a vacuum chamber. Since the trapped ions don't have direct contact with the external environment, this well-isolated system can obtain a long coherence time. And the energy levels of ions provide a natural platform for the coding of qubit. Increasing of qubit number can be achieved by adding more ions. Trapped ion system has several properties that make it a leading platform for quantum information science.

- All the same species ion qubits are exactly the same. Unlike the artificial qubits in the superconducting system, ion qubits are naturally the same no matter where the ions are. This makes the calibration process of the operating parameters easier.
- The quantum state of trapped ions can be prepared to a known state with high fidelity. Ion qubit state can be initialized to $|0\rangle$ state by optical pumping, in which the laser frequency and polarization are designed to pump all the ion population to one of the states. The optical pumping process has high efficiency and high fidelity. And various cooling techniques can be used to cool the ion motional state to the near ground state, such as EIT cooling, Sisyphus cooling, and sideband cooling.
- The quantum state of trapped ions can be detected with high fidelity. Unlike photon systems, where photon detectors can't achieve perfect quantum efficiency, ion trap systems use standard fluorescence detection techniques to detect the qubit state, and all detection events will have an output with high fidelity.
- The trapped ion system is well isolated from the environment and has a long coherence time. Ion trap system has demonstrated ten min level coherence time in 2017^[37] and hour level coherence time in 2021^[69], which is 6×10^7 times longer than the typical two-qubit gate time duration of $100 \mu\text{s}$. Long coherence time also helps to reduce the gate infidelity caused by decoherence.
- High fidelity single-qubit and two-qubit gates in trapped ion systems have been demonstrated experimentally. They are the bases of universal quantum computation.

2.2 Four-rod Paul trap

Paul trap^[70-72] is a class of ion traps that use RF and DC electric fields to produce the confinement. Depending on the design of electrodes, the Paul trap is divided into four-rod trap, blade trap, surface trap, and so on. The four-rod trap is one of the simplest versions of the Paul trap. As shown in Fig. 2.1, there are four rods and two needles in our four-rod trap, rod 1 and 3 are grounded. Rod 2 and 4 are connected to the RF electric signal. These four rods provide radial confinement of the ion, and two needles in the axial direction are applied to a positive voltage to provide axial DC confinement. Ions form a linear crystal in the axial direction when the axial trap frequency is smaller than the radial one.

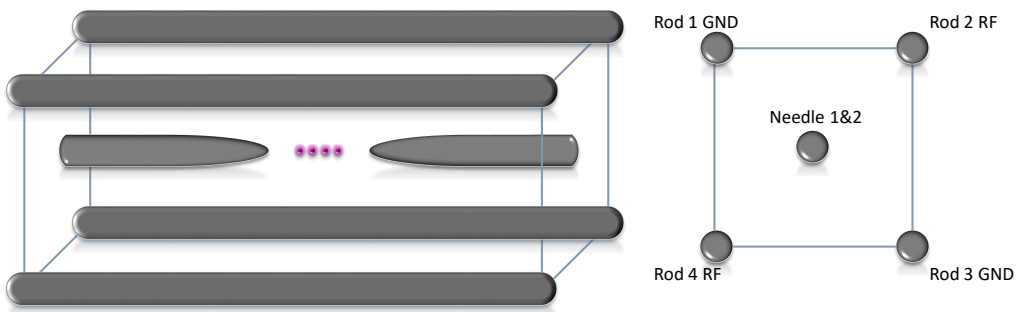


Figure 2.1 Schematic diagram of four-rod trap.

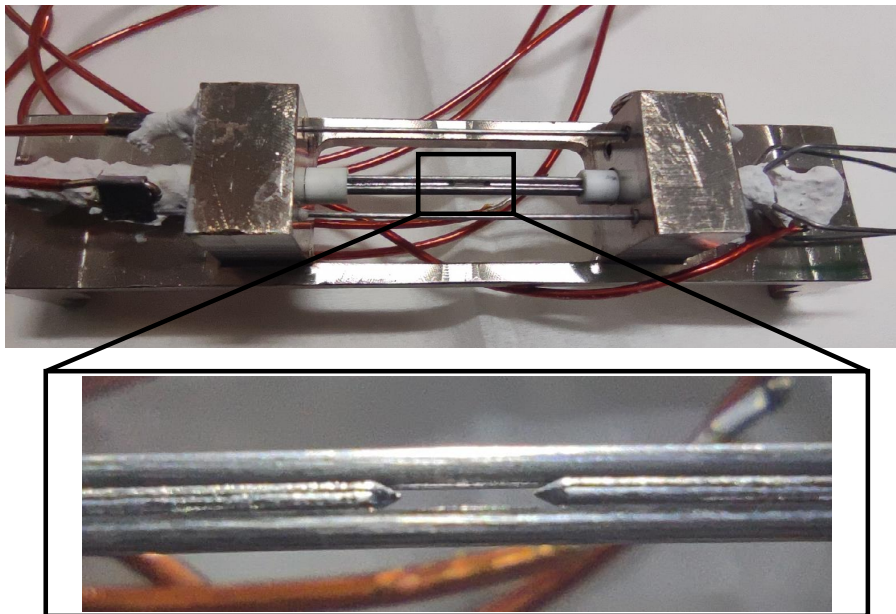


Figure 2.2 Four-rod trap.

2.3 Multi-species trapped ion system

We can trap more than one species of ions in single ion trap, and in a sense, the difference between the two species can be a powerful tool. This makes it possible for a multi-species trapped ion system to deal with some tasks that are difficult for a single-species trapped ion system. Multi-species trapped ion system has some advantages as follows:

- The multi-species trapped ion system can adopt the advantage of both species. For example, ion-photon quantum network is one of the most promising protocols to scale ion-based quantum computers up. Multi-species trapped ion system^[73-74] is suitable for ion-photon network. One species of ion with long coherence time can be used as memory qubits, and the other species of ion with fiber-friendly fluorescence wavelength can be used as communication qubits;
- The multi-species trapped ion system can be used for sympathetic cooling^[75-78]. During the quantum computation process, the direct cooling of qubit ion is not allowed since the cooling will destroy the qubit state, and this problem will be more serious when the quantum circuit is longer. Because the ion will keep heating until the phonon number is too high to do the quantum gate. Sympathetic cooling technic in multi-species trapped ion systems can solve this problem efficiently. Cooling of part of the ions in a trap will cool other ions through Coulomb interactions. Due to the fact that the cooling lasers for different species of ions are different, cooling of one species of ion won't disturb other ion's quantum state. Then sympathetic cooling can be used to continually cool the system during the quantum computation process;
- The multi-species trapped ion system can apply adaptive control^[79] in a quantum circuit. Trapped ion systems use standard fluorescence detection techniques for quantum state detection. Due to the limited collection efficiency of the imaging system and quantum efficiency of photon detector, ions emit a lot of photons during the detection process. These photons have some chance to be absorbed by other nearby ions, which will lead to crosstalk between ions. So the quantum state of part of the ions can't be detected in the middle of the quantum circuit without introducing cross-talk errors. But this problem can also be solved by multi-species of ions. There is no cross-talk between the detection of different species of ions since they have different detection lasers. This application makes it possible to perform some

circuit that a feedback process is involved, such as quantum error correction^[80-82], which is essential for realizing a universal quantum computer;

- The multi-species trapped ion system can manipulate part of the ions without interfering with others. Different species of ions have different energy levels, then need different microwaves or lasers to manipulate the qubits. This fact makes it easy for a multi-species ion trap to manipulate only one species of ions without disturbing the other one. Another way to manipulate part of the ions is using tightly focused laser beams to individually address each ion^[23]. But individually addressing needs a technical effort and cross-talk between neighbor ions always exists due to the nature of the Gaussian laser beam.

CHAPTER 3 $^{171}\text{Yb}^+$ ION

3.1 Ion loading

Loading ions to the trap is the first step of the ion trap experiment. We use a home-made oven to generate an atom gas beam^[83-84]. A stainless steel tube is first blocked at one end and then filled with corresponding atom material up to 2/3, and then mounted into a ceramic tube for thermal isolation. The stainless steel tube together with ceramic tube are mounted on a holder to fix the tube direction to point at the trap center. During the ion loading, 1 ~ 4 A current is applied to the stainless steel tube to increase its temperature and heat the inside materials to generate an atom gas beam. The long tube limits the spreading angle of the atom beam and guides the atoms to the center of the trap.

In the trap center, focused ionization lasers are used to ionize atom into ion. As shown in Fig. 3.1, we use 399 nm lasers to ionize Yb atoms. Once the atom is transformed into an ion, it feels the radial pseudo-potential and axial DC potential produced by the four-rod trap and has a probability to be trapped. And more ions will be loaded one by one in the same way. Another more efficient way for ion loading is laser ablation^[86-89]. A piece of

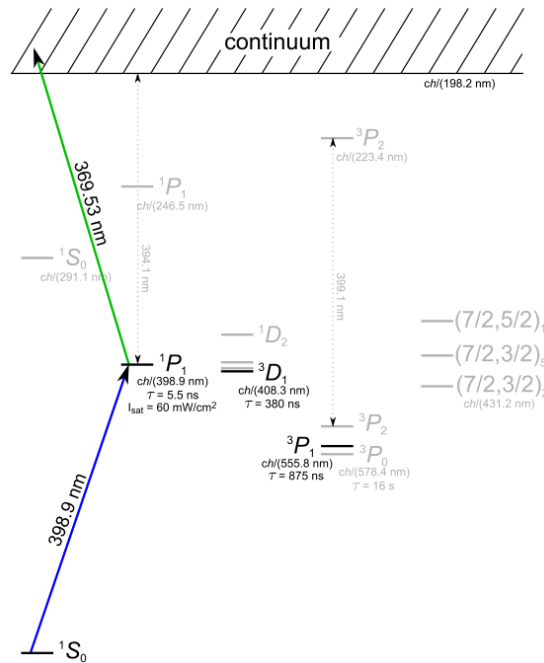


Figure 3.1 Ionization process of Yb atom. Electron is first excited to 1P_1 state by 399 nm laser and then to continuum by 370 nm laser. The figure is quoted from Ref.^[85].

pure atom or compound material target is first mounted into the vacuum chamber, during the loading, a strong pulsed laser is focused at the target to ablate it. The atoms sputtered out will have some chance to be ionized and trapped in the center of the trap. The loading process with laser ablation has several advantages. Firstly, laser ablation is more efficient than a thermal oven since it doesn't need any warm-up time. Secondly, unlike a thermal oven, laser ablation almost doesn't have any thermal heating effect which is good for the thermal stabilization of the whole trap. But laser ablation needs a careful design of the beam pass of the high power ablation laser. One straightforward way is to let the beam first goes through the trap center and then hits the ablation target, then the sputtering out atoms can directly go back to the trap center^[89]. But in this protocol, the ablation laser has to be carefully aligned and focused to avoid hitting the trap rod or blade. Another way is separating the laser beam and atom beam direction to avoid ablation laser going through the trap center^[90], which also needs an ingenious design of the beam pass since most viewports are designed for normal incidence to the trap center.

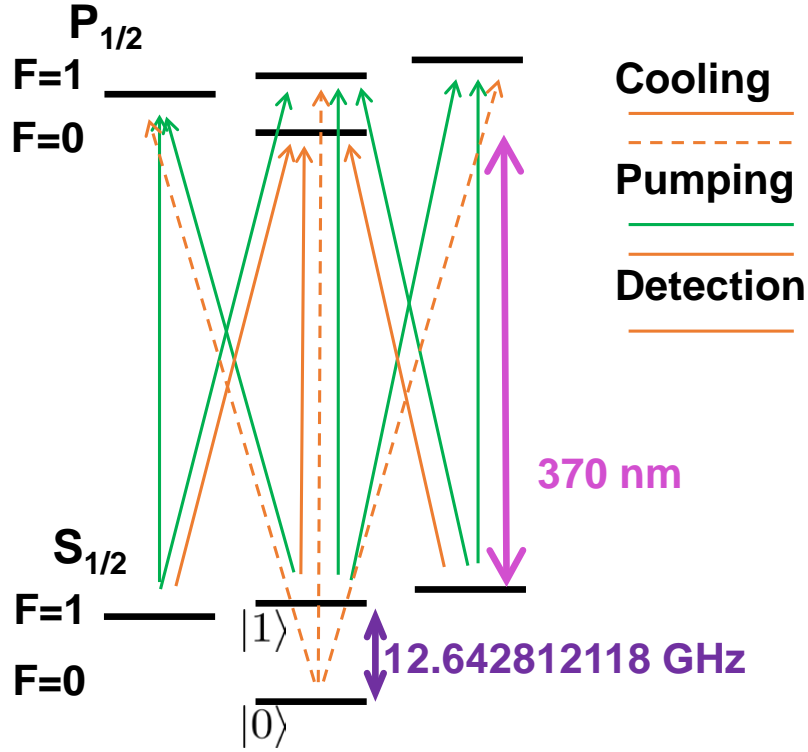
3.2 Ion qubits

In our system, the qubit is encoded at the energy levels of ions. For the $^{171}\text{Yb}^+$ ion shown in Fig. 3.2, two hyperfine levels of the $^2S_{1/2}$ manifold are used to encode the qubits, denoted as $|0\rangle_{\text{Yb}} \equiv |F=0, m_F=0\rangle$ and $|1\rangle_{\text{Yb}} \equiv |F=1, m_F=0\rangle$. The energy difference between the two states is $f_{\text{Yb}} = 12642812118.5 + (310.8)B^2$ Hz, where B is the strength of external magnetic field in Gauss.

3.3 Doppler cooling, state initialization, state detection

In the ion trap experiment, Doppler cooling, state initialization, and state detection are three essential basic operations.

For the Doppler cooling, we use red detuned 370 nm lasers to cool the $^{171}\text{Yb}^+$ ion down to dozens of phonon number. Unlike the cold atom system, where six Doppler cooling beams are used to cool the atom, ion's three-dimensional motional cooling only needs one cooling laser beam due to the tight confinement of trap potential. The ion will always feel a Doppler force along the direction of the cooling beam. But it won't escape due to the tight confinement of the ion trap. In order to have efficient cooling, the dark state of the ion has to be avoided by either adding an external magnetic field or using


 Figure 3.2 Energy levels of $^{171}\text{Yb}^+$.

polarization-modulation cooling lasers. And repump lasers are necessary to repump ions back to the main cooling cycle. As shown in Fig. 3.3, we use 935 nm lasers to repump $^{171}\text{Yb}^+$ ion from $^2D_{3/2}$ state.

The state initialization process is used to reset the state of the ion qubit to a specific initial state. For $^{171}\text{Yb}^+$ ion, the state initialization process is realized by designing the frequency of 370 nm laser. As shown in Fig. 3.2, the pumping laser only couples the three levels in ($^2S_{1/2}, F = 1$) and keeps the $|0\rangle_{\text{Yb}}$ alone, which will keep pumping the population to $|0\rangle_{\text{Yb}}$ and get a high fidelity $|0\rangle_{\text{Yb}}$ state.

For the state detection process, we use the standard fluorescence detection technique to detect the qubit state. For the $^{171}\text{Yb}^+$ ion, a 370 nm laser which is resonant with transition between $|1\rangle_{\text{Yb}}$ and $|F = 0, m_F = 0\rangle$ in $^2P_{1/2}$ manifold is used as the detection beam. The transition between $|F = 0, m_F = 0\rangle$ in $^2P_{1/2}$ and $|0\rangle_{\text{Yb}}$ is forbidden. When the ion is in the $|1\rangle_{\text{Yb}}$ state, due to the lifetime of $P_{1/2}$ state is only 8.7 ns, lots of photons will be emitted, and part of them will be collected by our imaging system. On the other side, no photon will be emitted if the ion is in the $|0\rangle_{\text{Yb}}$ state. Then the photon number collected

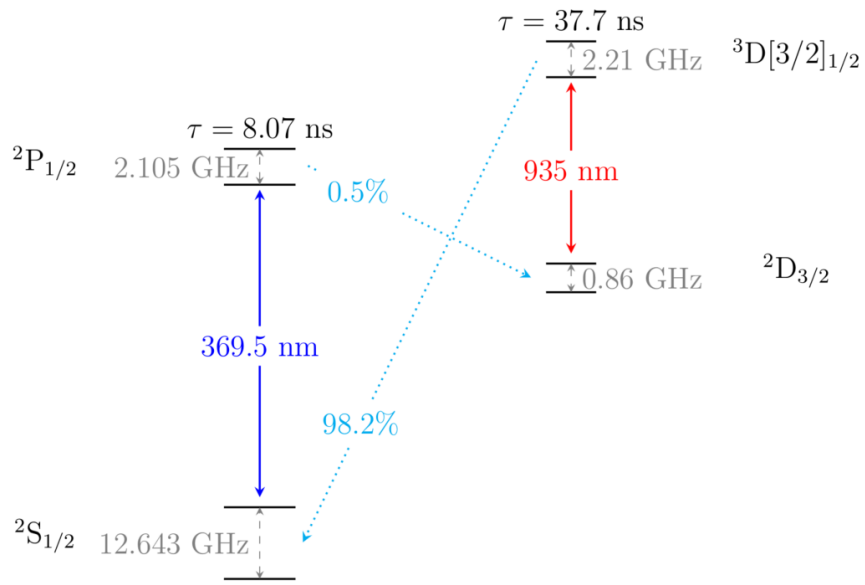


Figure 3.3 Repump scheme of $^{171}\text{Yb}^+$.

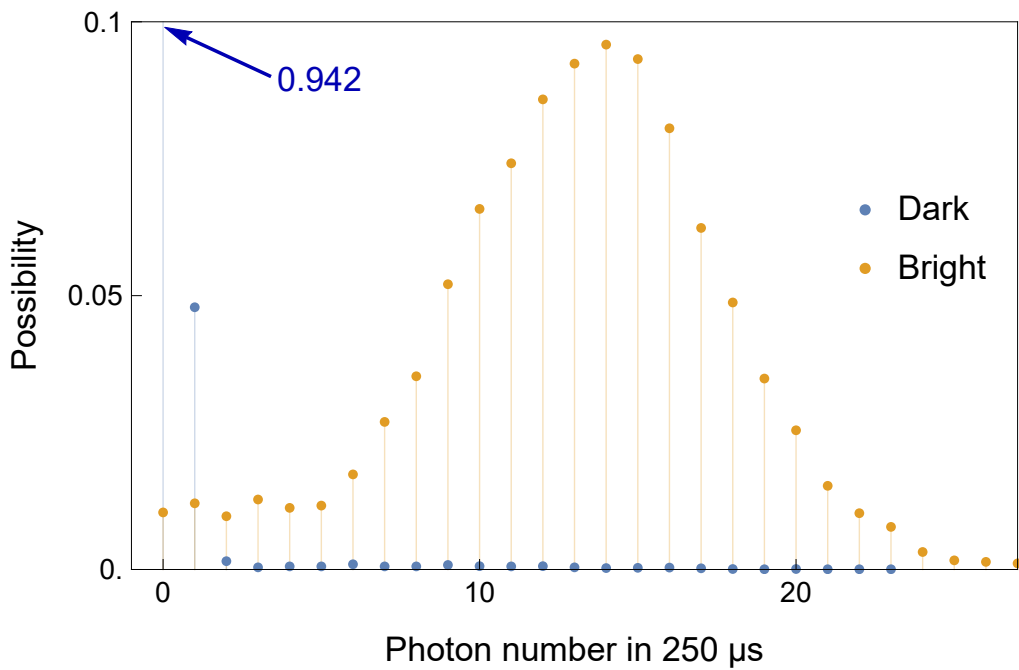


Figure 3.4 Detection photon-count distribution for $^{171}\text{Yb}^+$ dark and bright state.

by the imaging system can be used to distinguish qubit states. As shown in Fig. 3.4, the detection process of $^{171}\text{Yb}^+$ ion has detection infidelity of 2.25% for the bright state, and 0.96% for the dark state.

3.4 Laser systems

$^{171}\text{Yb}^+$ and $^{138}\text{Ba}^+$ ions need independent lasers for Doppler cooling, state initialization, state detection, and qubit manipulate, which makes the laser system much more complicated than these of single-species ion system^[83-84]. As shown in Fig. 3.5, all the lasers are applied to the trap center through the 5 side viewports of the octagon vacuum chamber. The other three sides are occupied by a vacuum connection, RF connection, and a permanent magnet. The magnet is used to generate the external magnetic field.

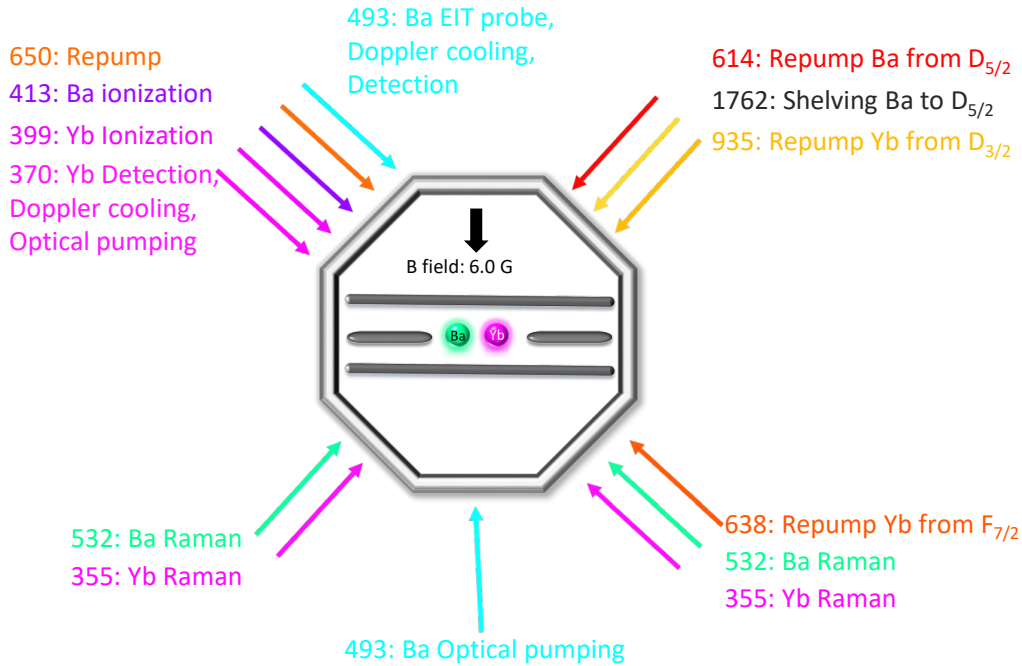


Figure 3.5 Laser scheme.

3.4.1 370 nm and 935 nm lasers

The 370 nm laser is produced by second-harmonic generation (SHG) of 739 nm laser from Toptica. As shown in Fig. 3.5, the 739 nm laser before the SHG is locked to an iodine reference. We use the 370 nm laser to produce basic operation lasers of $^{171}\text{Yb}^+$. The electro-optical pulse picker (EOPP) after the laser output is used as a fast optical switch. Three AOMs are used as switches for Doppler cooling (DOP) beam, detection

(DET) beam and optical pumping (OPT) beam. A 7.36 GHz EOM is used to generate $2 \times 7.36 = 14.72$ GHz sideband for the DOP beam. Another 2.095 GHz EOM is used to generate sidebands for OPT beam. The zero order beam of DOP AOM has a power of more than 200mW. This so-called “strong beam” is used as a protection beam to bring ions back once the ion crystal melt. In the end, the four beams were first combined into two beams through PBS, and then combined into one beam by BS. It is then sent to the trap through a single-mode fiber. The 935 nm laser first passes through a 3.1 GHz fiber EOM and is then sent to the trap by fiber.

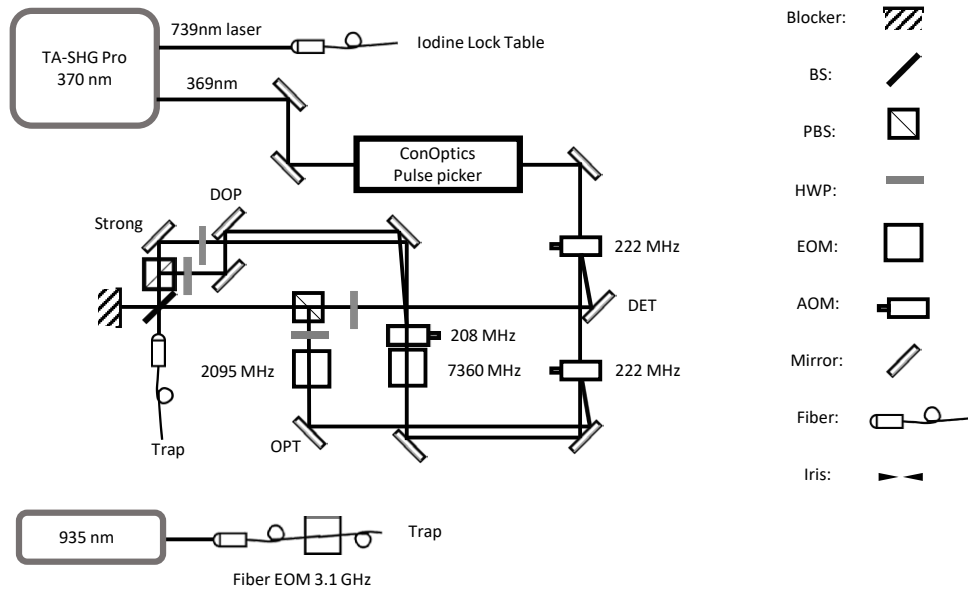


Figure 3.6 Optical paths of 370 nm and 935 nm laser.

The 739 nm laser is first shifted by 13.283 GHz through a fiber EOM and then sent to the iodine reference table. As shown in Fig. 3.7, on the iodine reference table, the 2 mW 739 laser is first separated into three parts: pump beam, probe beam, and reference beam. The reference beam directly goes to the balanced PD as a reference of laser power. The pump beam first passes through an AOM, whose input signal is modulated at 10 kHz. Then the first-order modulated beam is applied to a 280 °C iodine cell. The probe beam is directly applied to the iodine cell counter-propagating with the pump beam. The probe beam after the cell goes to the balanced PD to obtain the saturated absorption spectrum signal. The signal of the balanced PD and 10 kHz trigger signal are then sent to a lock-in amplifier to generate error signal. The lock-in amplifier is only sensitive to signals with the same modulation frequency as trigger signal. In principle, this protocol suppresses all other noise signals and has a high signal-to-noise ratio (SNR). But in practice, the pump

laser after the iodine cell also has the same modulation frequency. Some of the pump laser has the chance to be reflected by the lens surface or fiber surface, and then observed by the balanced PD. This will affect the SNR a lot. To solve this problem, as shown in Fig. 3.7, we use several wave plates and PBS to ensure that the pump beam behind the iodine cell was completely blocked.

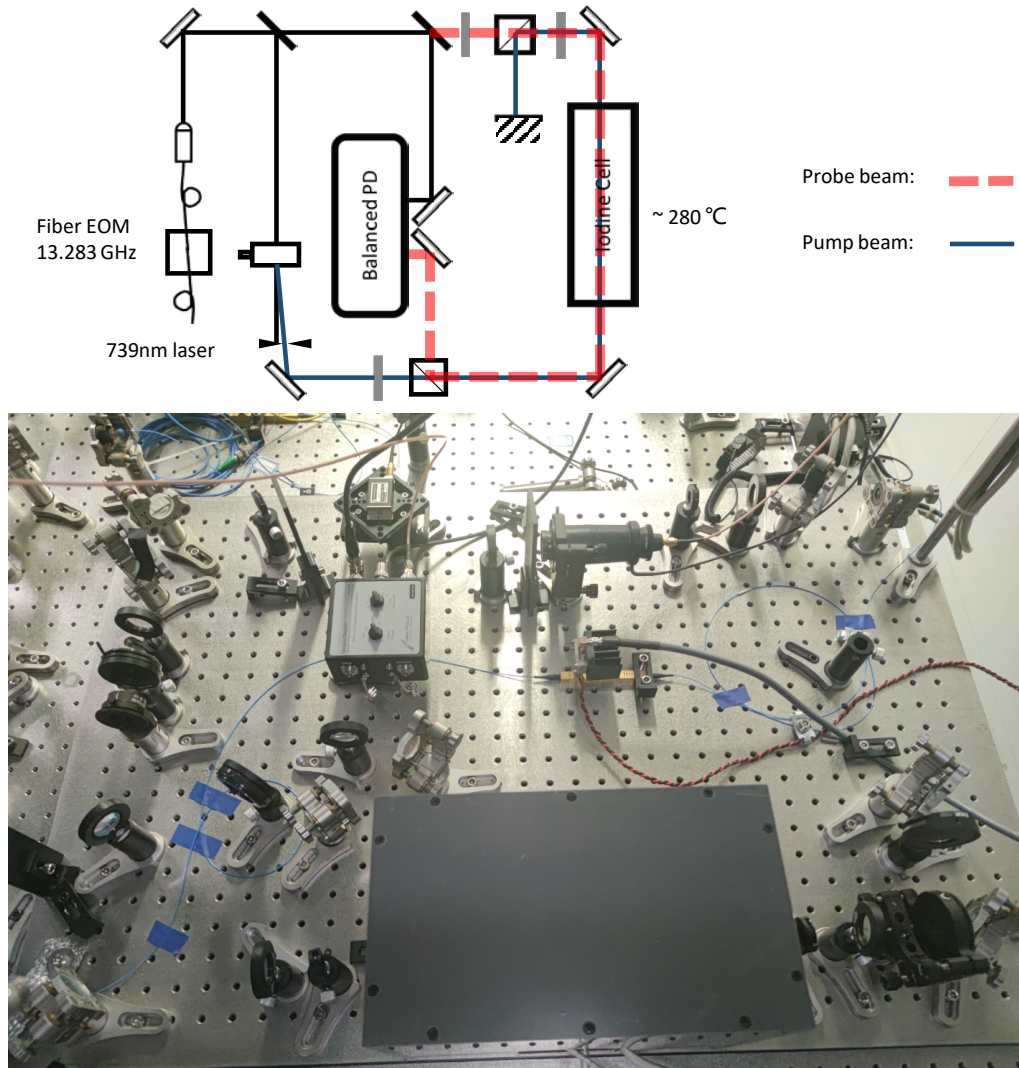


Figure 3.7 Iodine reference for laser frequency stabilization.

CHAPTER 4 $^{138}\text{Ba}^+$ ION

4.1 Ion loading

Same as the $^{171}\text{Yb}^+$ ion we also use an atomic oven for the loading of $^{138}\text{Ba}^+$ ion. For the Ba atom shown in Fig. 4.1, there are two main ways to ionize it into ion. Here, we use 413 nm laser to ionize Ba atom by two-step ionization. Another more efficient way is to use 553.7 nm and 413 nm laser for atom ionization^[91], where one more laser is needed.

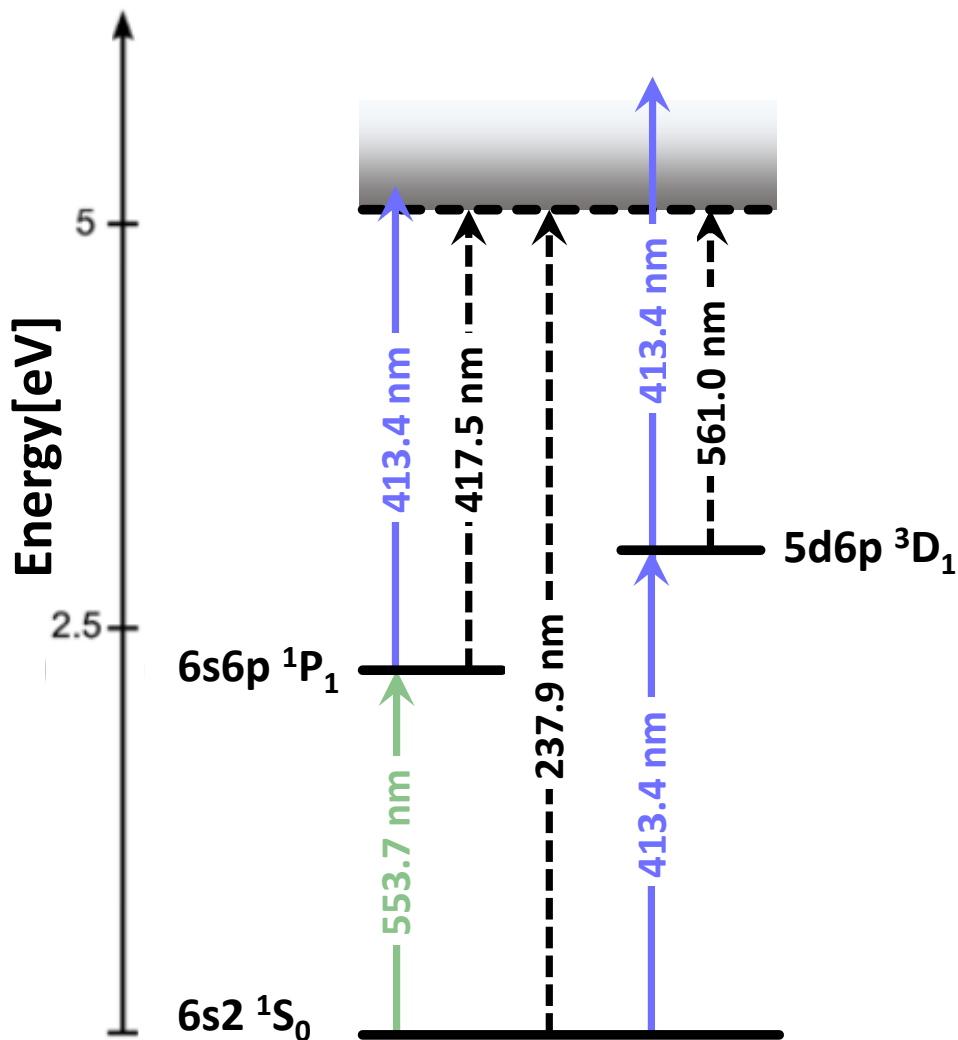


Figure 4.1 Two different ionization process of Ba atom: 413 nm laser only or combine with 553 nm laser. This figure is from Ref.^[91].

4.2 Ion qubits

4.2.1 Zeeman qubits

For $^{138}\text{Ba}^+$ ion shown in Fig. 4.2, the qubit is represented by the two Zeeman levels of the $^2S_{1/2}$ manifold, denoted as $|0\rangle_{\text{Ba}} \equiv |m = +1/2\rangle$ and $|1\rangle_{\text{Ba}} \equiv |m = -1/2\rangle$. The energy gap is $f_{\text{Ba}} = 16.8 \text{ MHz}$ when $B = 6.0 \text{ Gauss}$.

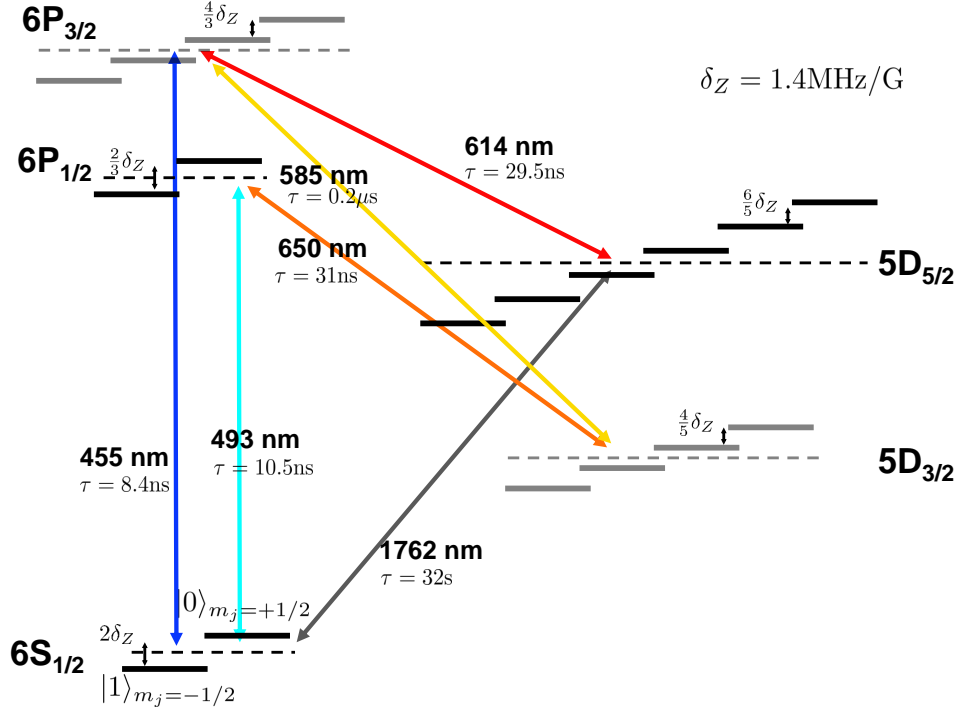


Figure 4.2 Energy levels of $^{138}\text{Ba}^+$.

4.2.2 Optical qubits

Other than the Zeeman qubits of the $^2S_{1/2}$ manifold, the $^2D_{5/2}$ manifold of $^{138}\text{Ba}^+$ ion has a long lifetime up to 32 s and can be used as optical qubit^[67]. The long lifetime also means a narrow linewidth of the transition. So the transitions between $^2S_{1/2}$ and $^2D_{5/2}$ have to be driven by a 1762 nm laser which is locked to a high fineness cavity to get a narrow linewidth below 1 Hz. The Rabi frequency of electric quadrupole transition has a formula of^[92]

$$\Omega^{(E2)} = \left| \frac{eE\omega_0}{2\hbar c} \langle S_{1/2}, m_s | \hat{r}_i \hat{r}_j | D_{5/2}, m_D \rangle \epsilon_i n_j \right|, \quad (4.1)$$

where ω_0 is the transition frequency between $^2S_{1/2}$ and $^2D_{5/2}$. E is the amplitude of laser field. \hat{r} is the position operator of the ion's valence electron. ϵ is the polarization vector.

According to Wigner-Eckart theory, the matrix elements can be written as

$$\langle S_{1/2}, m_S | \hat{r}_i \hat{r}_j | D_{5/2}, m_D \rangle \epsilon_i n_j = \langle S_{1/2} \| r^2 C^{(2)} \| D_{5/2} \rangle \sum_{q=-2}^2 \begin{pmatrix} j & 2 & j' \\ -m_S & q & m'_D \end{pmatrix} c_{ij}^{(q)} \epsilon_i n_j. \quad (4.2)$$

Then the Rabi frequency is

$$\Omega^{(E2)} = \left| \frac{eE\omega_0}{2\hbar c} \langle S_{1/2} \| r^2 C^{(2)} \| D_{5/2} \rangle \sum_{q=-2}^2 \begin{pmatrix} j & 2 & j' \\ -m_S & q & m'_D \end{pmatrix} c_{ij}^{(q)} \epsilon_i n_j \right|. \quad (4.3)$$

The m dependency of Rabi frequency is determined by $g^{(q)} = c_{ij}^{(q)} \epsilon_i n_j$. $\mathbf{B} = (0, 0, B)$ is the magnetic field vector. $\mathbf{k} = k(\sin \varphi, 0, \cos \varphi)$ is the laser wave vector. We assume the laser is a linear polarization and the polarization vector $\epsilon = (\cos \theta \cos \varphi, \sin \theta, -\cos \theta \sin \varphi)$. We can project \mathbf{B} to the plane which is perpendicular to laser direction and get a new vector \mathbf{B}' . Then θ is the angle between ϵ and \mathbf{B}' . φ is the angle between laser direction and magnetic field. And then the Rabi frequencies for different Δm are

$$\begin{aligned} g_{\Delta m=0} &= \frac{1}{2} |\cos \theta \sin 2\varphi|, \\ g_{\Delta m=\pm 1} &= \frac{1}{\sqrt{6}} |\cos \theta \cos 2\varphi + i \sin \theta \cos \varphi|, \\ g_{\Delta m=\pm 2} &= \frac{1}{\sqrt{6}} \left| \frac{1}{2} \cos \theta \sin 2\varphi + i \sin \theta \sin \varphi \right|. \end{aligned} \quad (4.4)$$

In our setup, $\varphi = \pi/4$. The relative Rabi frequencies for different Δm are shown in Fig. 4.3.

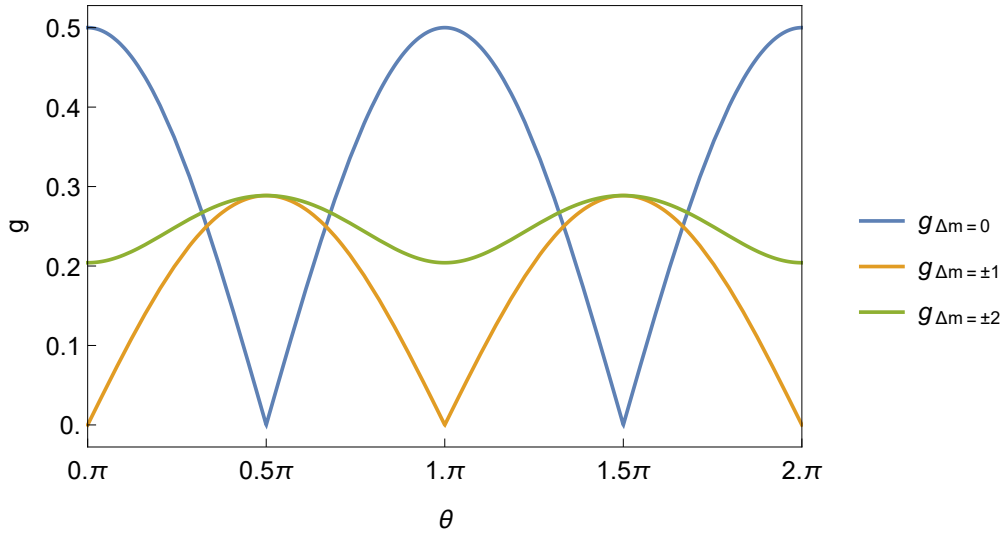


Figure 4.3 Relative 1762 nm Rabi frequencies for different Δm .

4.3 Doppler cooling, state initialization, state detection

For the Doppler cooling of $^{138}\text{Ba}^+$ ion, as shown in Fig. 4.2 and Fig. 4.4, we use red detuned 493 nm lasers to cool the $^{138}\text{Ba}^+$ ion down. 614 nm laser is used to repump $^{138}\text{Ba}^+$ ion from $5D_{5/2}$ state. 650 nm laser is used to repump $^{138}\text{Ba}^+$ ion from $5D_{3/2}$ state.

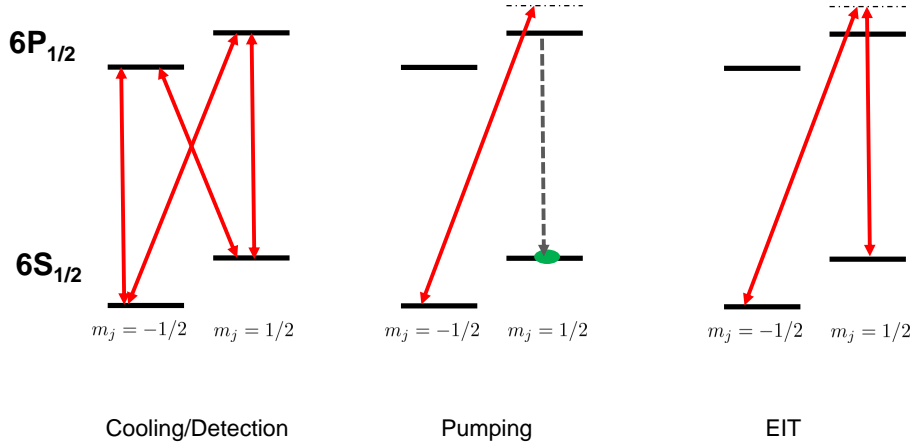


Figure 4.4 Basic operations of $^{138}\text{Ba}^+$ ion.

The $^{138}\text{Ba}^+$ ion state initialization/optical pumping process is realized by polarization design rather than frequency design. A σ_+ 493 nm laser is used to pump all the population to $|0\rangle_{\text{Ba}}$ state.

The state detection process of $^{138}\text{Ba}^+$ is different from $^{171}\text{Yb}^+$ ion since there is no similar energy structure that can be used to distinguish $^{138}\text{Ba}^+$ qubit states. We use the 1762 nm narrow linewidth laser to perform the detection process. One of the qubit states is first shielded to the metastable state $5D_{5/2}$ by 1762 nm laser. Then the detection process can be done by 493 nm laser. As shown in Fig. 4.5, the detection process of $^{138}\text{Ba}^+$ ion is perfect for the bright state, but have an infidelity of 2.10% for the dark state.

4.4 Laser systems

4.4.1 493 nm and 650 nm lasers

The 493 nm laser is used to produce the basic operation beams of $^{138}\text{Ba}^+$ ion. As shown in Fig. 4.6, there are three double pass AOMs in series in the beam pass. AOM 1 shifts the laser frequency by 2×349 MHz to match the reference of tellurium. AOM 2 has three different frequency input: DOP (2×85 MHz), DET (2×90 MHz) and EIT

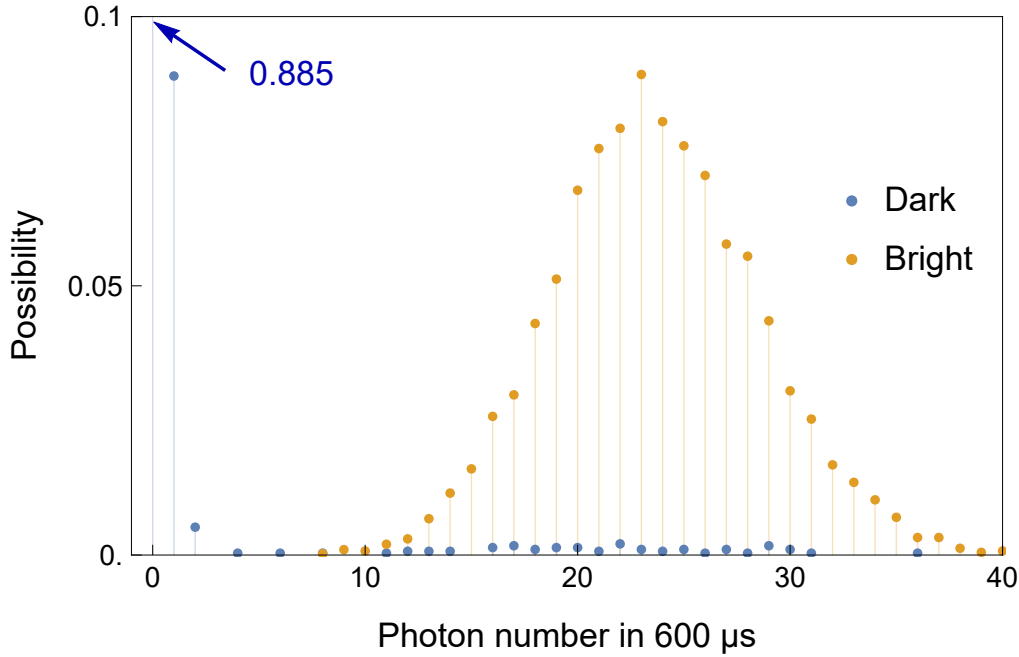


Figure 4.5 Detection photon-count distribution for $^{138}\text{Ba}^+$ dark and bright state.

probe (2×149 MHz), which is benefit from the fact that the output beam direction of double-pass AOM doesn't change with the input RF frequency. AOM 3 has two different frequency input: OPT (2×155 MHz), EIT coupling (2×160 MHz). The output of AOM 2 and AOM 3 are coupled to single-mode fibers and then sent to the trap.

The 650 nm laser is directly divided into three parts after the laser head. The first part is sent to the wavelength meter, and the second part is first shifted by 300 MHz by a fiber EOM, and then sent to an iodine reference table similar to Fig. 3.7. The third part is sent to the trap through fiber.

4.4.2 1762 nm laser

The narrow linewidth 1762 nm laser is used for shelving detection of $^{138}\text{Ba}^+$ ion and optical qubit rotations. We use a high fineness cavity from stable laser system (SLS) to stabilize the laser frequency to below 1 Hz Allan Deviation at 1 s. The optical path for cavity lock is shown in Fig. 4.8 and Fig. 4.9. The output of the NKT fiber laser first goes through a fiber polarization controller, and then passes through a 35 MHz fiber AOM, which is used for the fast frequency stabilization feedback loop. Then only the first-order beam is coupled to the output fiber. The output is then divided into two parts. For the first part, the frequency is shifted by 338.9 MHz and a 5 MHz PDH sideband is added through an optical fiber EOM. Then it goes to the cavity to obtain the PDH lock signal. The other part is sent to the experiment table, where the 1762 nm laser power is first stabilized by

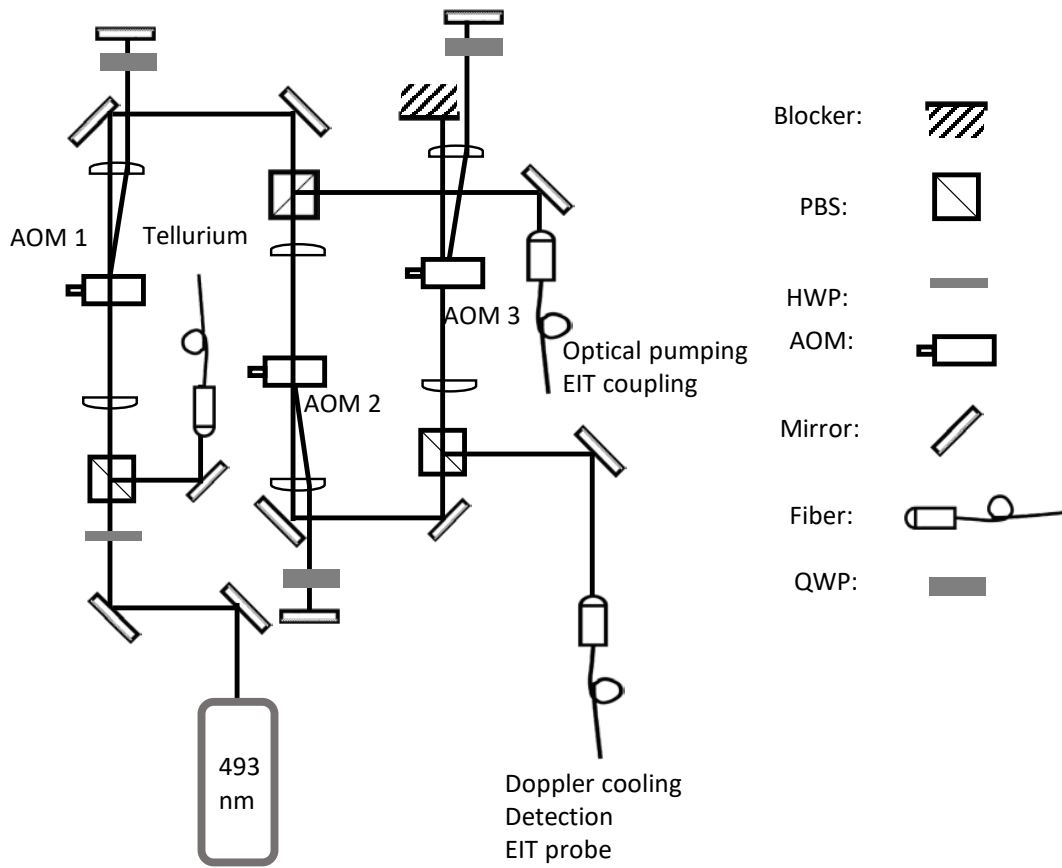


Figure 4.6 Optical paths of 493 nm laser.

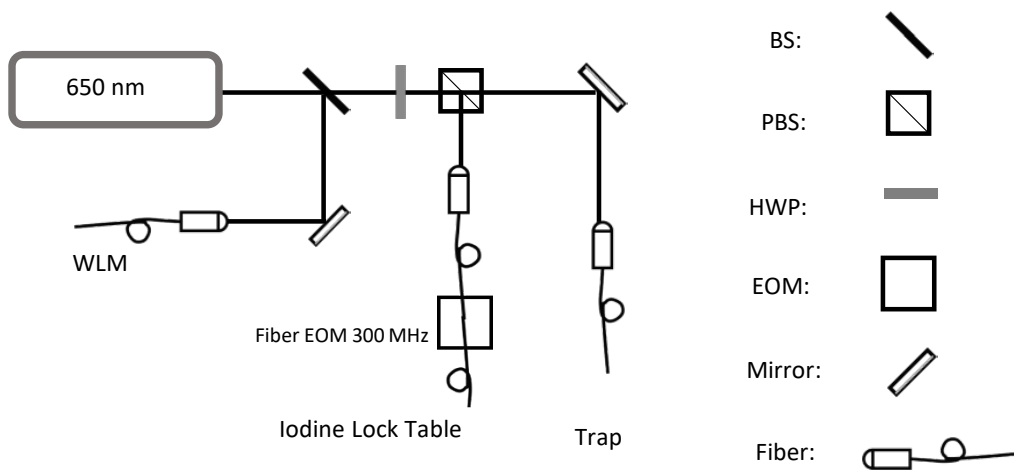


Figure 4.7 Optical paths of 650 nm laser.

a power lock loop shown in Fig. 4.11. Then it passes through another AOM (AOM 2 in Fig. 4.10) with a frequency of around 100 MHz. The zero-order beam is then sent to the wavelength meter (WLM). The -1 order beam is sent to the trap.

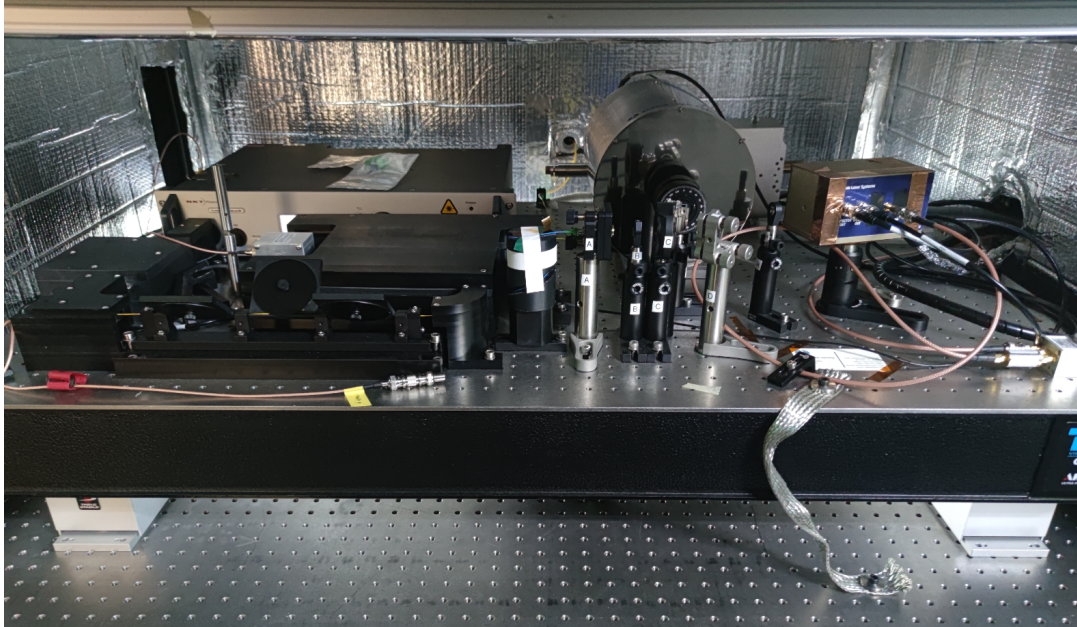


Figure 4.8 1762 nm laser cavity lock system.

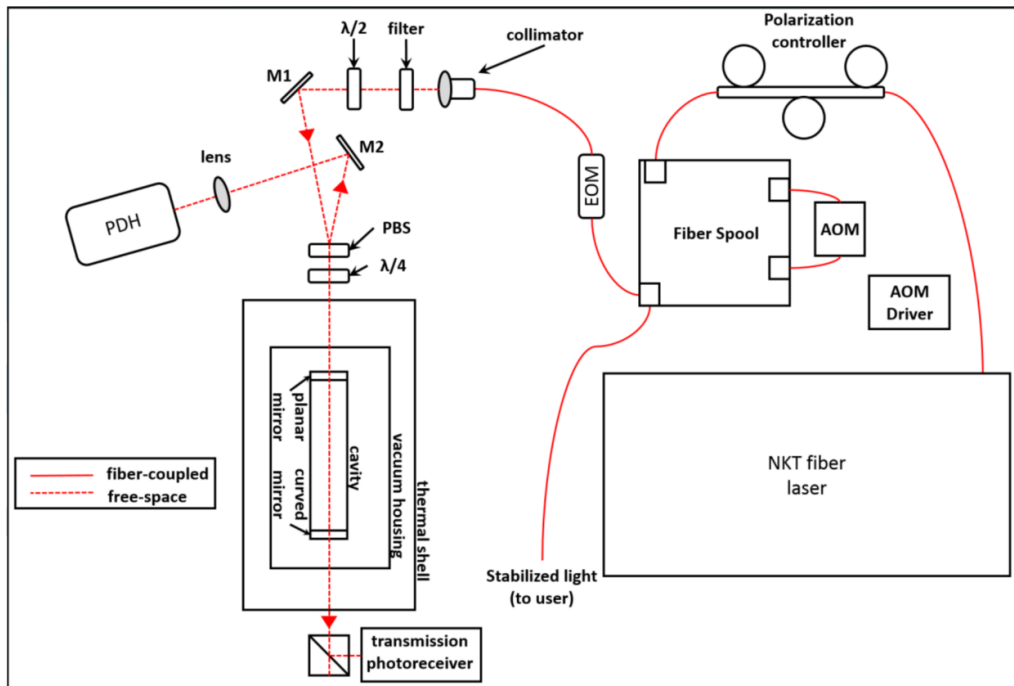


Figure 4.9 Schematic diagram of 1762 nm laser cavity lock system.

For the EOM in the cavity lock beam path, the first order beam of 338.9 MHz is used to shift the lock point. The -1 order beam of AOM 2 is sent to the trap. So the frequency

relation between EOM and AOM is shown in Fig. 4.10. The laser frequency sent to the trap is $f_{\text{trap}} = f_{\text{Lockpoint}} - f_{\text{EOM}} - f_{\text{AOM}}$.

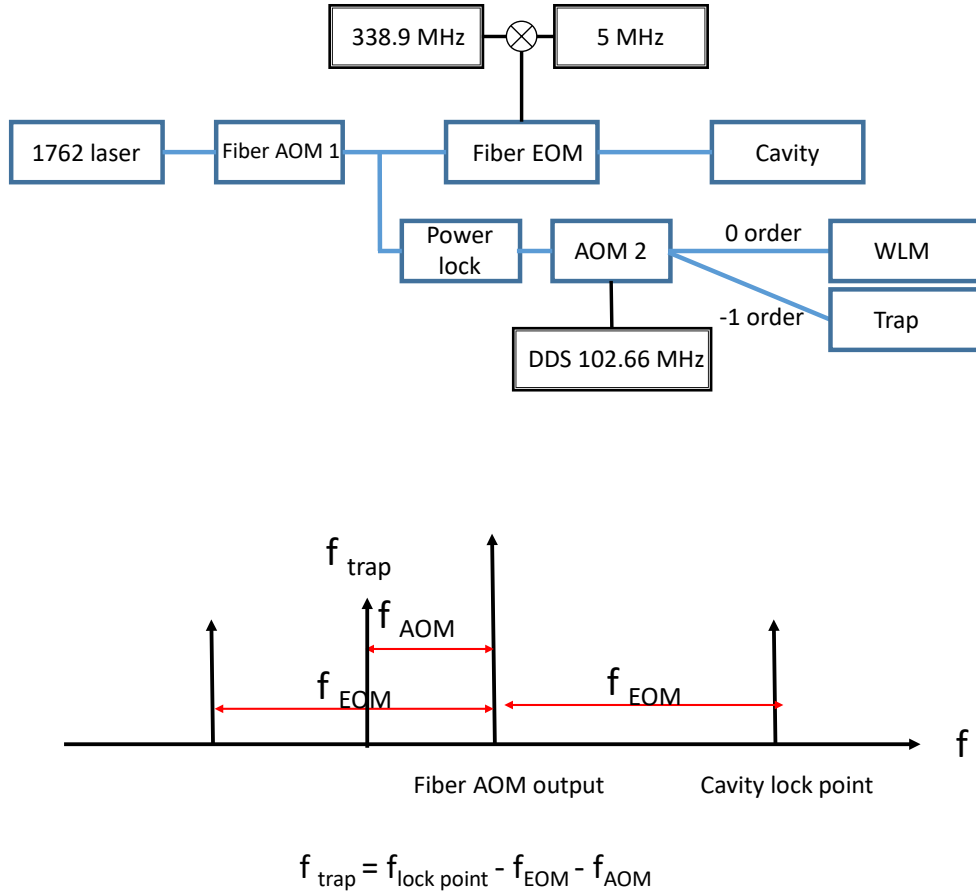


Figure 4.10 Lock frequency of 1762 nm laser.

The output power of 1762 nm laser after the cavity lock fluctuates by 3%. To stabilize the laser power, a power lock loop is used to stabilize the power. As shown in Fig. 4.11, we first use a booster optical amplifier (BOA) to increase the laser power. Then an AOM is added for feedback. A PD after the AOM is used to pick up the power fluctuation signal, and then feedback the signal to the AOM input through a PID server. After the power lock loop, the power fluctuation is reduced to less than 0.5%.

Fig. 4.12 shows the trap mode spectrum measured by 1762 nm laser. The horizontal axis is the frequency relative to carrier transition in MHz. From the left to right, six peaks are two radial out-of-phase (OOP) modes, axial in-phase (IP) mode, two radial IP modes, and axial OOP mode.

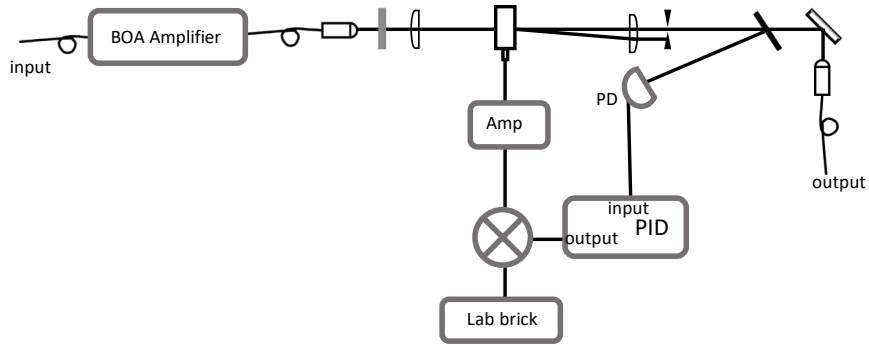


Figure 4.11 Power-lock module of 1762 nm laser.

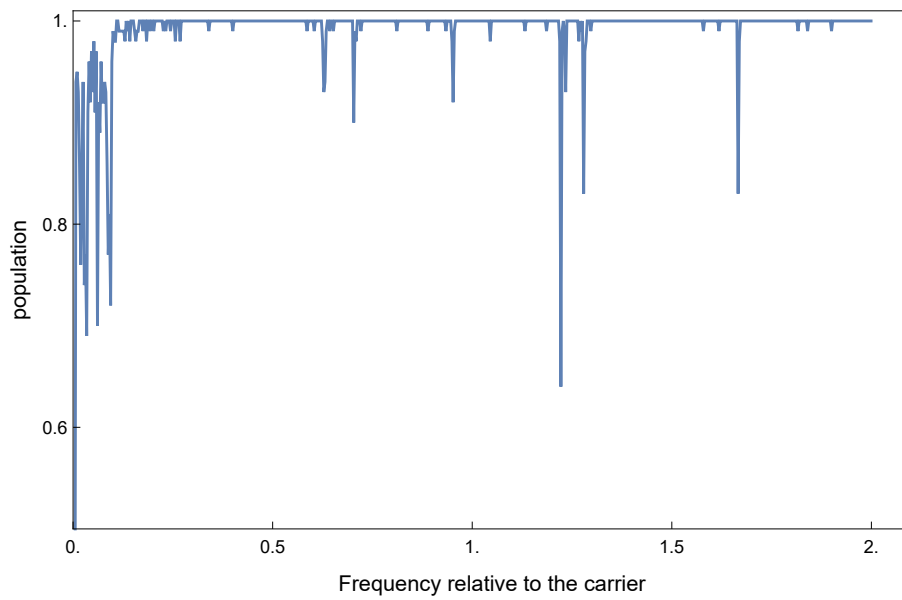


Figure 4.12 Mode spectrum measured by 1762 nm laser.

4.4.3 Raman lasers

We use a HighQ picosecond pulsed laser as the Raman laser for both $^{171}\text{Yb}^+$ ion and $^{138}\text{Ba}^+$ ion, which has three output wavelengths of 1064 nm, 532 nm, and 355 nm. 355 nm laser is used for Raman transition of $^{171}\text{Yb}^+$ ion and 532 nm is used for $^{138}\text{Ba}^+$ ion. The beam path of Raman laser is shown in Fig. 4.13 and Fig. 4.14. The 1064 nm is directly blocked after the output. We have two power lock loops similar to Fig. 4.11 to stabilize the power of 355 nm laser and 532 nm laser. PD 1 and PD 2 are used to monitor the power fluctuations. The two first AOMs in two beam paths of 355 and 532 nm laser are used for laser power feedback. The other two AOMs in each beam path are used to control Raman beams. The optical path difference of each pair of Raman beam is compensated by delay stage. In the end, one 355 nm laser beam and one 532 nm laser beam are combined and then sent to the trap. Fast PD 3 is used for the phase lock loop shown in Fig. 4.15. And slow PD 4 is used to monitor the 80.097 MHz repetition rate signal of the laser.

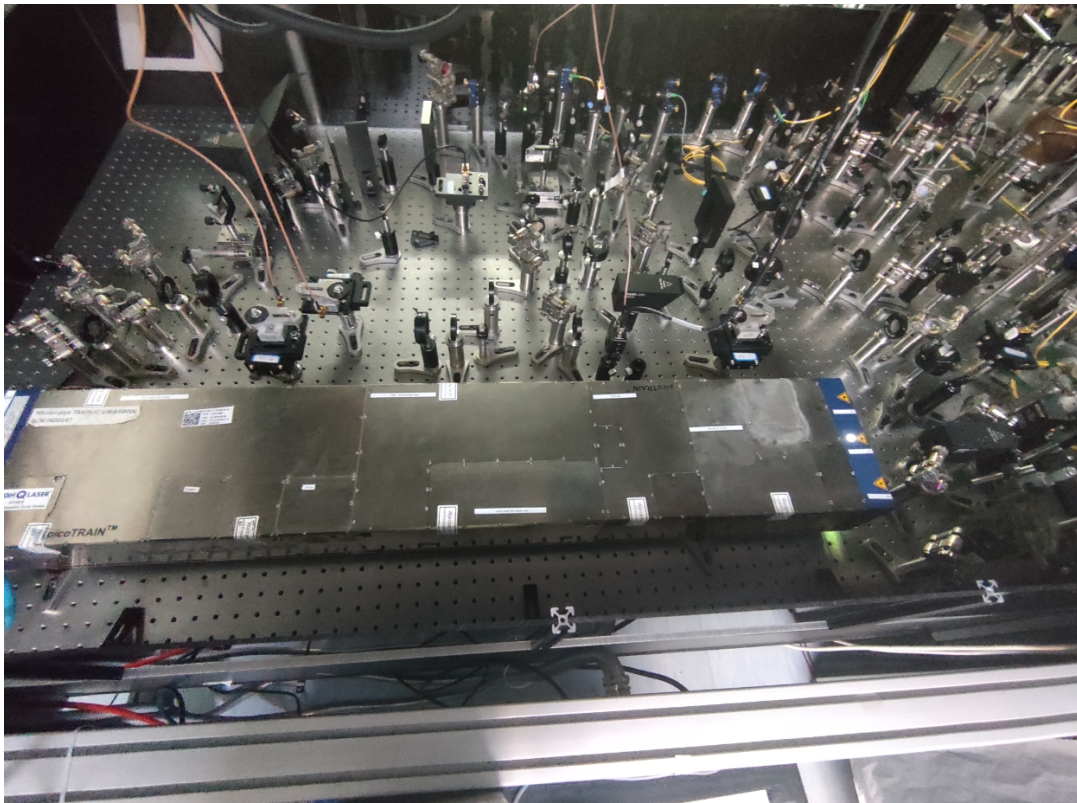


Figure 4.13 Beam path of Raman lasers.

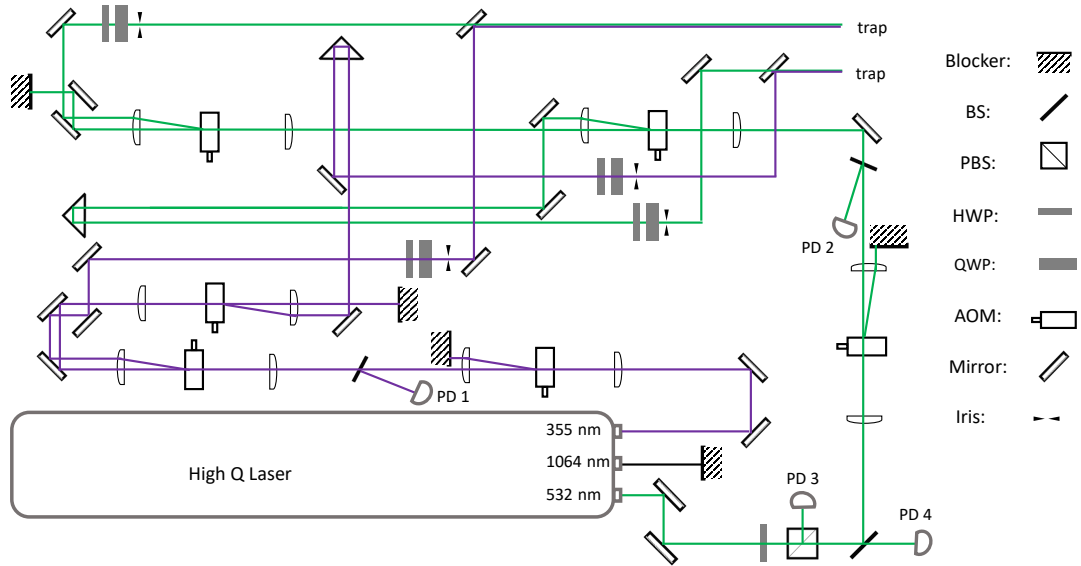


Figure 4.14 Schematic diagram of Raman lasers beam path.

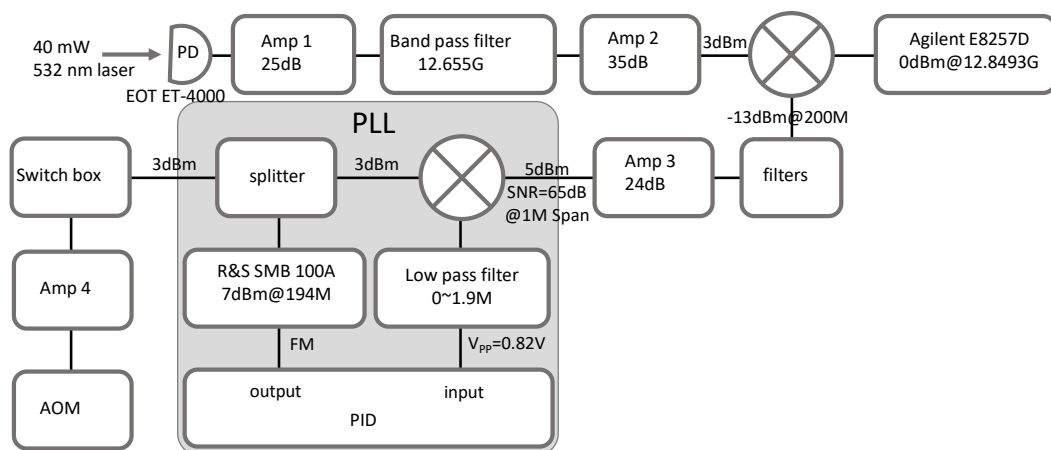


Figure 4.15 Repetition rate drift lock loop.

CHAPTER 5 SINGLE ION QUBIT WITH COHERENCE TIME EXCEEDING ONE HOUR

5.1 Introduction

Quantum coherence is a vital component for scalable quantum computation^[2-4], quantum metrology^[12-13], and quantum communication^[6-10]. In practice, decoherence, loss of coherence in the computational basis, in the quantum system comes from the coupling with the surrounding environment and fluctuations of control parameters in quantum operations, which can lead to the infidelity of quantum information processing, the low sensitivity of quantum sensors, and the inefficiency of quantum repeater based protocols in quantum communication networks. Limited coherence time may also undermine quantum-information applications such as quantum money^[26-27]. It is thus of practical importance to have a stable quantum memory with a long coherence time.

Numerous experimental attempts have been made to enhance the coherence time of quantum memory in a variety of quantum systems. With ensembles of trapped ions and nuclear spins in a solid, coherence time of 10 min^[31-32], and 40 min at room temperature^[28-29] and a few hours at 4 K^[30] have been reported, respectively. For a single qubit quantum memory, which is the essential building-block for quantum computers^[93-94] and quantum repeaters^[73,95], records of coherence time have been reported to the time scale of a minute in trapped ion-qubit^[33-36]. For the coherence time of a minute, the limitation mainly came from the qubit-detection inefficiency^[36,96-97] due to the motional heating of qubit-ions without Doppler laser-cooling. The problem was addressed by sympathetic cooling by other species of ion, which allowed further improvements of coherence time to over 10 min with the support of dynamical decoupling^[37]. While the fundamental limit is far beyond 10 min, however, it remains a major technological challenge to further enhance the quality of a trapped-ion quantum-memory.

Here we address this challenge by improving the coherence time of a $^{171}\text{Yb}^+$ ion-qubit memory from 10 min to over one hour^[69]. This is achieved by identifying and suppressing the three dominant error sources: magnetic-field fluctuation, the phase noise of the local oscillator, and microwave leakage for qubit operation. Furthermore, with the capability of full control on a single qubit, we systematically study the decoherence process of the quantum memory by quantum process tomography. Typically, the deco-

herence process has been characterized by the coherence time T_2 at which the Ramsey contrast, corresponding to the size of the off-diagonal entry in the qubit density-matrix, decays to $1/e$ ^[28-32,37]. We experimentally study the decoherence dynamics by relevant quantum channels of depolarization and dephasing, which allows us to use recently developed coherence quantifiers^[42-43,98]. We also use our data to study recently developed resource-theories of quantum memory and coherence, such as the robustness of quantum memory that quantifies how well a memory preserves quantum information^[99] and relative entropy of coherence that quantifies how much coherence is maintained in the state.

5.2 Experiment details

5.2.1 Ion qubit

Two Species of Atomic Ions. In our experiment, we load one $^{171}\text{Yb}^+$ ion and one $^{138}\text{Ba}^+$ ion in a four-rod Paul trap as shown in Fig.5.1(a). Two hyperfine levels of the $^{171}\text{Yb}^+$ ion in the $S_{1/2}$ manifold are used to encode the qubit with $\{|0\rangle \equiv |F=0, m_F=0\rangle, |1\rangle \equiv |F=1, m_F=0\rangle\}$ and a frequency difference of $12642812118 + 310.8B^2$ Hz, where B is the magnetic field in Gauss. As a sympathetic cooling ion, $^{138}\text{Ba}^+$ is used since it has a similar atomic mass with $^{171}\text{Yb}^+$, which can be used for efficient cooling. We apply Doppler-cooling laser beams on the $^{138}\text{Ba}^+$ ion all the time, which provides continuous cooling for the whole system. In this way, we can measure the final state of the $^{171}\text{Yb}^+$ qubit by standard fluorescence detection technique without losing any detection fidelity^[36,96-97].

5.2.2 Suppression of ambient magnetic field

We suppress the ambient noise of the magnetic field by installing a magnetic-field shielding with a permanent magnet^[100]. We enclose our main vacuum chamber that contains the Paul trap with a two-layer of μ -metal shielding as shown in Fig.5.1(a). By using a fluxgate meter, we observe more than 40 dB attenuation at 50 Hz inside the shielding, which is the main frequency of noise in the lab due to the AC power-line. To generate stable magnetic field of 5.8 G, we replace coils with a $\text{Sm}_2\text{Co}_{17}$ permanent magnet, which has a temperature dependence of $-0.03 \text{ \%}/\text{K}$ ^[100]. The magnetic field strength can be adjusted by changing the position of the magnet from the location of ions. After these modifications, we observe the coherence time of the field-sensitive Zeeman qubit is increased to more than 30 ms. We study the noise spectrum by dynamical decoupling

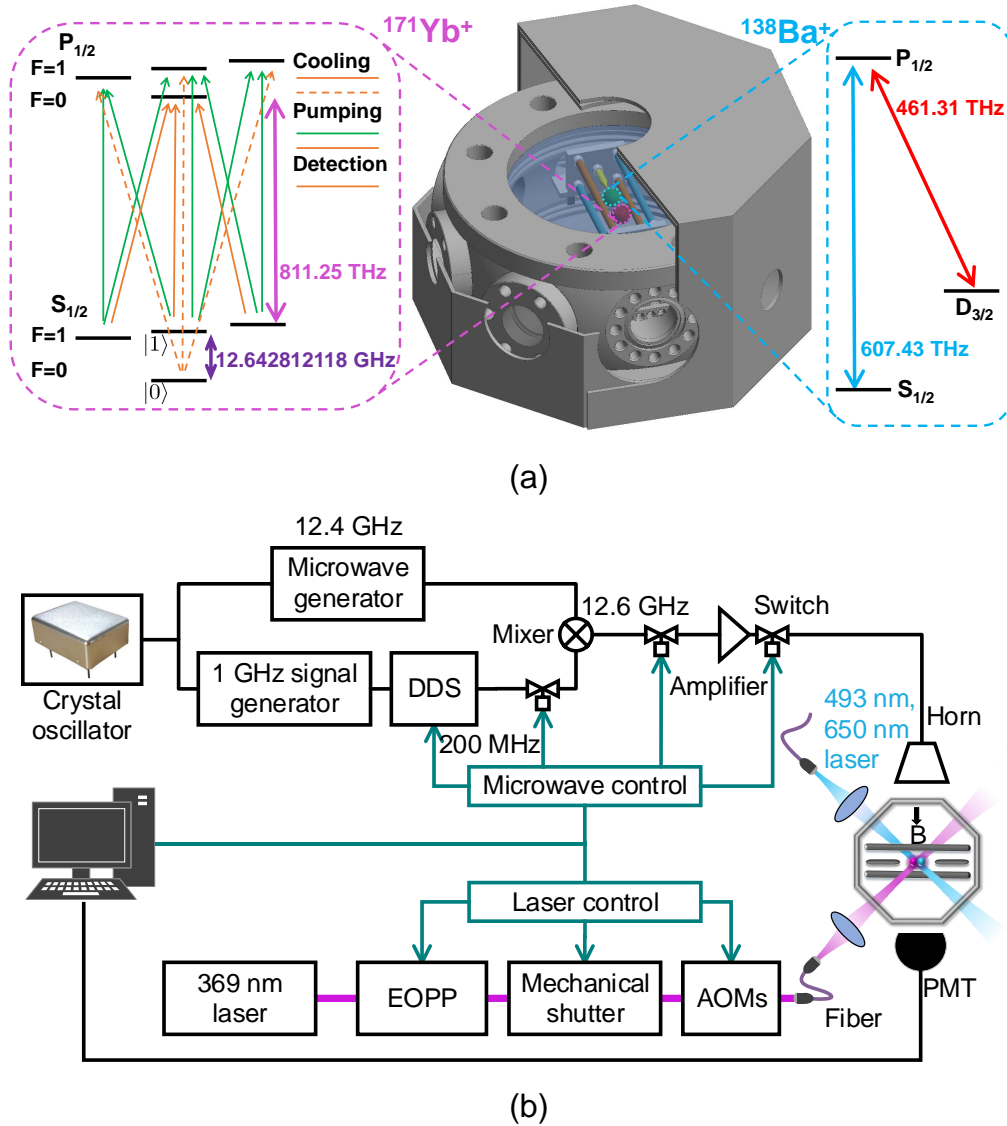


Figure 5.1 Experimental setup. (a), Energy levels of $^{171}\text{Yb}^+$ and $^{138}\text{Ba}^+$ ion and cutaway view of the μ -metal shielding enclosing octagon chamber. The shielding has ten holes, where two holes for connection of the vacuum pump and helical resonator and the other eight holes with diameter from 20 mm to 40 mm for the access of laser beams, microwave and imaging system. (b), The schematic diagram for the control of microwave and laser beams. We use a crystal oscillator (SIMAKE SMK36270CHFM OCXO) to reference the microwave generator and Direct Digital Synthesize (DDS) through a 1 GHz signal generator. The microwave of 12.6 GHz is generated by mixing 200 MHz signal from DDS and 12.4 GHz from the microwave generator, which is amplified and applied to ions through a horn. All three microwave switches are used to reduce microwave leakage. For 369 nm laser beams, we use acousto-optic modulators (AOMs) to generate basic operating lasers. We use Electro-Optic pulse picker (EOPP), mechanical shutter and single-mode fiber to reduce laser leakage. The magnetic field direction is in the radial direction. We detect the qubit state with a photomultiplier tube (PMT).

sequences^[101-102] and observe that noise of 50 Hz and 150 Hz are below 16 μG and 32 μG , respectively.

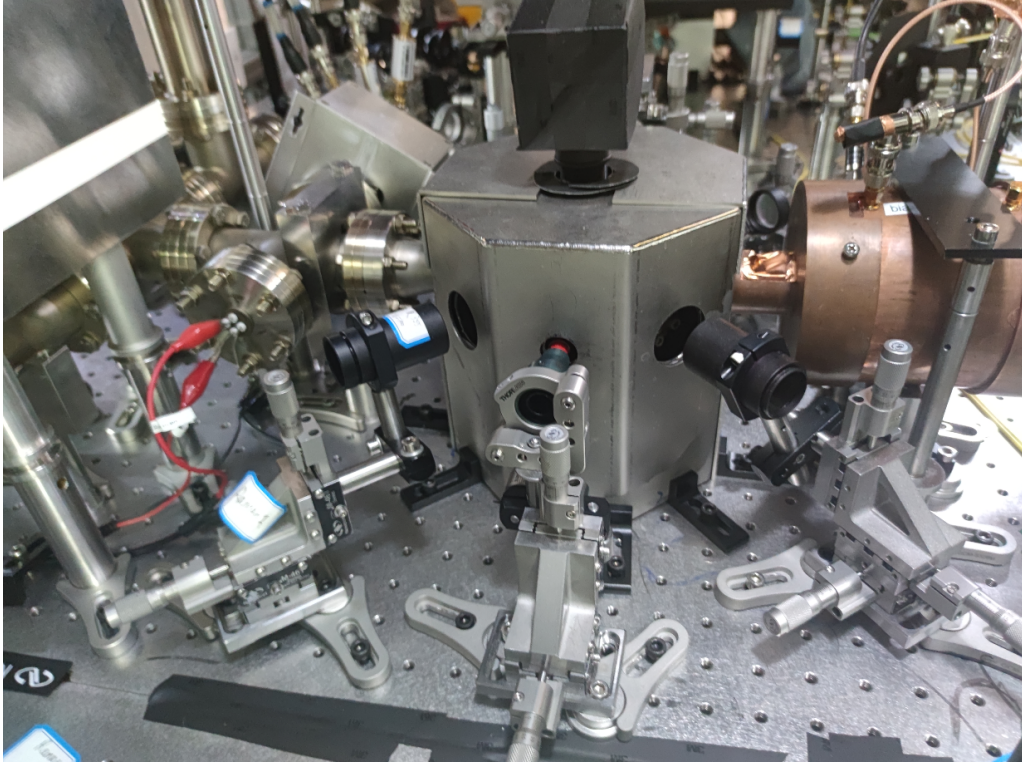


Figure 5.2 Magnetic field shielding.

5.2.3 Improvements of microwave frequency-stability

We perform coherent manipulation of the qubit by applying a resonant microwave. Qubit coherence is typically measured by the contrast of Ramsey fringe, which requires control and interrogation of the system by a local oscillator that can bring in phase noise^[103-104]. In our case, this part of the noise is determined by the microwave signal generator and its reference. For microwave signal, phase noise in the low-frequency regime is mainly determined by those of the reference signal. We use a crystal oscillator as the reference, which has an order-of-magnitude smaller Allan variance at 1 s observation time than our previous Rb clock oscillator^[37].

5.2.4 Suppression of microwave power-leakage

We also find that leakage of the microwave can introduce relaxation of the qubit memory. We include a microwave switch after amplifier as shown in Fig. 5.1(b), which reduces the leakage by over 70 dB. In total, we suppress the microwave output by 164 dB

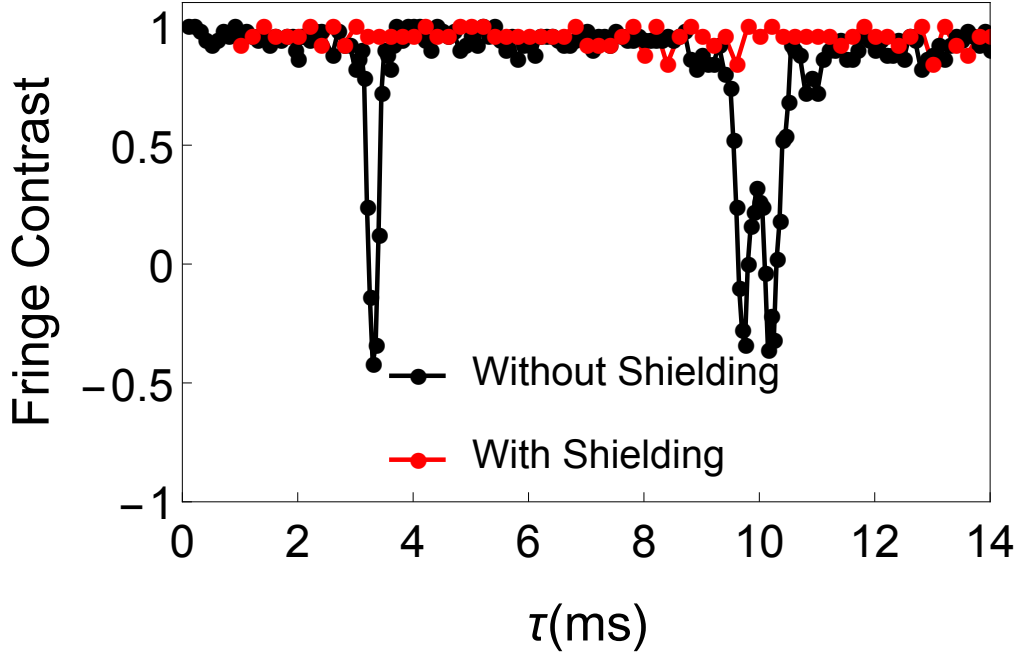


Figure 5.3 Suppression of magnetic-field noise. To check the noise suppression of magnetic-field shielding, we use 31 CPMG (Carr, Purcell, Meiboom and Gill) pulses to accumulate the AC magnetic-field noise^[37]. The figure shows Ramsey contrast as a function of the inter-DD pulse spacing τ . Black and red points represent data without and with shielding and permanent magnet^[37], respectively. Before the improvement of magnetic field stability, there are two dips at $\tau = 3.3$ ms and $\tau = 10$ ms which correspond to 150 Hz and 50 Hz noise, respectively, which disappeared after the improvement. We further increase the CPMG pulses number to 190, and get fringe contrasts of 0.97 and 0.98 at $\tau = 10$ ms and 3.3 ms, respectively. This indicates that the level of the noise at 50 Hz and 150 Hz are below 16 μG and 32 μG , respectively.

after turning off all the switches. With π pulse duration of 175 μs , the effect of leakage is negligible for 0.4 s pulse interval time, which would be further suppressed by dynamical decoupling pulses. At the same time, we also use AOMs, EOPP and a mechanical shutter to suppress the leakage of $^{171}\text{Yb}^+$ ion resonant laser beams as same as Ref.^[37].

5.2.5 Dynamical decoupling pulse sequence

We measure the coherence time of the $^{171}\text{Yb}^+$ ion-qubit by observing the dependence of Ramsey contrasts on the storage time. The experimental sequence is shown in Fig. 5.4. As discussed above, cooling laser beams for $^{138}\text{Ba}^+$ are applied during the whole sequence. We initialize the state of the $^{171}\text{Yb}^+$ ion-qubit to $|0\rangle$ by the standard optical pumping technique, apply the $\pi/2$ -Ramsey pulses, and detect the probability in $|1\rangle$ state by the standard state-dependent fluorescence method. In the Ramsey measurement, we observe the coherence time of 1.6 s. We note that we have a detection efficiency of 98.6%, which is corrected by the calibrated error magnitude with the uncorrelated error

assumption as shown in Ref.^[105].

To enhance coherence time, we first apply a spin-echo pulse that uses single π pulse to compensate low-frequency noise. We observe the coherence time is improved to 11.1 s with the single spin-echo pulse. Then, we apply the dynamical decoupling scheme^[29-30,37,101-102,106-107], which contains multiple of spin-echo pulses. Performance of dynamic decoupling pulses is described by the filter function $\tilde{y}(\omega, T) = \frac{1}{\omega} \sum_{j=0}^{T/\tau} (-1)^j (e^{i\omega t_j} - e^{i\omega t_{j+1}})$, with $t_0 = 0$, $t_{(T/\tau)+1} = T$, $t_j = (j - 0.5)\tau$ when $1 \leq j \leq T/\tau$, and τ is the interval of pulses. Then Ramsey fringe contrast^[101] is $W(T) = e^{-\frac{2}{\pi} \int_0^\infty S(\omega) |\tilde{y}(\omega, T)|^2 d\omega}$ with $S(\omega)$ being the noise spectrum density. In our experiment, we use KDD_{xy}(Knill dynamical decoupling)^[30,37,107] pulses, where all the pulses are equally spaced and have periodic phases as shown in Fig. 5.4. The filter function of the KDD_{xy} pulses has a peak at the frequency of $\omega = \frac{\pi}{\tau}$. Most of the noise is suppressed except the part with frequencies around the peak, which is instead amplified. When the total time T is fixed, the position of the peak is determined by the pulse interval, which can be optimized depending on the noise spectrum. After comparing different parameters, we choose 0.4 s as the pulse interval, which leads to the peak of the filter function at $2\pi \times 1.25$ Hz.

5.3 Experiment results

5.3.1 Coherence time

With different initial states, we show the time dependence of the Ramsey contrast up to 960 s in Fig. 5.5. By assuming exponential decay of the Ramsey contrast, we find the coherence time of states $|0\rangle$ and $|1\rangle$ to be 16000 ± 3200 s. Other four superposition states ($\phi = 0, \frac{\pi}{2}, \pi$, and $\frac{3\pi}{2}$ shown in the legends of Fig. 5.5) have a coherence time of 5500 ± 670 s. Both of the uncertainties are from fitting errors. As shown in the inset of Fig. 5.5, the coherence time is increased by an order-of-magnitude compared to the previous state-of-the-art result^[37].

5.3.2 Experimental study of decoherence process

We further analyze the decoherence process by performing quantum process tomography, which completely characterizes unknown dynamics of a quantum system, at different storage time following the Refs.^[38,108]. The procedure of quantum process tomography is as follows. For a quantum process ε , we consider its process χ matrix, which is defined

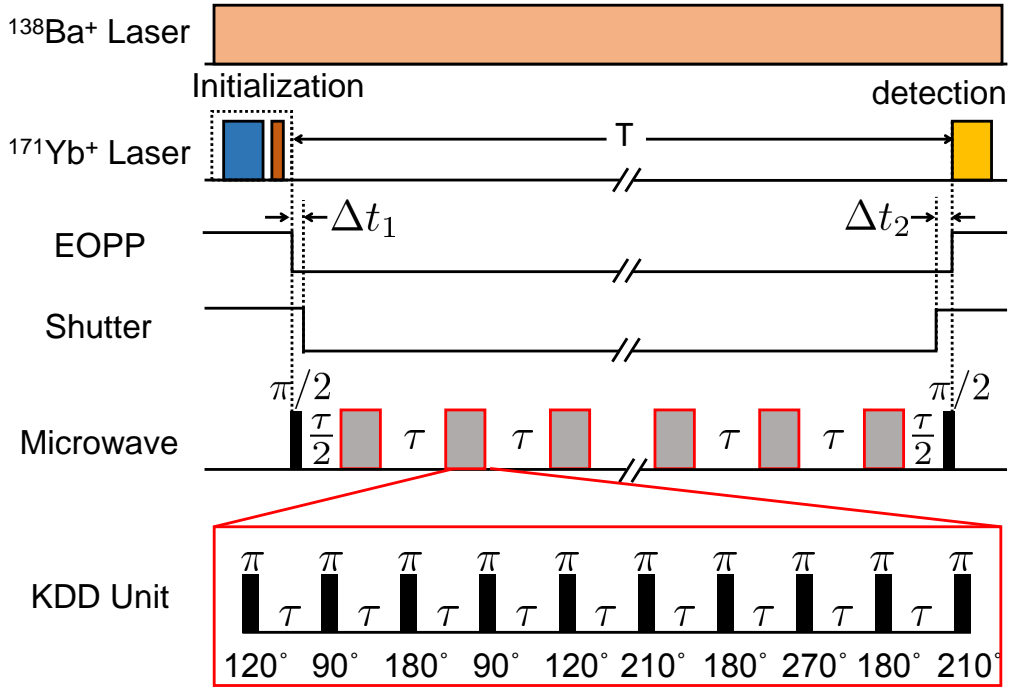


Figure 5.4 Experimental sequence. Cooling laser beams for the $^{138}\text{Ba}^+$ ion are applied during the whole sequence. For $^{171}\text{Yb}^+$ ion, we first initialize the qubit and then start to apply the microwave pulses. All the KDD_{xy} (Knill dynamical decoupling) pulses are inserted between two $\pi/2$ pulses of Ramsey sequence. Blue and brown blocks represent Doppler cooling and optical pumping pulses for $^{171}\text{Yb}^+$ ion. EOPP and shutter are closed after state initialization and opened before state readout, where the time delays between them are shown as $\Delta t \approx 10$ ms, which is mainly caused by the limited speed of the mechanical shutter. Gray blocks represent KDD_{xy} units. T is the total measurement time, and τ is the interval of pulses. Each KDD_{xy} unit has ten π pulses, where the first and the second five pulses represent σ_x - and σ_y -rotation, respectively. Therefore, the second five pulses have 90° phase shift from the first five. We choose the total number of KDD_{xy} units even to make sure all the KDD_{xy} pulses are identity operation in the ideal case. In the end, we use a detection laser pulse to measure the qubit state.

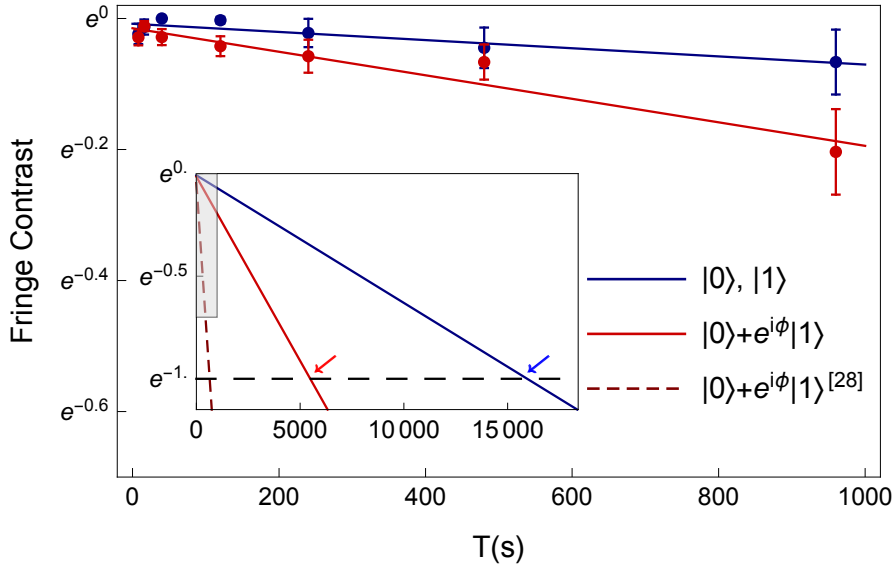


Figure 5.5 The evolution of Ramsey fringe contrast. Blue points are from the initial states of $|0\rangle$ and $|1\rangle$, and red points are from $|0\rangle + |1\rangle$, $|0\rangle + i|1\rangle$, $|0\rangle - |1\rangle$, and $|0\rangle - i|1\rangle$, where $\phi = 0, \frac{\pi}{2}, \pi$, and $\frac{3\pi}{2}$, respectively. Error bars are standard deviations. Each initial state at each data point repeats 30 to 100 times. The solid lines are the fitting results by the exponential decay function. Inset shows extrapolations of fits in a longer time range. The shadow indicates the enlarged area in the figure. The red-dashed line indicates the previous result of superposition states^[37]. The black-dashed line indicates the $1/e$ threshold. The red and blue arrows indicate times when threshold are reached.

by $\varepsilon(\rho) = \sum_{mn} \chi_{mn} \hat{E}_m \rho \hat{E}_n^\dagger$ with $\hat{E}_m \in \{\hat{I}, \hat{X}, \hat{Y}, \hat{Z}\}$ ^[38]. We measure the χ matrix of our single ion-qubit memory by preparing four different input states $|0\rangle$, $|1\rangle$, $(|0\rangle + |1\rangle)/\sqrt{2}$, $(|0\rangle + i|1\rangle)/\sqrt{2}$, applying the memory, and finally measuring the output states with four measurements I , X , Y and Z . We use the maximum likelihood method to reconstruct the process matrix^[108]. We observe the time dependence of the process matrix as shown in Fig. 5.7(a). The ideal process of quantum memory is described by $\chi_{mn}^{\text{id}} = \delta_{m,1}\delta_{n,1}$. With the experimentally measured process matrix χ^{exp} , we can obtain the process fidelity $F_p = \text{Tr}(\chi^{\text{id}} \chi^{\text{exp}}) = \chi_{11}^{\text{exp}}$. The infidelity mainly comes from the dephasing and depolarization effects. The process with these two noises can be described by the following matrix as

$$\begin{bmatrix} \frac{1+2e^{-t/T_2}+e^{-t/T_1}}{4} & 0 & 0 & 0 \\ 0 & \frac{1-e^{-t/T_1}}{4} & 0 & 0 \\ 0 & 0 & \frac{1-e^{-t/T_1}}{4} & 0 \\ 0 & 0 & 0 & \frac{1-2e^{-t/T_2}+e^{-t/T_1}}{4} \end{bmatrix}, \quad (5.1)$$

where T_1 and T_2 are depolarizing and total dephasing time, respectively^[39-40]. The process matrix describes a quantum memory with full coherence at $T = 0$ but which has

transitioned to a fully mixed state for $T \gg \min(T_1, T_2)$. By fitting the experimental process tomography results with the above process matrix of Eq. (5.1), we obtain $T_1 = 12000 \pm 2200$ s and $T_2 = 4200 \pm 580$ s. We also plot the model of Eq. (5.1) and the experimental data in Fig. 5.7(a).

Process matrix evolution. We obtain the T_1 and T_2 in the diagonal elements of χ of Eq. (5.1) by fitting $\chi_{XY} \equiv 0.5(\chi_{22} + \chi_{33})$ and $\chi_{IZ} \equiv 1 - (\chi_{11} - \chi_{44})$ to the functions of $\frac{1-e^{-t/T_1}}{4}$ and $1 - e^{-t/T_2}$, respectively. As shown in Fig. 5.6, we obtain $T_1 = 11900 \pm 2200$ s and $T_2 = 4200 \pm 580$ s by fitting χ_{XY} and χ_{IZ} , respectively.

We note that ideally the total dephasing time $T_2 = 4200 \pm 570$ s in the process tomography should be matched to the coherence time of 5500 ± 670 s. The discrepancy originates from the quantum fluctuation noise in the other bases measurements of the process tomography. The process tomography requires measurements of four different bases for different input-states. For example, a superposition input-state, $(|0\rangle + |1\rangle)/\sqrt{2}$ (an eigenstate of σ_x), we need to measure the expectation values of identity, σ_x , σ_y , and σ_z . In principle, both $\langle\sigma_y\rangle$ and $\langle\sigma_z\rangle$ should be zero (even there exists serious decoherence). However, due to the quantum fluctuation noise, they deviated from zero, which introduced the reduction of the T_2 in the process tomography in our measurement. If these results are zero, the Ramsey coherence time and the total dephasing time of the process tomography will be perfectly matched. We believe if the number of measurements for the process tomography approaches infinity, the difference should converge to zero.

From the experimental result of quantum process tomography, the performance of the quantum memory on arbitrary quantum states can be accurately estimated, which can be simplified as the mean fidelity, $F_{\text{mean}} = \langle\text{Tr}(\rho\varepsilon(\rho))\rangle_\rho$, which is the averaged output fidelity with all possible input states ρ ^[109-111]. The mean fidelity is a function of wait time T since the process matrix of quantum memory is different depending on wait time T. We use the Monte Carlo method to get the mean fidelity with 10^5 different input states, generated by uniformly sampled random unitary operations according to the Haar measure^[112-113]. As shown in Fig. 5.7(a), we obtain the coherence time, the time constant of fitted exponential decay-function, 5200 ± 500 s for the mean fidelities. We note that within the error bar, this coherence time is consistent with that of a simple estimation of the mean fidelity from the formula of $F_{\text{mean}} = (2F_p + 1)/3$ ^[109], where it provides 5600 ± 650 s.

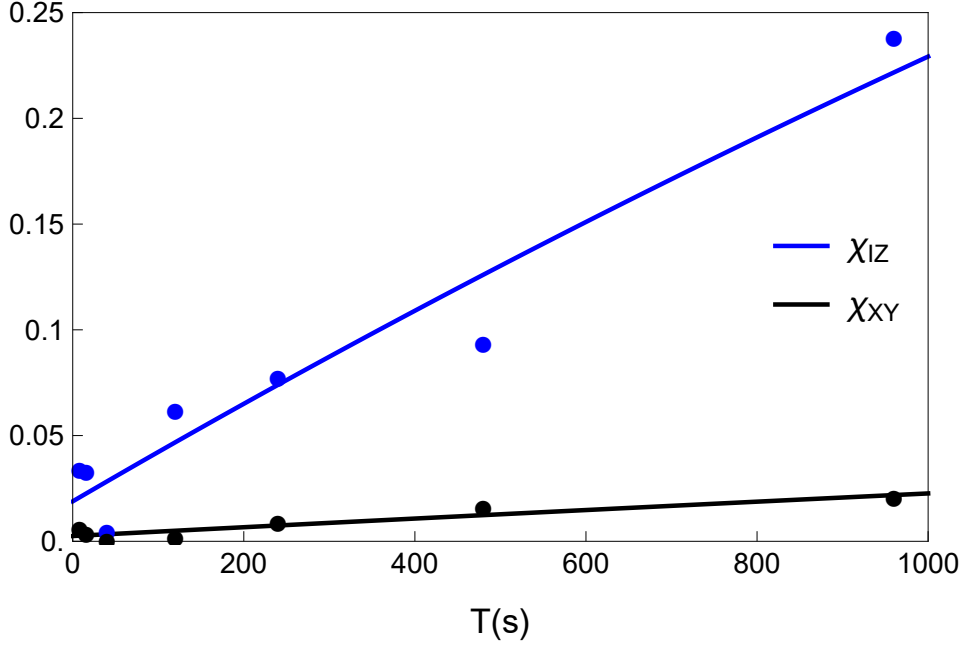


Figure 5.6 Fitting of process matrix elements evolution. Blue and black points are experimental results of χ_{Iz} and χ_{XY} , respectively. The solid lines are their fitting results.

5.3.3 Benchmark of quantum memory and quantum coherence

Recently due to the fundamental importance of quantum coherence, there have been serious developments of rigorous theories of quantum coherence and quantum memory as a physical resource. In our manuscript, we relate our experimental results to up-to-date resource theories of quantum coherence and quantum memory such as relative entropy of coherence (REC) and robustness of quantum memory (RQM), respectively.

5.3.3.1 Relative Entropy of Coherence

The relative entropy of coherence (REC) is a distance-based coherence quantifier, which is suggested as a gold standard measure^[109]. The REC can be interpreted as the minimal amount of noise required for making a quantum state fully decohere^[43]. The REC has the same formula with distillable coherence, which has an analogy to the distillable entanglement, a standard widely-using entanglement quantifier. The distillable coherence is the optimal number of maximally coherent single-qubit states that can be obtained in a given qubit state through incoherent operations. It fulfills all the requirements as a proper coherence quantifier as suggested in Ref.^[43]. The formal definition of the REC^[42] is written as $C(\rho) = S(\Delta(\rho)) - S(\rho)$, with $\Delta(\rho) = \sum_i \langle i | \rho | i \rangle | i \rangle \langle i |$, $\{|i\rangle\}$ being the computational basis, and $S(\rho) = -\text{Tr}(\rho \log_2 \rho)$ being the Von Neumann entropy.

In our analysis, we use the ratio of the REC between the output state and the input

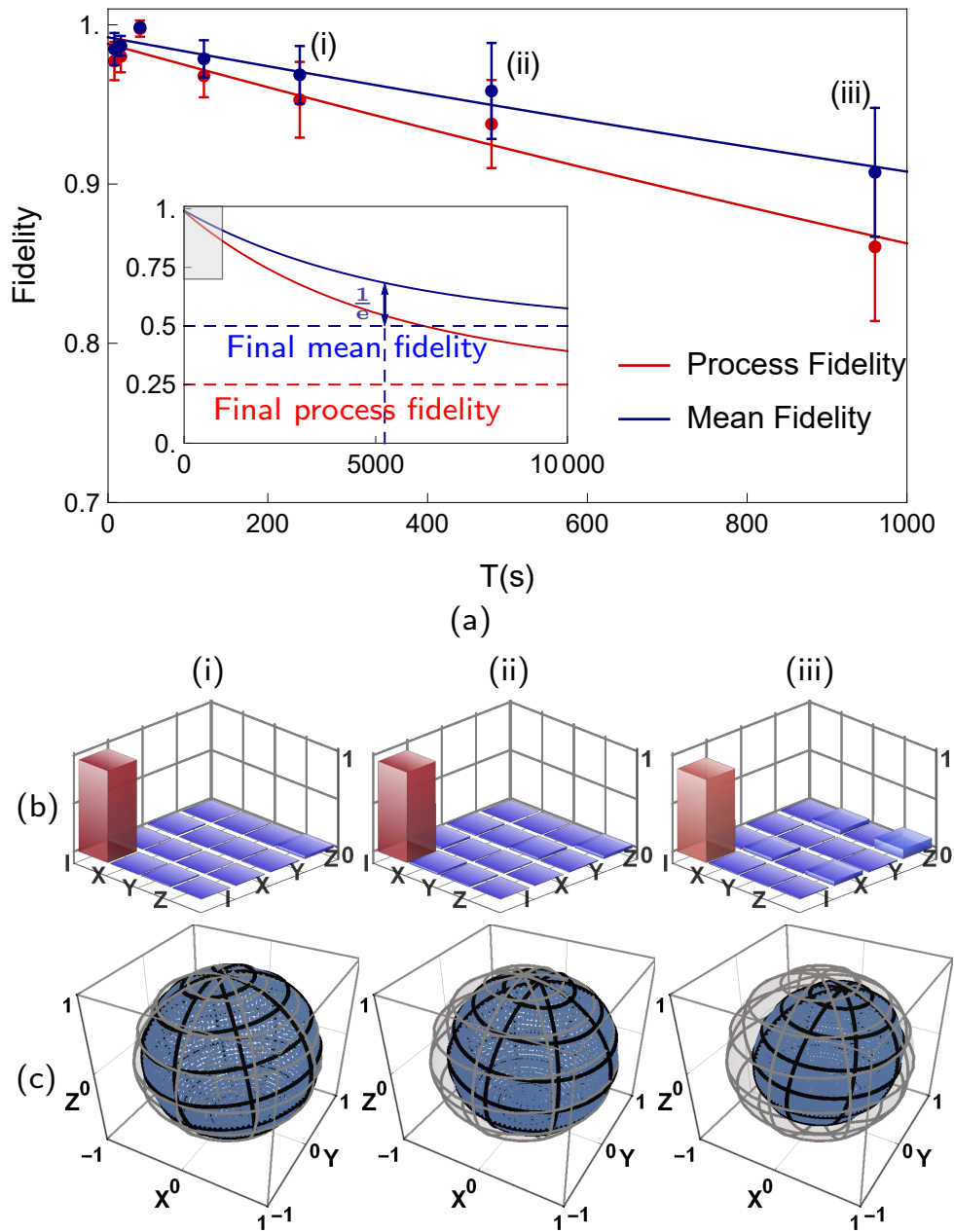


Figure 5.7 Results of quantum process tomography. (a), Red and blue points represent process and mean fidelities, respectively. Error bars are standard deviations. The red line is the fitting result of Eq. (5.1). The blue line is the fitting result of the exponential decay function. Inset shows extrapolations of fits in a longer time range. The shadow indicates the enlarged area in the figure. The red and blue dashed horizontal lines indicate the process fidelity and mean fidelity of the final state, where the system lost all the quantum information. The blue vertical line indicates the time point when mean fidelity decays to $1/e$ threshold. (b), The real part of the process matrix after a storage time of (i): 4 min, (ii): 8 min and (iii): 16 min. The largest diagonal element of the process matrix is the identity operation part, χ_{11}^{exp} , which is the process fidelity F_p . (c), State evolution represented in the Bloch sphere after a storage time of (i): 4 min, (ii): 8 min and (iii): 16 min. Gray meshed spheres represent the initial pure states, which form the Bloch sphere. And blue spheres represent the output states after corresponding storage time, which are the same as the input state at $T = 0$ but shrink into the Bloch sphere later and transition to a dot in the center for $T \gg \min(T_1, T_2)$. Given the input state, the corresponding output state is calculated by the process matrix χ^{exp} .

state instead of directly using the REC because each input state has a different value of the REC. Based on the process matrix χ^{exp} , we numerically calculate the ratio of the REC. We study the time-dependence of the mean ratio of the REC $C'_{\text{mean}} = \langle C(\varepsilon(\rho))/C(\rho) \rangle_{\rho}$, where we average over 10^5 random input states. Note that we only consider states with REC larger than 0.01. As shown in Fig. 5.8, the mean REC ratio decays to $1/e$ after 3500 ± 1100 s by the exponential fitting. The relatively short duration and the large fluctuation of the results mainly stem from stringent condition and sensitivity of the REC to small errors in the process matrix.

5.3.3.2 Robustness of Quantum Memory

The robustness of quantum memory (RQM), which was introduced by the Ref.^[99], quantifies how well the memory preserves quantum information that includes coherence. Here the quantum memory, which stores a quantum state for later retrieval, is considered as a channel that maps an input state to an output state. Ideally, it should be an identity channel. The quantifier of RQM is developed based on the approach that considers the quantum memories as a resource and provides a means to benchmark quantum memories. Basically, the higher the RQM is, the more noise the quantum memory can sustain before it is unable to preserve quantum information. In contrast, a classical memory that cannot preserve quantum information is characterized as a measure-and-prepare (MP) memory that destroys the input state by measurement, and stores only the classical measurement result.

The RQM is defined as the least portion of the classical memory that needs to be mixed with the quantum memory so that the resultant mixture belongs to MP memory, which is formally written as $R(\mathcal{N}) = \min_{\mathcal{M} \in \mathcal{F}} \left\{ s \geq 0 \left| \frac{\mathcal{N} + s\mathcal{M}}{s+1} \in \mathcal{F} \right. \right\}$, where \mathcal{N} is the quantum memory of interest, \mathcal{M} is a classical memory that is in the set of MP memories \mathcal{F} , and s is the amount of mixture of the quantum memory \mathcal{N} with the classical memory \mathcal{M} . The RQM is the minimum value of s to make the mixed memory in \mathcal{F} . We note that the RQMs of all classical memories are zero since the MP memories cannot maintain quantum information. We obtain the RQM from the experimental process matrix. In general, the $R(\mathcal{N})$ can be found by a numerical search of the minimum s . Assuming off-diagonal elements in the process matrix are negligible, the RQM can be simplified to $\max\{2F_p - 1, 0\}$ for the case of qubit quantum-memory. In our experimental process tomography, no noticeable difference is observed between the numerical search and the simplified formula. As shown in Fig. 5.8, the RQM of our system lasts 6300 s before it

decays to zero by the exponential fitting.

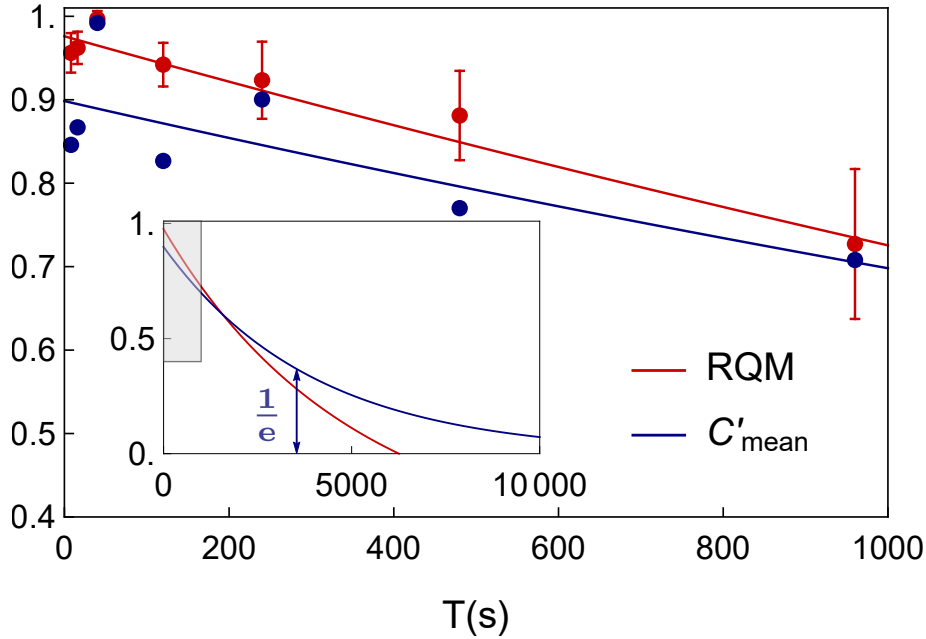


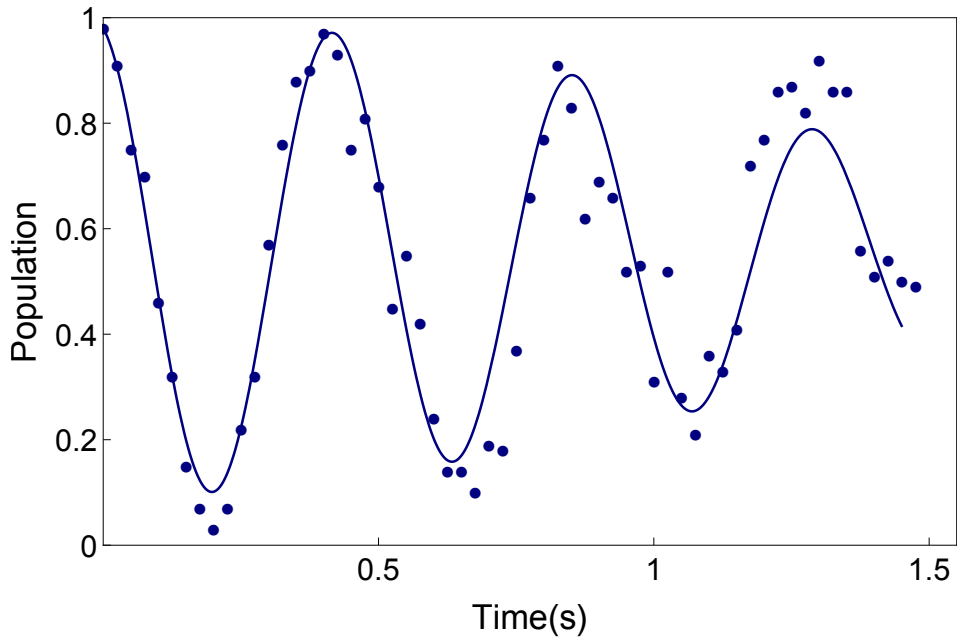
Figure 5.8 Benchmark of quantum memory and coherence. Red and blue points are data of the robustness of quantum memory (RQM) and the mean ratio of the relative entropy of coherence (REC), respectively. Error bars are standard deviations. The red line is the theoretical result of the RQM calculated from the process matrix of Eq. (5.1) and the blue line is the exponential fitting result of the mean ratio of the REC. Inset shows extrapolations of fits in a longer time range. The shadow indicates the enlarged area in the figure. The blue vertical line indicates the time point when the mean REC ratio decays to $1/e$.

5.3.4 Coherence time without dynamical decoupling pulses

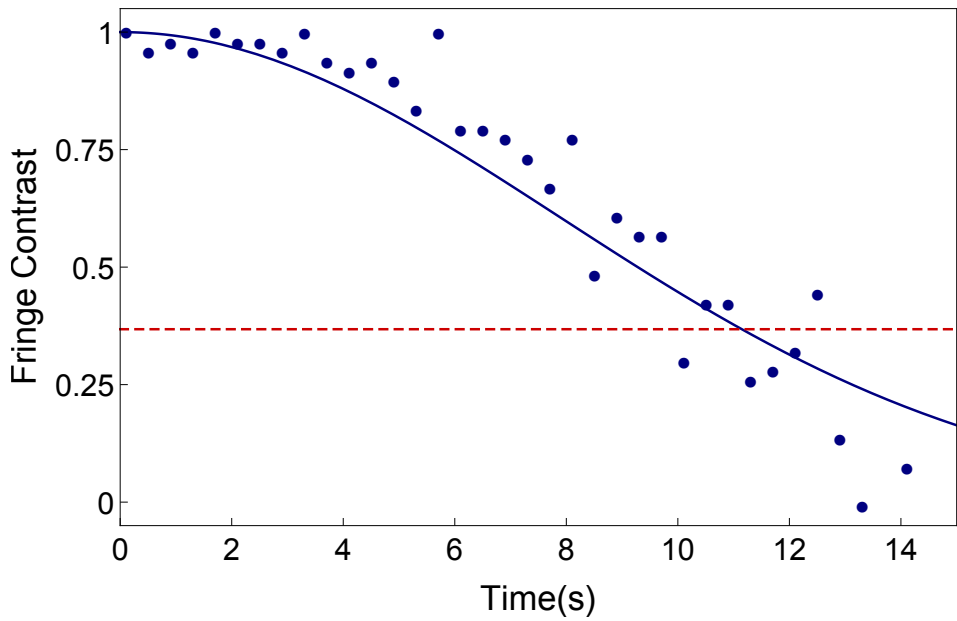
Many experiments of interest can take advantage of dynamical decoupling pulses, but some of them cannot or can only apply a single spin-echo pulse. This makes the enhancement of these special-cases coherence time more attractive for some applications. Fig. 5.9 shows the measurement results for direct Ramsey measurement and one spin-echo pause case.

5.4 Expected limitations of coherence time

The expected limitations of coherence time caused by different decoherence sources are summarized in Fig. 5.10. We note that in the analysis, we do not consider the imperfection of the KDD_{xy} pulses because we find the KDD_{xy} sequence is robust against the typical errors as flip-angle error and frequency-offset errors even at the levels of errors



(a)



(b)

Figure 5.9 Coherence time obtained from Ramsey measurements. (a) without dynamical decoupling pulses and (b) with one spin echo pulse. Blue points are experimental results and each point repeats 100 times. The solid lines are their fitting by the Gaussian decay function. (a) A small detuning between microwave frequency and qubit energy splitting is used here to observe the oscillation signal rather than the fringe contrast signal to wipe out the frequency drift effect. The coherence time is 1.6 ± 0.22 s. (b) The red dashed line indicates the $1/e$ threshold. The coherence time is 11.1 ± 0.38 s.

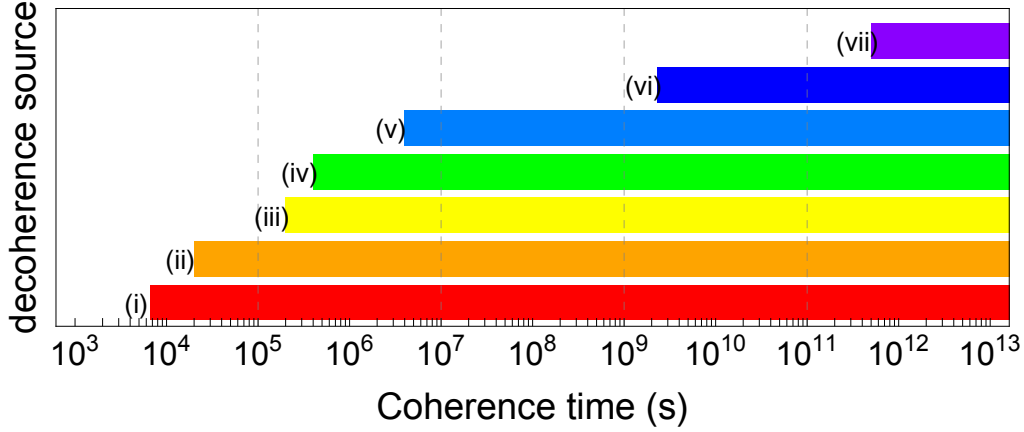


Figure 5.10 Expected limitations of coherence time. The left boundaries of different color-bars indicate expected limitations caused by corresponding decoherence-sources as follows: (i) Phase noise of local oscillator; (ii) Magnetic-field fluctuation; (iii) Ion hopping; (iv) Scattering of $^{138}\text{Ba}^+$ lasers; (v) Leakage of the microwave; (vi) Collision of background gas; (vii) Lifetime of hyperfine ground-state. Currently, the coherence time is mainly limited by the phase noise of the local oscillator and the ultimate coherence time limited by the lifetime of the hyperfine state is estimates as around 5×10^{11} s.

in our system^[107]. For the flip-angle error of 10^{-2} and the frequency-offset error of 100 Hz, around 2×10^{10} pulses and 3×10^{10} can be applied before the output results decay to $1/e$, respectively, which correspond to 0.8×10^{10} s and 1.2×10^{10} s, respectively for our choice of the gap-time, 0.4 s.

(i) Phase noise of local oscillator: the new frequency reference for local oscillator has an order-of-magnitude smaller Allan variance $\sigma(\tau_0)^2$ at $\tau_0 = 1$ s than that of previous one in Ref.^[37], which indicates an order-of-magnitude smaller phase-noises spectrum density $S_{\text{LO}}(\omega)$, assuming the shape of $S_{\text{LO}}(\omega)$ is the same for both references. It is because of the relation between Allan variance $\sigma(\tau_0)^2$ and phase-noise spectrum-density $S_{\text{LO}}(\omega)$ is $\sigma(\tau_0)^2 = \frac{1}{\pi} \int_0^\infty S_{\text{LO}}(\omega) \sin^4(\frac{\tau_0}{2}\omega) d\omega$ ^[114]. With the order-of-magnitude smaller $S_{\text{LO}}(\omega)$, the Ramsey fringe contrast^[101] $W(T) = e^{-\frac{2}{\pi} \int_0^\infty S_{\text{LO}}(\omega) |\tilde{y}(\omega, T)|^2 d\omega}$ will also takes an order-of-magnitude longer time to reach $1/e$. Therefore, the current an order of magnitude enhancement of coherence time is mainly limited by the phase noise of local oscillator.

(ii) Magnetic-field fluctuation: magnetic-field noise is suppressed by shielding and permanent magnet. The comparison of magnetic-field fluctuation before and after the suppression is shown in Fig. 5.3. The coherence time of the Zeeman state is improved by around 30 times improvement after magnetic-field noise suppression similar to that in Ref.^[100]. Therefore, we expect the limitation of the coherence time of the clock-state qubit due to the magnetic-field fluctuation is increased by 30 times, which is around 2×10^4 s.

(iii) Ion hopping: hopping of the ions between two positions that have the qubit-frequency difference of 0.22 Hz (60 μG difference) occurs about every 10 min. The estimated infidelity of a superposition state due to the alternating frequency changes from the ion-hopping is around 2.7×10^{-3} per hopping. Assuming the infidelity increases exponentially with the number of hopping, the limitation of coherence time due to the ion-hopping is expected to be around 2×10^5 s ($= 10 \text{ min}/(2.7 \times 10^{-3})$). We estimate the infidelity per hopping as follows. Since a small amount of constant frequency-shift almost does not introduce infidelity due to the KDD_{xy} sequences, we ignore the no-hopping period. When hopping occurs, the effect of frequency shift cannot be compensated by the dynamical decoupling pulses, which introduces the infidelity of the state. We assume in one KDD_{xy} unit, hopping occurs at most once with a uniform distribution of time, which is reasonable since the duration of one KDD_{xy} unit (4 s) is much shorter than the period of the hopping (10 min). Finally, we average out the infidelities at different occurring times of hopping.

(iv) Scattering of $^{138}\text{Ba}^+$ lasers: we estimate the spontaneous emission rate of the $^{171}\text{Yb}^+$ ion assuming the cooling laser beams (493 nm and 650 nm) of the $^{138}\text{Ba}^+$ ion are entirely applied to the $^{171}\text{Yb}^+$ ion. The spontaneous emission rate of the dipole transition of the $^{171}\text{Yb}^+$ ion is written as^[37,115-117]:

$$\Gamma_{\text{spon}} = \frac{\gamma g^2}{6} \left(\frac{1}{\Delta_{\text{D1}}^2} + \frac{2}{(\Delta_{\text{FS}} - \Delta_{\text{D1}})^2} \right) \quad (5.2)$$

where $\gamma \approx 2\pi \times 20$ MHz is the spontaneous emission rate from the ^2P states, $g = \frac{\gamma}{2} \sqrt{I/(2I_{\text{sat}})}$, $\Delta_{\text{HF}} = 2\pi \times 12.6$ GHz, $\Delta_{\text{FS}} = 2\pi \times 100$ THz. For 493 nm laser, power $P = 35$ μW , beam waist $\omega = 31.4$ μm , $I_{493} = 21.8I_{\text{sat}}$, $\Delta_{\text{D1}} = 2\pi \times 203.8$ THz, then we get a scattering rate of 1.09×10^{-6} Hz. For the 650 nm laser, power $P = 66$ μW , beam waist $\omega = 22.9$ μm , $I_{650} = 75.5I_{\text{sat}}$, $\Delta_{\text{D1}} = 2\pi \times 349.9$ THz, scattering rate 1.29×10^{-6} Hz. Therefore, both of 493 nm and 650 nm laser beams provide the limitation of the coherence time around 4×10^5 s.

(v) Leakage of microwave: after improving the frequency stability of the local oscillator and suppressing magnetic-field fluctuations, the coherence time was improved to only twice, 1200 s, which was limited by the microwave leakage. We suppress the leakage by adding the microwave switch with 70 dB isolation at the final stage before the horn. We observe the enhancement of coherence time to 5400 s, which now is mainly limited by the frequency stability of the local oscillator as discussed in section (i). We estimate that the 70 dB isolation suppresses the carrier Rabi-frequency by microwave leakage around 3000

times, which improves the coherence-time limitation to around 4×10^6 ($\approx 1200 \text{ s} \times 3000$).

(vi) Collision of background gas: background-gas collisions cause decoherence by collision frequency-shift. The model in Ref.^[118] estimates that $^{27}\text{Al}^+$ optical transition clock has a frequency shift of order 10^{-16} after 0.15 s probe from the background gas collision of H_2 in the pressure of 38 nPa at room-temperature. The model estimates that a microwave transition has a larger shift as the level of 10^{-14} with 4 s probe, due to no suppression introduced by the Debye-Waller factor. This shift will be an upper bound of our collision frequency-shift because the model does not include the suppression by the sympathetic cooling. We numerically simulate the collision frequency-shift with KDD_{xy} sequences. The infidelity of a superposition state is estimated by around 1.7×10^{-9} for each KDD_{xy} unit, which leads the coherence-time limitation to $4 \text{ s} \times 1/(1.7 \times 10^{-9}) \sim 2 \times 10^9 \text{ s}$, where we assume the infidelity increase exponentially with the number of KDD_{xy} gate numbers^[119].

(vii) Lifetime of hyperfine state: the spontaneous emission rate of magnetic dipole transitions is written as $\gamma = \frac{\alpha \Delta_{\text{HF}}^3 |M|^2}{3m_e^2 c^4}$, where M is the magnetic dipole matrix element that is expected to be of order \hbar , α is the fine-structure constant, and Δ_{HF} the energy splitting of hyperfine qubit^[120]. For the ground hyperfine level of $^{171}\text{Yb}^+$ ions, we estimate it as $\tau_{\text{HF}} = \frac{1}{\gamma} \sim 5 \times 10^{11} \text{ s}$, where we assume $M \sim \hbar$.

5.5 Software-based auto-relock system for laser frequency lock

Measurement of the coherence time needs a long data-taking process. It is necessary to improve the automation of our setup. We have three lasers that need to be locked to the saturated absorption spectrum. Each lock stays locked for about one day after it is locked. The experiment can continue only when all the locks are working properly, which means that the experiment can only last less than half a day after each refresh. So the laser lock jump is the major source of instability in our lab and it is necessary to develop an auto-relock system.

The general method to realize this auto-relocking is to first monitor the lock's error signal with a fast data acquisition card (DAC). Then unlock the PID server once the lock jump occurs. Then adjust the laser wavelength and relock the system. But there are several serious problems with this protocol. Firstly, the error signal peak is pretty narrow and the feedback bandwidth is roughly 10 MHz. Then the DAC needs to be faster than 10 MHz to notice the jump event. The large amount of data collected will complicate the

data processing. Secondly, the error signal of saturated absorption spectrum always has more than one lock point and cannot be distinguished from the error signal. Thirdly, if the WLM signal is used during the relocking process, the wavelength drift of WLM is also a problem since the width of the error signal is small relative to the WLM drift. And the auto-calibration of WLM also doesn't help, since all the lasers used for WLM calibration have to be first locked to the saturated absorption spectrum.

To solve these problems, we have developed some techniques. Firstly, to avoid the use of DAC, we only use the WLM signal throughout the process, which only has one lock point. Secondly, to solve the WLM drift problem, we developed a “self-reference” method, which is based on the fact that the drift of WLM is always slow drift rather than fast fluctuation. Here, a shift register is used to keep recording the locked wavelength in the WLM of 5 mins ago. Since the WLM drift in 5 mins is negligible compare with the width of the error signal, then this record is close enough to the real lock point and can be used as the lock reference once lock jump happens. The feedback process doesn't need to be very fast and can be done based on Labview software.

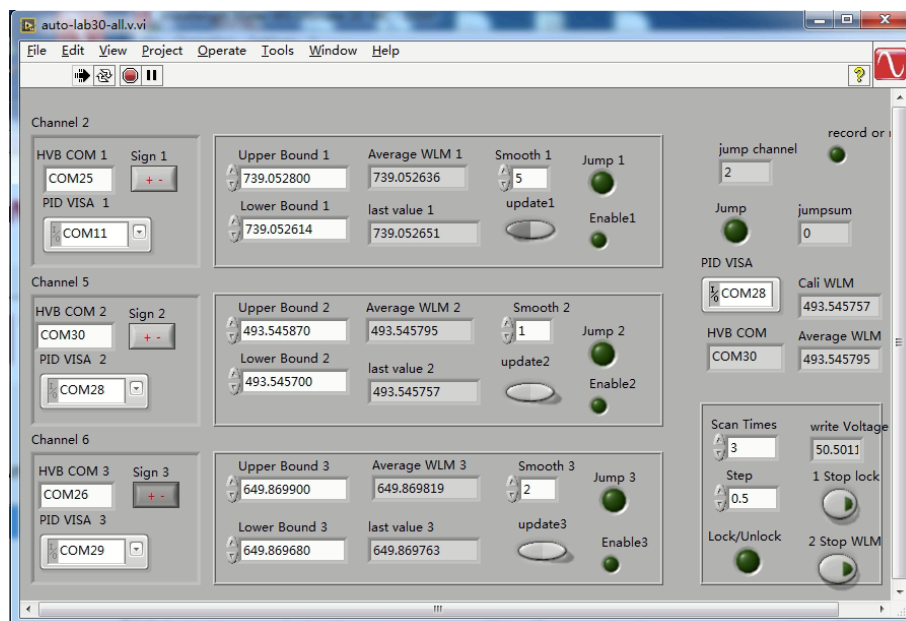


Figure 5.11 Labview auto-relock program for laser frequency lock.

Fig. 5.11 shows our Labview-based auto-relock system for frequency locks. There are three channels of controller for three lasers: 739 nm laser, 493 nm laser, and 650 nm laser. It is also easy to increase the number of channels to more than three. The upper bound and lower bound are used to judge whether the lock jumps. The “last value” is the locked wavelength of 5 mins ago. The “Average WLM” shows the real-time wavelength

averaged by “Smooth” times. And the program can record all the lock jump events, which can be used for removing abnormal experiment data later. The program can also send an alarm email to the mobile phone if any laser lock jumps too frequently.

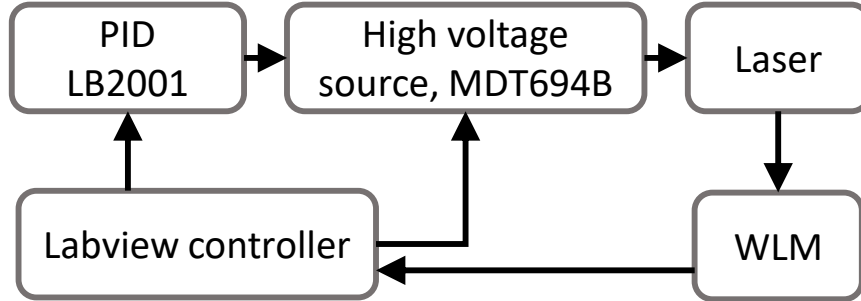


Figure 5.12 Auto-relock system hardware connection.

Fig. 5.12 shows the hardware connection of the auto-relock system. The LB2001 is a PID server, which can be controlled remotely. MDT694B is a high voltage source. The output can be controlled by the input BNC port and serial port.

A simplified version of the logic diagram for our auto-relock system is shown in Fig. 5.13. With the help of this auto-relock system, our experiment setup can continuously take data for more than one week without manually re-locking the laser.

5.6 Discussion

In conclusion, we report a trapped-ion based single qubit quantum memory with over one hour coherence time, an order-of-magnitude enhancement compared to the state-of-the-art record^[37]. The quantum memory with the long-coherence time will accelerate the development of scalable quantum computation^[4,121-122], long-distance quantum communication^[9,123], high-precision quantum metrology^[12-13] and quantum money^[26-27], in particular, in the near-term noise-intermediate-scale quantum regime where there will be no quantum error correction. Our research can be also extended to realize a general-purpose quantum-memory that contains multiple qubits capable of individual storage and retrieval of quantum information at any required time with further enhancement of coherence time and increase of the number of individually controllable qubits.

Further enhancement of the coherence time to day level ($\approx 10^5$ s) may be achievable by improving the stability of the classical oscillator and magnetic-field fluctuation as shown in Fig. 5.10. To reach the ultimate coherence time limited by the lifetime of the excited hyperfine state that is expected to be thousands of years to our estimation, we

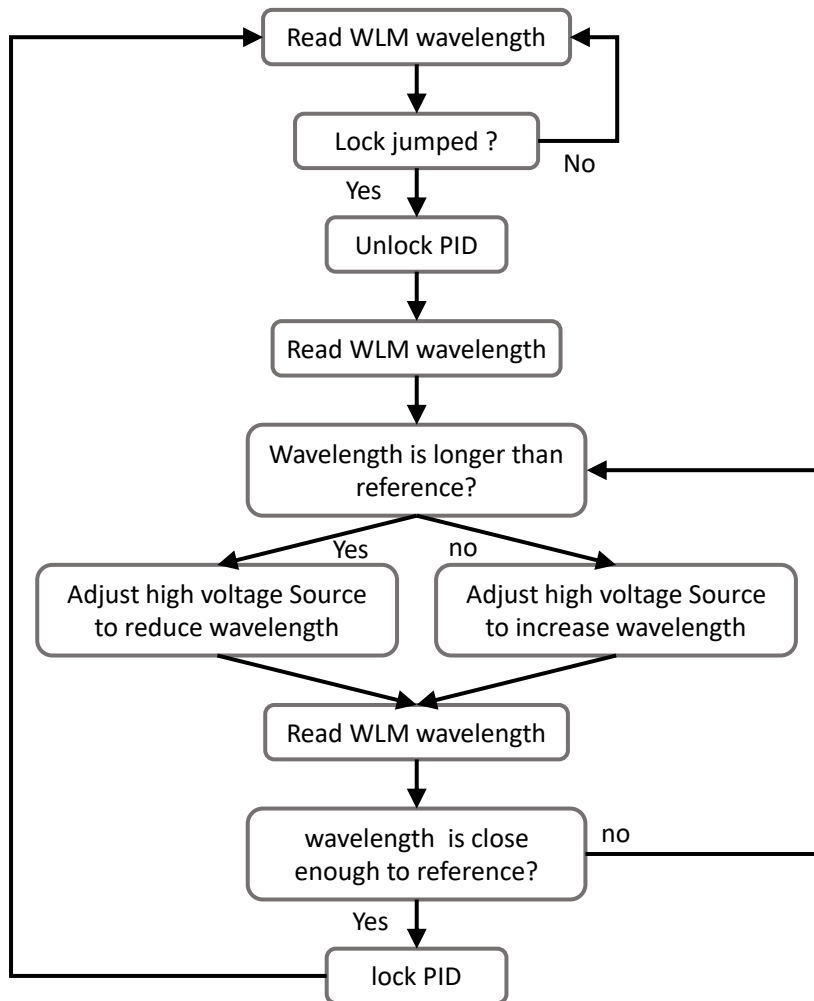


Figure 5.13 Auto-relock system logic block diagram.

need to suppress the hopping of ions, decoherence from scattering of $^{138}\text{Ba}^+$ lasers, leakage of the microwave, and collision of the background gas. Microwave leakage can be simply addressed by adding switches. The other sources of decoherence are related to the background gas collisions. The collisions cause hopping of ions, which introduces frequency shift from different magnetic-field strengths between two positions and collision frequency-shift due to change of motional distribution and phase of atomic superposition^[118]. The background gas collisions can be significantly suppressed by locating the ion trap system in a cryostat environment^[124], which naturally suppresses the hopping rates and collision-induced shift. No hopping allows us to shed the cooling laser beams only on the $^{138}\text{Ba}^+$ ion, which eliminates the scattering-induced decoherence of the ion-qubit.

Our work can be extended to the general purpose of quantum memory, quantum money for example, that requires a large number of qubits by using a long ion-chain in a trap with an individual addressing system. The necessary technical improvement for such quantum memory is to eliminate the hopping problem because hopping ruins the individual tracking of the quantum memory. The hopping problem in the long-linear chain can be also suppressed by a cryostat ion-trap as discussed above. We also notice that in the long ion-chain, the micromotion induces inefficiency of state-detection^[125]. Individual compensation of the micromotions can be achieved by a sophisticated trap with the capability of local-field control.

CHAPTER 6 ENTANGLEMENT GENERATION BETWEEN $^{171}\text{Yb}^+$ AND $^{138}\text{Ba}^+$ IONS

As discussed in Chapter 2, multi-species trapped ion system can adopt the advantage of both species and realize some important applications, such as ion photon network and quantum error correction. But the first step to achieve most of these advantages is entanglement generation between different species of ions. Here, we demonstrate entanglement between $^{171}\text{Yb}^+$ and $^{138}\text{Ba}^+$ ions with a fidelity up to 98.1%. We first cool the system close to the thermal ground state and then realize the entanglement through Mølmer-Sørensen (M-S) interaction.

6.1 Ion qubits

We perform the entanglement between two different atomic ions, one of $^{171}\text{Yb}^+$ and the other of $^{138}\text{Ba}^+$, trapped in a four-rod Paul trap^[70] as shown in Fig. 6.1. Two hyperfine levels of the $^2S_{1/2}$ manifold of the $^{171}\text{Yb}^+$ ion are used as one of the qubits, denoted as $|0\rangle_{\text{Yb}} \equiv |F=0, m_F=0\rangle$ and $|1\rangle_{\text{Yb}} \equiv |F=1, m_F=0\rangle$. The energy gap between the two states is $f_{\text{Yb}} = 12.64281$ GHz. While the other qubit is represented by the two Zeeman levels of the $^2S_{1/2}$ manifold of the $^{138}\text{Ba}^+$ ion as $|1\rangle_{\text{Ba}} \equiv |m=-1/2\rangle$ and $|0\rangle_{\text{Ba}} \equiv |m=1/2\rangle$. The energy gap is $f_{\text{Ba}} = 16.8$ MHz in an external magnetic field of 6.0 Gauss. The states of both qubits can be measured with fluorescence detection technique. For the $^{171}\text{Yb}^+$ ion, the cyclic transition between $|F=1\rangle$ states in $^2S_{1/2}$ and $|F=0, m_F=0\rangle$ in $^2P_{1/2}$ is excited with a 370 nm laser beam so that only $|1\rangle_{\text{Yb}}$ scatters photons. While for the $^{138}\text{Ba}^+$ ion, we first transfer the population of $|0\rangle_{\text{Ba}}$ to $^2D_{5/2}$ with a 1762 nm laser beam before exciting the 493 nm transition between $^2S_{1/2}$ and $^2P_{1/2}$ levels. A 1064 nm picosecond pulsed laser is used for the coherent quantum operations of the two qubits. Two beams from its 532 nm frequency-doubled output are used to generate a stimulated Raman process to control the $^{138}\text{Ba}^+$ ion, and another two beams from its 355 nm frequency-tripled output are used for the $^{171}\text{Yb}^+$ ion^[126]. The schematic diagram of the arrangement of both Raman laser beams is shown in Fig. 6.1(c).

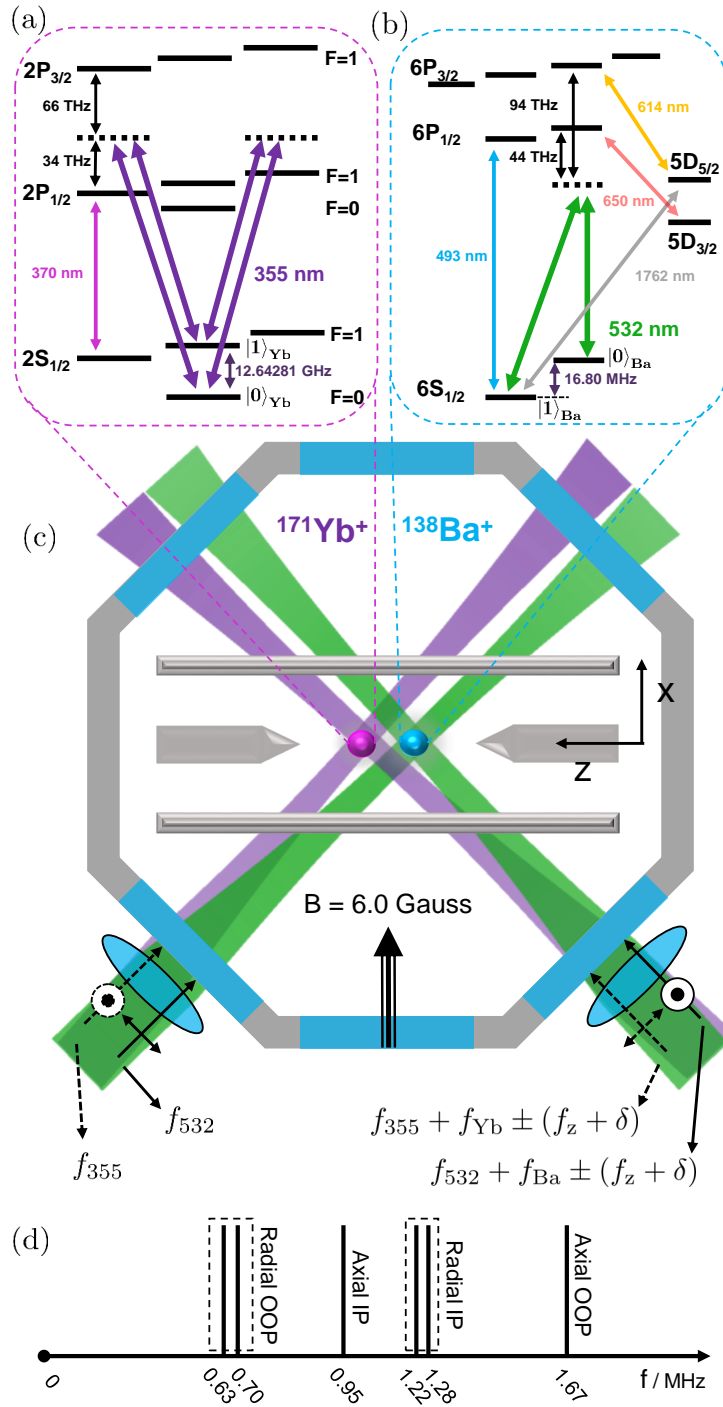


Figure 6.1 Experimental setup. (a) and (b) are the energy level diagrams of $^{171}\text{Yb}^+$ and $^{138}\text{Ba}^+$ ion, respectively. Only relevant Raman transitions are shown here. (c), Ion trap in the octagon chamber and schematic diagram for Raman beams. Solid and dashed arrows indicate the directions and the polarizations of 532 nm and 355 nm laser beams, respectively. In the figure, $f_{\text{Yb},0}$ and $f_{\text{Ba},0}$ are the qubit frequencies of $^{171}\text{Yb}^+$ and $^{138}\text{Ba}^+$, respectively, $f_z = 1.67$ MHz is the frequency of the axial out-of-phase (OOP) mode, and δ is 22.0 kHz. (d), Frequencies of vibrational modes of a single $^{171}\text{Yb}^+$ and a single $^{138}\text{Ba}^+$ ions. Axial OOP mode is used for the Mølmer-Sørensen (M-S) interaction. IP stands for in-phase mode.

6.2 EIT cooling and sideband cooling

We perform three-step cooling before the entanglement operation. First is the Doppler cooling, which only needs one cooling beam. But Doppler cooling has a cooling limit of roughly tens of phonons, which is too high to perform an entanglement gate. Then we need other cooling methods to cool the system further. In our system, we also use electromagnetically-induced-transparency (EIT) cooling^[127] and Raman sideband cooling^[128] to cool the system down.

As shown in Fig. 4.4, we apply the EIT cooling to the $^{138}\text{Ba}^+$ ion by two 493 nm laser beams, then a Fano profile is realized by the EIT effect. We put the laser frequency to the dip and then the red sideband has a higher transition possibility than the blue sideband transition. Then the phonon number can be reduced efficiently during the 1500 μs EIT cooling process. The Fano profile is shown in Fig. 6.2.

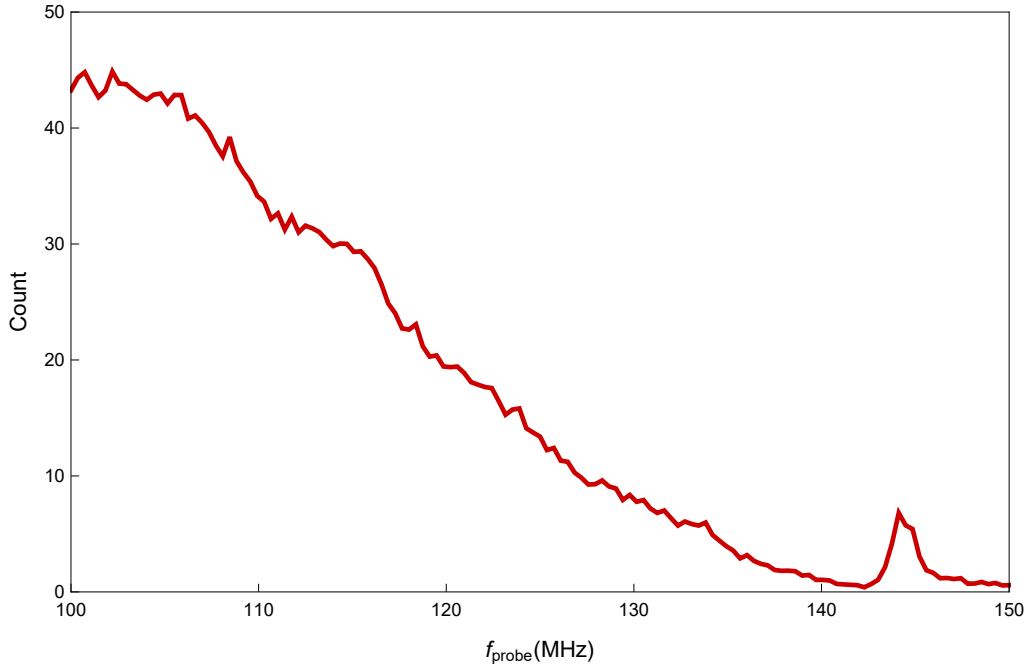


Figure 6.2 Fano profile of EIT cooling. The horizontal axis is the RF frequency of the probe laser double pass AOM. The left side is the red side and the main peak is close to the resonant frequency. The small peak around 145 MHz is the Fano profile caused by the EIT effect. The vertical axis is the count of $^{138}\text{Ba}^+$ ion.

To improve the performance of EIT cooling, we want higher peak count and lower dip count in the Fano profile. They determine the cooling speed and final cooling limitation. Fig. 6.3 shows the effect of probe beam power to the Fano profile and Fig. 6.4 shows the effect of coupling beam frequency to the Fano profile.

To further reduce the phonon number, we apply 50 cycles of resolved Raman sideband

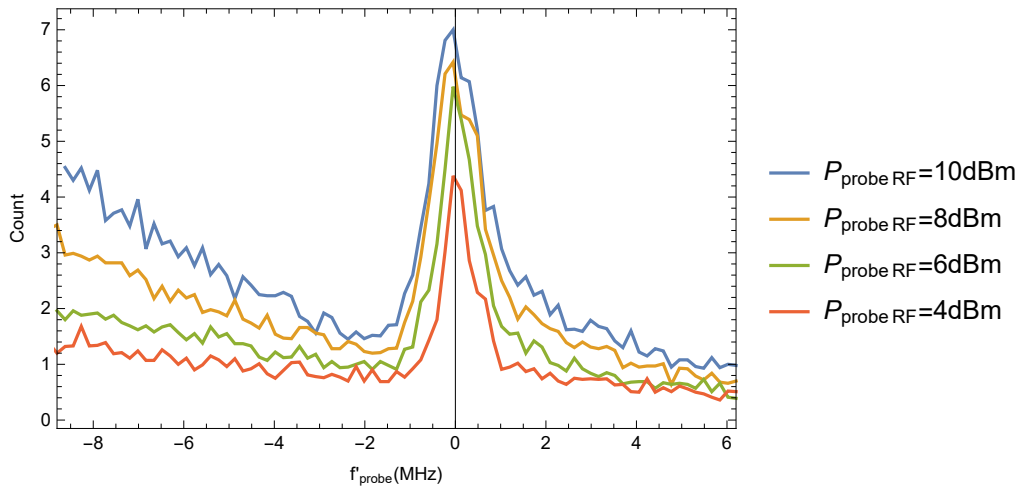


Figure 6.3 Fano profile for different probing beam power. Increasing probe beam power can improve peak count but also background count.

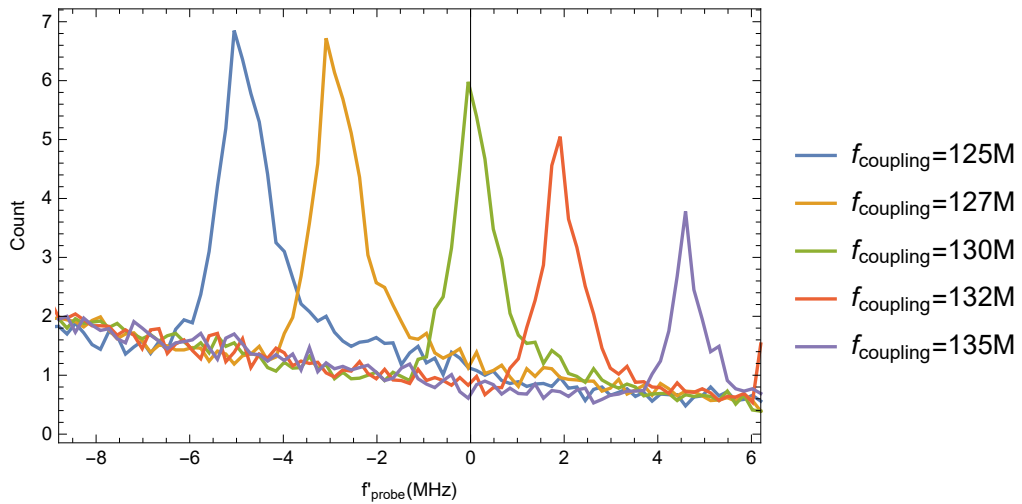


Figure 6.4 Fano profile for different coupling beam frequency. Increasing coupling beam frequency can reduce background count but also reduce peak count.

cooling after the EIT cooling and get an average phonon number lower than 0.04. Since the charging and thermal effect of 355 nm Raman laser are stronger than 532 nm laser, we only use 532 nm laser for the sideband cooling. Two axial modes are cooled alternatively through the $^{138}\text{Ba}^+$ ion. As shown in Fig. 6.5, during the sideband cooling process, blue sideband π -pulse and optical pumping pulse are applied alternatively, which moves the phonon state from higher Fock state $|n_F\rangle$ to lower one $|(n-1)_F\rangle$ step by step. Eventually, in the ideal case, the phonon state will end up with $|0_F\rangle$ as long as the phonon number after EIT cooling is less than 50. But Raman operation imperfection and trap heating always exist and make the cooling not perfect.

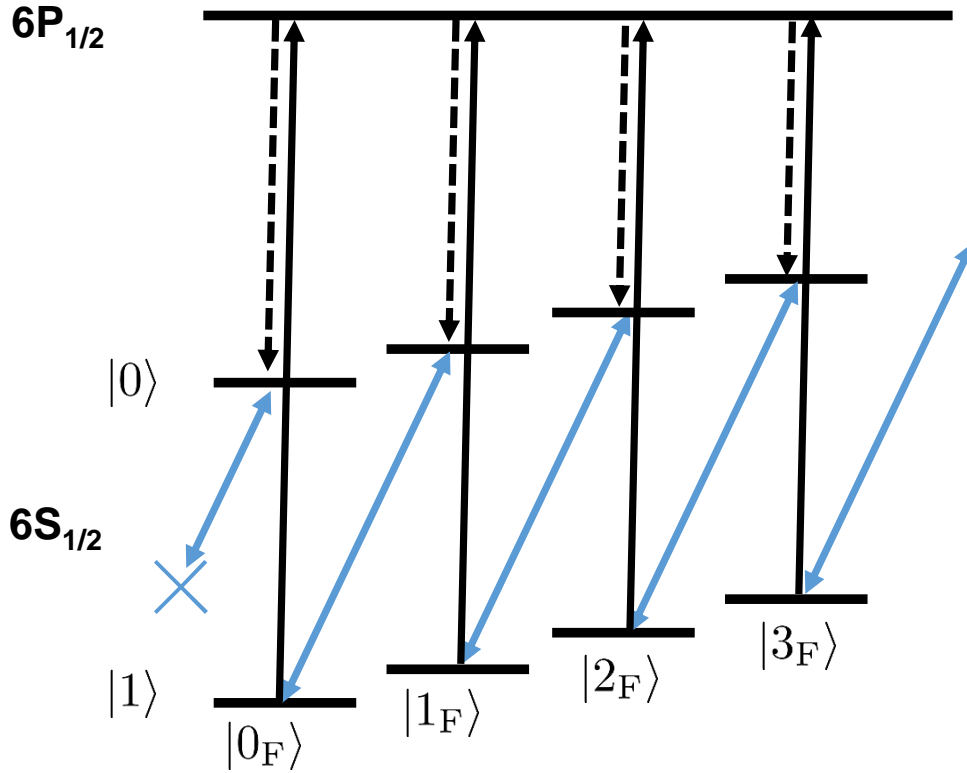


Figure 6.5 Sideband cooling scheme. The blue lines are the blue sideband Raman π pulses and the black solid lines are the optical pumping pulses. The black dashed lines are the spontaneous emission from $6P_{1/2}$.

6.3 Motional mode

6.3.1 Axial mode

For the $^{171}\text{Yb}^+$ - $^{138}\text{Ba}^+$ two ion crystal in our four-rod trap, there are six motional modes in total and the performances of axial modes and radio modes are different. We

first consider the axial mode, and the calculation follows Ref. [74,92,129-130].

We use m_1 and m_2 to donate the mass of $^{171}\text{Yb}^+$ and $^{138}\text{Ba}^+$ ion, respectively. If only consider the axial direction, the kinetic energy is:

$$T_z = \frac{m_1 \dot{z}_1^2}{2} + \frac{m_2 \dot{z}_2^2}{2}. \quad (6.1)$$

The potential energy is:

$$U_z = \frac{k_z z_1^2}{2} + \frac{k_z z_2^2}{2} + \frac{Q}{|z_2 - z_1|}, \quad (6.2)$$

where $Q = \frac{e^2}{4\pi\epsilon_0}$ and z_1 and z_2 are position of $^{171}\text{Yb}^+$ and $^{138}\text{Ba}^+$ ion in axial direction, respectively. $k_z = m_1 \omega_{1z}^2 = m_2 \omega_{2z}^2$ is the spring constant.

The equilibrium position $z_1(0)$ and $z_2(0)$ of two ions should satisfy that:

$$\begin{aligned} \left. \frac{\partial U_z}{\partial z_1} \right|_{(z_1=z_1(0), z_2=z_2(0))} &= 0 \\ \left. \frac{\partial U_z}{\partial z_2} \right|_{(z_1=z_1(0), z_2=z_2(0))} &= 0. \end{aligned} \quad (6.3)$$

Then we have:

$$\begin{aligned} z_1(0)k_z - \frac{Q}{(z_1(0)-z_2(0))^2} &= 0 \\ z_2(0)k_z + \frac{Q}{(z_1(0)-z_2(0))^2} &= 0. \end{aligned} \quad (6.4)$$

Then

$$\begin{aligned} z_1(0) &= \sqrt[3]{\frac{Q}{4k_z}} \\ z_2(0) &= -\sqrt[3]{\frac{Q}{4k_z}}. \end{aligned} \quad (6.5)$$

Then U can have a Taylor expansion at the equilibrium position. The constant term and higher than second order term can be ignored. Since the first order term equals zero so we can only consider the second order term and obtain:

$$U_z \approx \frac{1}{2} \left. \frac{\partial^2 U}{\partial z_1^2} \right|_0 z_1^2 + \frac{1}{2} \left. \frac{\partial^2 U}{\partial z_2^2} \right|_0 z_2^2 + \left. \frac{\partial^2 U}{\partial z_1 \partial z_2} \right|_0 z_1 \cdot z_2. \quad (6.6)$$

The Lagrangian of the system is $L_z = T_z - V_z$. The equation of the motion is:

$$-\frac{\partial}{\partial t} \frac{\partial T_z}{\partial \dot{z}_i} = \frac{\partial U_z}{\partial z_i}. \quad (6.7)$$

Then we have:

$$\begin{aligned} \left. \frac{\partial^2 U}{\partial z_1^2} \right|_0 z_1 + \left. \frac{\partial^2 U}{\partial z_1 \partial z_2} \right|_0 z_2 + m_1 \ddot{z}_1 &= 0 \\ \left. \frac{\partial^2 U}{\partial z_1 \partial z_2} \right|_0 z_1 + \left. \frac{\partial^2 U}{\partial z_2^2} \right|_0 z_2 + m_2 \ddot{z}_2 &= 0. \end{aligned} \quad (6.8)$$

If we assume $z_i(t) = z_i e^{i\omega t}$, which means two ions move in the same frequency. Then we get:

$$\frac{k_z}{m_1} \begin{pmatrix} -2 & 1 \\ \alpha & -2\alpha \end{pmatrix} \begin{pmatrix} z_1 \\ z_2 \end{pmatrix} = \omega^2 \begin{pmatrix} z_1 \\ z_2 \end{pmatrix}, \quad (6.9)$$

where $\alpha = m_1/m_2$ is the mass ratio between two ions. Then the mode frequencies are eigenvalues of the left matrix. For the single species ion case, $\alpha = 1$, the two mode frequency are ω_1 and $\sqrt{3}\omega_1$, known as center-of-mass (CM) mode and breathing modes.

For the general case, the frequency of out-of-phase (OOP) mode and in-phase (IP) mode are:

$$\omega_{\text{OOP}} = \sqrt{\frac{(\sqrt{\alpha^2 - \alpha + 1} + \alpha + 1) k_z}{\alpha}} \quad (6.10)$$

$$\omega_{\text{IP}} = \sqrt{\frac{(-\sqrt{\alpha^2 - \alpha + 1} + \alpha + 1) k_z}{\alpha}},$$

and corresponding eigenvectors are:

$$X_{\text{OOP}} = \left\{ \begin{array}{l} \frac{\sqrt{\alpha^2 - \alpha + 1} - \alpha + 1}{\alpha \sqrt{\frac{(\sqrt{\alpha^2 - \alpha + 1} - \alpha + 1)^2}{\alpha^2} + 1}}, \frac{1}{\sqrt{\frac{(\sqrt{\alpha^2 - \alpha + 1} - \alpha + 1)^2}{\alpha^2} + 1}} \end{array} \right\} \quad (6.11)$$

$$X_{\text{IP}} = \left\{ \begin{array}{l} \frac{-\sqrt{\alpha^2 - \alpha + 1} - \alpha + 1}{\alpha \sqrt{\frac{(-\sqrt{\alpha^2 - \alpha + 1} - \alpha + 1)^2}{\alpha^2} + 1}}, \frac{1}{\sqrt{\frac{(-\sqrt{\alpha^2 - \alpha + 1} - \alpha + 1)^2}{\alpha^2} + 1}} \end{array} \right\}.$$

Two ions IP mode and OOP mode amplitudes for different mass ratio α are shown in Fig. 6.6 and Fig. 6.7.

6.3.2 Radial mode

Since x direction and y direction are symmetric, we only consider x direction for the Radial mode. The kinetic energy in x direction is:

$$T_x = \frac{m_1 \dot{x}_1^2}{2} + \frac{m_2 \dot{x}_2^2}{2}. \quad (6.12)$$

The potential energy is:

$$U_x = \frac{k_x x_1^2}{2} + \frac{k_x x_2^2}{2} + \frac{Q}{|\mathbf{r}_2 - \mathbf{r}_1|}, \quad (6.13)$$

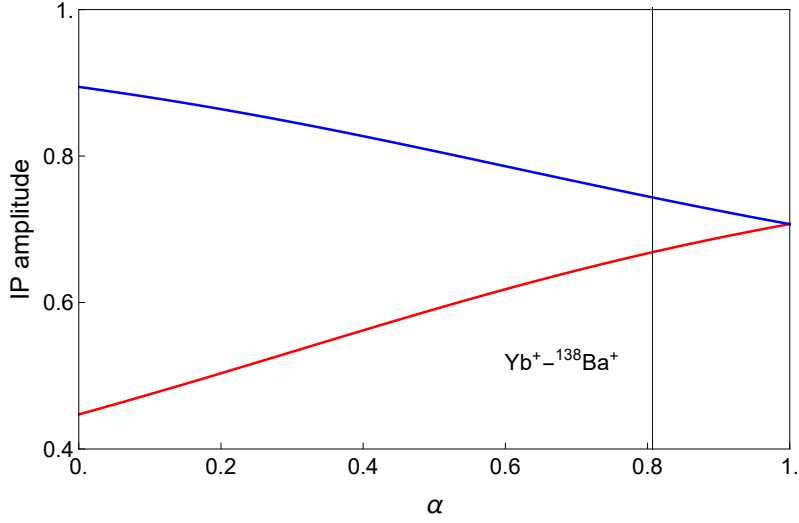


Figure 6.6 Two ions axial IP mode amplitudes for different mass ratio. For our case, $\alpha = 138/171 = 0.807$. $^{171}\text{Yb}^+ - ^{138}\text{Ba}^+$ ions axial IP mode amplitudes are (0.669, 0.744).

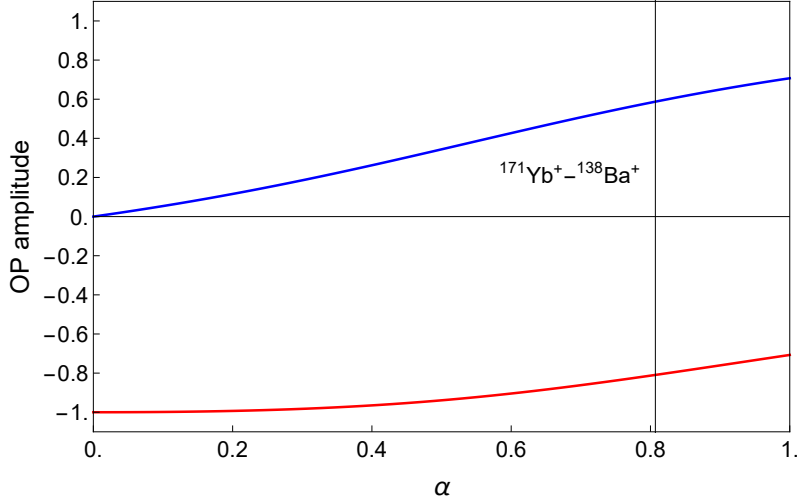


Figure 6.7 Two ions axial OOP mode amplitudes for different mass ratio. For our case, $\alpha = 0.807$. $^{171}\text{Yb}^+ - ^{138}\text{Ba}^+$ ions axial OOP mode amplitudes are (-0.809, 0.587).

where $k_x = m_1 \omega_{1x}^2$ is the spring constant in x direction. The equilibrium position of x direction is $x_1 = x_2 = 0$ due to the geometric symmetry. We can obtain the $\frac{1}{|r_2 - r_1|}$ by Taylor expansion at the equilibrium position:

$$\begin{aligned}
 \frac{1}{|r_2 - r_1|} &= \frac{1}{\sqrt{(x_1 - x_2)^2 + (z_1 - z_2)^2}} \\
 &\approx \frac{1}{\Delta z} \left(1 - \frac{(x_1 - x_2)^2}{2\Delta z^2} \right) \\
 &= \frac{1}{\Delta z} - \frac{1}{2\Delta z^3} (x_1^2 + x_2^2 - 2x_1x_2),
 \end{aligned} \tag{6.14}$$

where $\Delta z = z_1 - z_2 = \sqrt[3]{\frac{Q}{k_z}}$. Then same as axial case, we can get the Lagrange equation:

$$\begin{pmatrix} \frac{k_z}{2} - k_x & -\frac{k_z}{2} \\ -\frac{k_z}{2\alpha} & -\frac{k_x - \frac{k_z}{2}}{\alpha} \end{pmatrix} \begin{pmatrix} x_1 \\ x_2 \end{pmatrix} = \omega^2 \begin{pmatrix} x_1 \\ x_2 \end{pmatrix}, \quad (6.15)$$

then:

$$k_z \begin{pmatrix} \frac{1}{2} - \left(\frac{\omega_{1x}}{\omega_{1z}}\right)^2 & -\frac{1}{2} \\ -\frac{1}{2\alpha} & -\frac{\left(\frac{\omega_{1x}}{\omega_{1z}}\right)^2 - \frac{1}{2}}{\alpha} \end{pmatrix} \begin{pmatrix} x_1 \\ x_2 \end{pmatrix} = \omega^2 \begin{pmatrix} x_1 \\ x_2 \end{pmatrix}. \quad (6.16)$$

If $\alpha = 1$, then two eigenvalues are $(\omega_{1x}, \sqrt{\omega_{1x}^2 - \omega_{1z}^2})$, where the radial zigzag mode frequency is a function of axial and radial CM mode frequency.

For the general case, we have:

$X_{\text{OOP}} =$

$$\left\{ \frac{1}{2} \left(\sqrt{4\alpha^2\beta^4 - 4\alpha^2\beta^2 + \alpha^2 - 8\alpha\beta^4 + 8\alpha\beta^2 + 2\alpha + 4\beta^4 - 4\beta^2 + 1} + 2\alpha\beta^2 - \alpha - 2\beta^2 + 1 \right), 1 \right\}$$

$X_{\text{IP}} =$

$$\left\{ \frac{1}{2} \left(-\sqrt{4\alpha^2\beta^4 - 4\alpha^2\beta^2 + \alpha^2 - 8\alpha\beta^4 + 8\alpha\beta^2 + 2\alpha + 4\beta^4 - 4\beta^2 + 1} + 2\alpha\beta^2 - \alpha - 2\beta^2 + 1 \right), 1 \right\}, \quad (6.17)$$

where $\beta = \omega_{1x}/\omega_{1z}$ is the mode frequency ratio between radial and axial direction. If we choose $\beta = 2$, then two radial IP mode and OOP mode amplitudes for different mass ratio α are shown in Fig. 6.8 and Fig. 6.9.

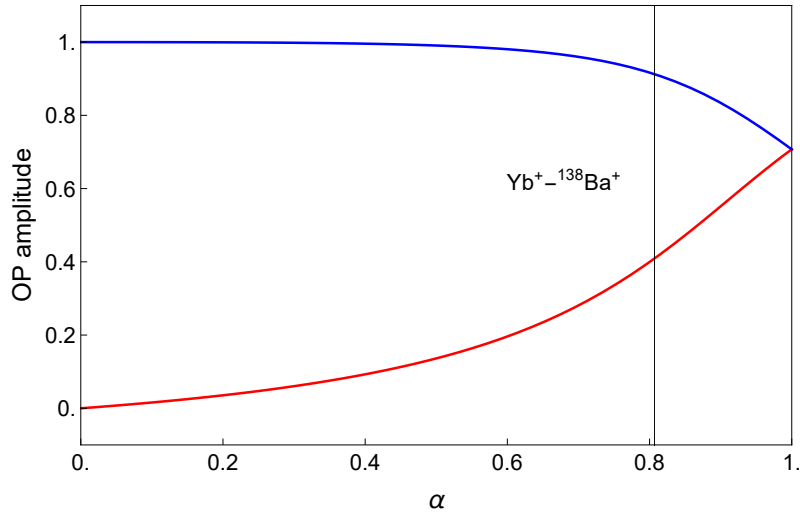


Figure 6.8 Two ions radial IP mode amplitudes for different mass ratio. For our case, $\alpha = 138/171 = 0.807$, $^{171}\text{Yb}^+ - ^{138}\text{Ba}^+$ ions radial IP mode amplitudes are (0.409, 0.912).

The mode amplitudes in the radial direction have a bigger mismatch between two

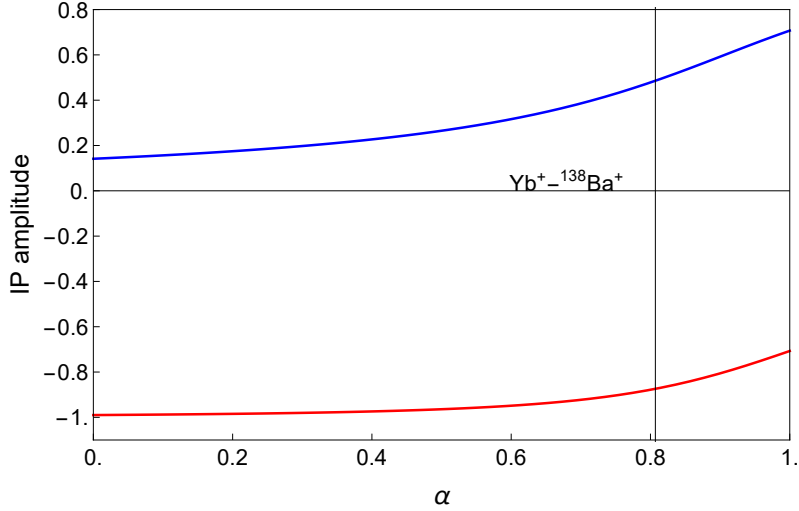


Figure 6.9 Two ions radial OOP mode amplitudes for different mass ratio. For our case, $\alpha = 0.807$, $^{171}\text{Yb}^+ - ^{138}\text{Ba}^+$ ions radial OOP mode amplitudes are $(-0.874, 0.486)$.

ions than the axial ones for $\beta = 2$ case. This situation makes the axial mode easier to get a balance coupling strength for two ions. And the mode amplitudes of OOP mode have different directions for two ions, which makes OOP mode insensitive to the environment noise. Here, we choose the axial OOP mode for mode-related operations.

6.4 Mølmer-Sørensen (M-S) interaction

In our ion trap system, we use the MS interaction to realize two qubit gate, which is produced by simultaneously applying red and blue sidebands of Raman laser with symmetric detunings of $-\delta$ and δ from the motional mode.

If only one mode is involved, Hamiltonian of Raman beam couples with qubit and motional state is as follows:

$$H = \frac{\hbar\omega_{HF}}{2}\sigma_z + \omega_\nu a^\dagger a + \Omega_R \cos(\Delta\mathbf{k} \cdot \mathbf{r} - \delta_\omega t - \Delta\phi)\sigma_x, \quad (6.18)$$

where $\Delta\phi$, δ_ω and $\Delta\mathbf{k}$ are phase difference, frequency difference and momentum vectors difference between the two Raman beam, ω_{HF} is the energy splitting of qubit. ω_ν is the frequency of motional mode. Ω_R is the coupling strength. Change to a rotating frame, in the interaction picture, we have:

$$H_I = \frac{\hbar\Omega_R}{2}\sigma^+ e^{-i(\Delta t + \Delta\phi)} e^{i\eta(a^\dagger e^{i\nu t} + a e^{-i\nu t})} + \text{h.c.}, \quad (6.19)$$

where $\Delta = \delta_\omega - \omega_{HF}$. $\eta = \Delta K x_0 = \Delta k \sqrt{\frac{\hbar}{2m\omega_m}}$ is the Lamb-Dicke parameter characterizing the coupling strength between laser and motional mode. x_0 is the RMS radius of the ion in the ground state of motional mode. When we operate in the Lamb-Dicke regime:

$\eta\sqrt{2\bar{n}+1} \ll 1$, where \bar{n} is the average phonon number, we can ignore the high order of exponential expansion, then we have:

$$H_I = \frac{\hbar\Omega_R}{2}\sigma^+ e^{-i(\Delta t + \Delta\phi)}(1 + i\eta(a^+ e^{i\nu t} + a e^{-i\nu t})) + \text{h.c.} \quad (6.20)$$

Depending on the value of Δ , we will have three kinds of transitions: carrier($\Delta \approx 0$), red($\Delta \approx -\nu$) and blue($\Delta \approx \nu$) transition:

$$\begin{aligned} H_{\text{carrier}} &= \frac{\hbar\Omega_R}{2}\sigma^+ e^{-i(\Delta t + \Delta\phi)} + \text{h.c.} \\ H_{\text{red}} &= \frac{i\eta\hbar\Omega_R}{2}\sigma^+ a e^{-i\Delta\phi} e^{-i(\Delta+\nu)t} + \text{h.c.} \\ H_{\text{blue}} &= \frac{i\eta\hbar\Omega_R}{2}\sigma^+ a^+ e^{-i\Delta\phi} e^{-i(\Delta-\nu)t} + \text{h.c.} \end{aligned} \quad (6.21)$$

Then we apply red and blue sidebands with detunings of $-\delta$ and δ from the motional mode.

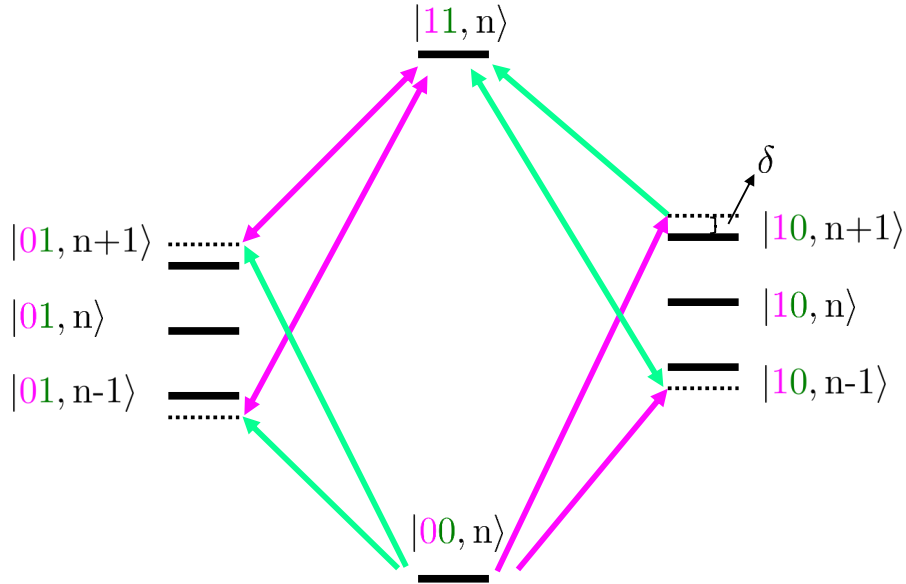


Figure 6.10 MS gate scheme for $^{171}\text{Yb}^+$ - $^{138}\text{Ba}^+$. $|a_1 a_2, n\rangle = |a_1\rangle |a_2\rangle |n\rangle$ is the state of two ion qubit and motional state, $|a_1\rangle$ is state of $^{171}\text{Yb}^+$ qubit, $|a_2\rangle$ is state of $^{138}\text{Ba}^+$ qubit, $|n\rangle$ is motional state. Detuning between laser and motional level is δ , all the sideband Rabi frequency need to be balanced by adjusting the RF signal power of each AOM.

First, we only consider a single ion, then we have:

$$H_{\text{blue+red}} = \frac{i\eta\hbar\Omega_R}{2}(\sigma^+ e^{-i\phi_s} - \sigma_- e^{i\phi_s})(a e^{-i\phi_m} e^{i\delta t} + a^+ e^{i\phi_m} e^{-i\delta t}), \quad (6.22)$$

where $\phi_s = (\phi_r + \phi_b)/2$, $\phi_m = (\phi_r - \phi_b)/2$. In this situation, ion will suffer a different periodic force depending on the qubit state, so called spin dependent force, and this will generate entanglement between qubit and motional state. If there are two ions, ions will

couple to the same motional mode and entangle with each other. If we don't take into account the initial phase of Raman beam, then there will have transition of $|00\rangle \rightarrow |11\rangle$ and $|01\rangle \rightarrow |10\rangle$ with the Rabi frequency $\tilde{\Omega} = \eta^2 \Omega_R^2 / (2\delta)$.

6.4.1 0.75 MHz axial trap frequency case

In our experiment, the MS interaction is mediated by the axial OOP mode^[74]. In the beginning, we use an axial trap frequency of 0.75 MHz and the axial OOP mode is $f_z = 1.32$ MHz. The axial OOP mode is cooled down to $\bar{n}_O \approx 0.04$ and the axial IP mode is cooled down to $\bar{n}_I \approx 0.1$ with Doppler cooling, electromagnetically-induced-transparency (EIT) cooling^[127] and Raman sideband cooling^[128]. The time evolution of the M-S interaction is shown in Fig. 6.11. After the M-S gate, we apply $\pi/2$ rotations to both ions with varying phases and obtain the parity oscillation signal as shown in Fig. 6.11. According to the state population after the M-S gate and the contrast of the parity oscillation, we obtain a fidelity of the entangled state as 0.865. The gate error is mainly due to the imperfection of axial IP mode cooling and the parameter drifts during the long calibration process.

6.4.2 0.95 MHz axial trap frequency case

In order to improve the cooling of axial IP mode, we increase the axial trap frequency to 0.95 MHz. Then the frequency of the axial OOP mode increased to $f_z = 1.67$ MHz. In this case, both axial OOP mode and IP mode can be cool down to $\bar{n} \approx 0.04$. The time evolution of the M-S interaction and parity oscillation signal are shown in Fig. 6.12. We obtain a M-S gate fidelity of 0.939 ± 0.014 . After we correct the error of state preparation and measurement (SPAM), the fidelity increases to $98.0 \pm 0.014\%$. Remain gate errors mainly come from parameter drifts during the calibration process.

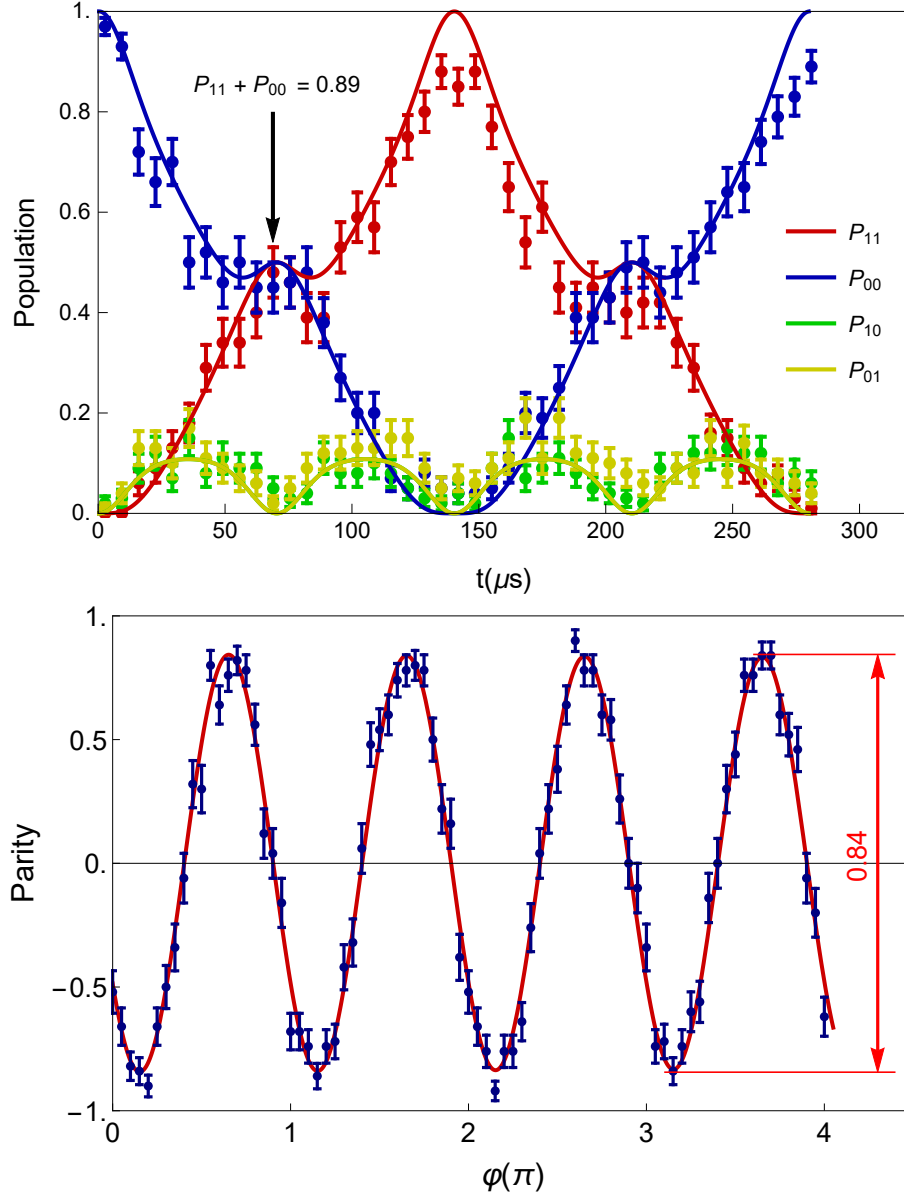


Figure 6.11 Evolution of the M-S interaction and oscillation of parity signal when axial mode is 0.75 MHz. Each data point is the average of 100 repetitions and all the error bars are standard deviation. The first figure is the time evolution of the M-S interaction. P_{ij} is the population of state $|ij\rangle$, where $|i, j\rangle = |i\rangle_{\text{Yb}} |j\rangle_{\text{Ba}}$. $P_{11} + P_{00} = 0.89$ at the end of the gate. The second figure is the parity scan of the entangled state. Parity of a state is defined as $P_{11} + P_{00} - P_{10} - P_{01}$, which is the population difference between the two qubits being in same or opposite states. Parity contrast is 0.84 here.

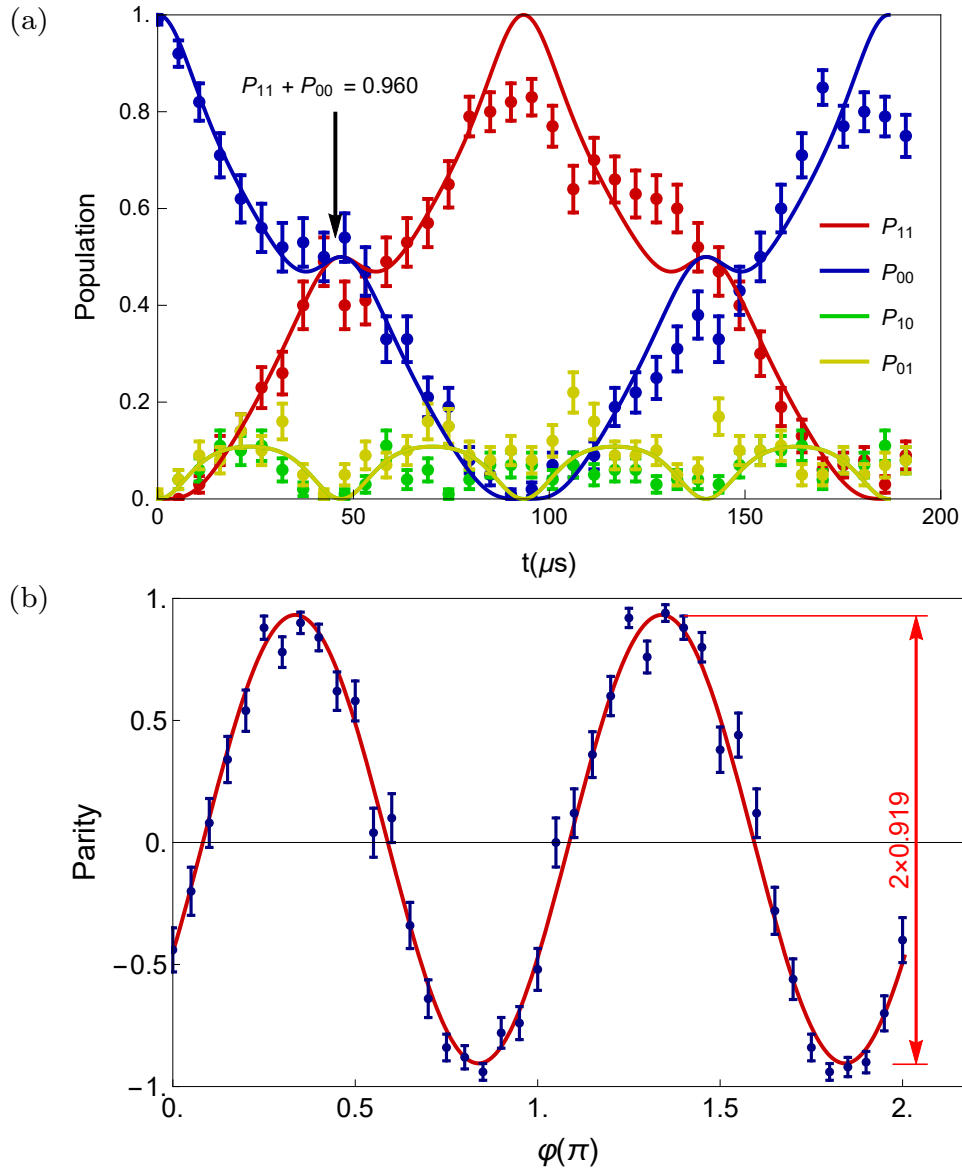


Figure 6.12 Evolution of the M-S interaction and oscillation of parity signal when axial mode is 0.95 MHz. Each data point is the average of 100 repetitions and all the error bars are standard deviation. (a) The time evolution of the M-S interaction. The duration of a single M-S gate is $45.4 \mu\text{s}$ and $P_{11} + P_{00} = 0.960 \pm 0.018$ at the end of the gate. (b) The parity scan of the entangled state. Parity contrast is 0.919 ± 0.021 .

CHAPTER 7 LOOPHOLE-FREE CONTEXTUALITY TEST

7.1 Introduction

In everyday life, we take the fact that the result of an observation is always the same when we repeat the observation, even when we make additional observations, as an indication of a preexisting and lasting property of the observed system. However, in quantum mechanics, that same persistence of results over time cannot be similarly interpreted. The reason is that quantum mechanics allows for contextual correlations between the results of repeatable and mutually nondisturbing measurements^[49-50]. These correlations are impossible to produce with systems in which observations reveal properties that do not depend on what other repeatable and mutually nondisturbing measurements are made. This phenomenon, called contextuality^[48,131], is at the basis of the power of quantum computers to perform tasks that are impossible for classical computers^[132-135].

Contextual correlations between measurements that give the same result when repeated have been observed with ions^[136-139] and, under relaxed assumptions, photons^[140-147], neutrons^[148-149], molecular nuclear spins^[150], superconducting systems^[151], and nuclear spins in diamond^[152]. However, all these experiments leave some loophole open.

Unlike Bell inequality tests, where spacelike separation between measurements sustains the assumption of local realism and loophole-free tests have been achieved^[44-47], in contextuality tests what sustains the assumption of outcome noncontextuality is the existence of measurements which yield the same outcome every time they are repeated on the same system, even when other compatible (i.e., jointly measurable) measurements are performed. These measurements are called “ideal”^[153-158] or “sharp”^[52] and are central to quantum mechanics^[153-154,157-158], where they are called “projective”. Ideal measurements on microscopic systems were for years beyond the reach of experiments^[159]. For a loophole-free proof of contextuality, it is crucial to show that the measurements are repeatable and that every context contains only measurements which are compatible and do not disturb each other. That is, it is crucial that the experiment is free of the compatibility/sharpness loophole^[68]. The name reflects the fact that compatibility and sharpness are related concepts as, by adding noise, the degree of compatibility can be increased at

the expense of reducing the degree of sharpness^[160]. It is also crucial to show that the inefficiency of the detectors cannot hide an outcome non-contextual explanation of the observed correlations. Therefore, the experiment must be free of the detection loophole^[54] that also affects Bell inequality experiments.

Previous contextuality experiments with ions have closed the detection loophole^[136-139], but still suffer from the compatibility loophole^[68]. Loophole-free Bell inequality tests^[44-47] do not suffer the detection loophole, assure measurement compatibility by spatially separating the measurements, but lack the feature of repeatable measurements. Repeatability has been shown in some contextuality experiments with photons^[142,145-147], but these experiments suffer both the compatibility and the detection loopholes.

7.2 Loophole free contextuality test theory

7.2.1 Loophole free

To close simultaneously the detection and the compatibility/sharpness loophole we adopt the following strategy. To close the detection loophole we use fluorescence measurements on trapped ions. To close the compatibility/sharpness loophole we choose a composite system of two different ions^[74,79,130,161-163], one $^{171}\text{Yb}^+$ ion and one $^{138}\text{Ba}^+$ ion. This two-ion-species system, on the one hand, allows for performing sequential measurements on each of the ions, and on the other hand, guarantees that the measurements in each context are compatible as we target a noncontextuality inequality in which there are only two measurements in each context, and each of them can be performed on a different ion. Therefore, compatibility is assured, on the one hand, by the spatial separation between the ions. In addition, compatibility is also enforced by using ions of different species, as measurements on each species use different operation laser wavelengths, fluorescence wavelengths, and detectors. It is this special combination of a “Bell-like”^[140-141] noncontextuality inequality and the use of spatially separated ions of different species which allows us to close all the relevant loopholes simultaneously.

7.2.2 4-cycle quantum contextuality inequality

The noncontextuality targeted by our experiment is the only tight noncontextuality inequality in the so-called “4-cycle contextuality scenario”^[60], which is the simplest scenario producing contextuality^[164-165]. The inequality is formally identical to the Clauser-

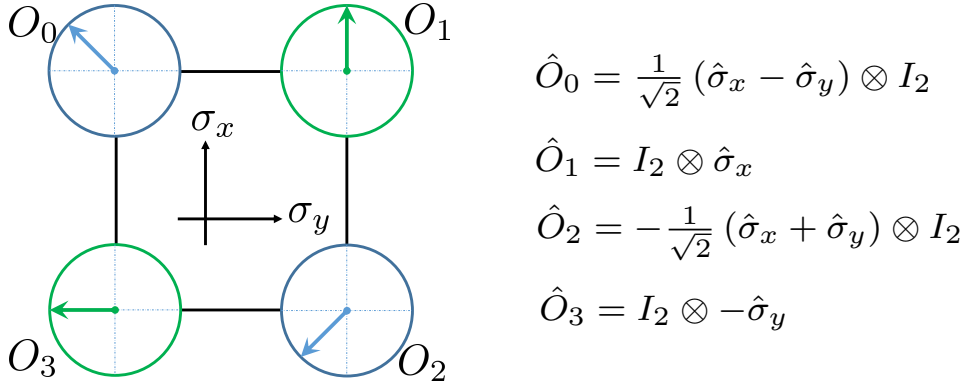


Figure 7.1 The four observables and compatibility relations. The observables \hat{O}_0, \hat{O}_2 are measured on the first qubit, and \hat{O}_1, \hat{O}_3 on the second qubit. The connected observables are compatible (jointly measurable). Here $\hat{\sigma}_x, \hat{\sigma}_y$ are Pauli operators and I_2 is the identity operator.

Table 7.1 Experiment data.

$\{\hat{O}_i, \hat{O}_j\}$	$\langle \hat{O}_i \hat{O}_j \rangle$	$\langle \hat{O}_i^j \rangle$	$\langle \hat{O}_j^i \rangle$
$\{\hat{O}_0, \hat{O}_1\}$	0.6164 ± 0.0074	-0.0008 ± 0.0112	0.1096 ± 0.0071
$\{\hat{O}_1, \hat{O}_2\}$	0.625 ± 0.0105	0.1066 ± 0.0116	0.1236 ± 0.0087
$\{\hat{O}_2, \hat{O}_3\}$	0.6678 ± 0.0083	0.1356 ± 0.0104	0.1078 ± 0.0096
$\{\hat{O}_3, \hat{O}_0\}$	-0.6166 ± 0.0105	0.1114 ± 0.0097	-0.0056 ± 0.0075

Horne-Shimony-Holt Bell inequality^[55], namely,

$$C = \langle \hat{O}_0 \hat{O}_1 \rangle + \langle \hat{O}_1 \hat{O}_2 \rangle + \langle \hat{O}_2 \hat{O}_3 \rangle - \langle \hat{O}_3 \hat{O}_0 \rangle \leq 2, \quad (7.1)$$

but can also be tested using single systems^[140,148] and has to be tested with ideal measurements. Each of the four observables in (7.1) has possible results -1 or 1 , and $\langle \hat{O}_i \hat{O}_j \rangle$ denotes the mean value of the product of the results of \hat{O}_i and \hat{O}_j . The two-qubit observables measured in our experiment and their relations of compatibility are shown in Fig. 7.1. There, each observable is represented by a node in a graph where sets of mutually adjacent nodes represent contexts. Therefore, there are four contexts each with two observables. All tests are performed on a two-qubit system which is prepared into state

$$|\psi\rangle = \frac{|00\rangle + i|11\rangle}{\sqrt{2}}. \quad (7.2)$$

7.3 Experiment result

7.3.1 Contextuality inequality violation

We first prepare the maximum entangled state by the MS gate in Chapter 6, then one of the four contexts is chosen and measured. The observable \hat{O}_0 and \hat{O}_2 are measured on the $^{171}\text{Yb}^+$ ion, and \hat{O}_1 and \hat{O}_3 on the $^{138}\text{Ba}^+$ ion. For each ion, a $\pi/2$ rotation is first performed to map the corresponding observable to the σ_z basis, and then the fluorescence detection is performed. The experiment is repeated 40000 times and the acquired data with standard error are shown in Table.7.1.

With the data we evaluate the left side of inequality (7.1) and

$$C = 2.526 \pm 0.019, \quad (7.3)$$

which violates the classical bound by 28 standard deviation.

In the experimental test, the detection loophole is closed, since we obtain the measurement outcome in each round of the test^[166]. We have the reduction of the violation of the inequality (7.1) due to the single-shot detection-infidelity of around 2% for $^{171}\text{Yb}^+$ ion and 1% for $^{138}\text{Ba}^+$ ion, but we do not miss any measurement results for the whole experimental tests.

7.3.2 Repeatability of measurements

Our experimental test is also free of the compatibility/sharpness loophole, since the measurements in the experiments are projective measurement, which is called as “ideal” or “sharp”. Sharp measurements yield the same outcome when they are repeated and do not disturb compatible measurements^[51,53]. The repeatability of our measurements is checked by repeatedly measuring the same observable in each of the ions, which is defined as:

$$R_i = \frac{\sum_a N(\hat{O}_i = a, \hat{O}_i = a)}{N(\hat{O}_i, \hat{O}_i)}, \quad (7.4)$$

where $a = \pm 1$ are measurement outcomes of the observable, $N(\hat{O}_i, \hat{O}_i)$ is the total number of sequential measurements, and $N(\hat{O}_i = a, \hat{O}_i = a)$ is the number of measurements that have the same outcomes. Ideally, repeatability of all the observables should be 1. In our experiment, the average repeatability of all of them is 98.1% , which is mainly limited by detection infidelity and basis rotation errors. The results of repeatability for four observables are shown in Fig. 7.3. The experiment sequences for repeatability measurement are shown in Fig. 7.2. A single qubit rotation by θ about the $\cos(\phi)\hat{\sigma}_x + \sin(\phi)\hat{\sigma}_y$ axis is

defined as:

$$R(\theta, \phi) = \begin{pmatrix} \cos(\frac{\theta}{2}) & -ie^{-i\phi} \sin(\frac{\theta}{2}) \\ -ie^{i\phi} \sin(\frac{\theta}{2}) & \cos(\frac{\theta}{2}) \end{pmatrix}. \quad (7.5)$$

After the measurement in step 3 in Fig. 7.2, we initialize the ion state to the detected state, we first use optical pumping to pump the qubits state to $|0\rangle$ and then apply single-qubit π rotations to prepare the detected state. These π rotations are different depending on the first measurement result, which is addressed by post-selection.

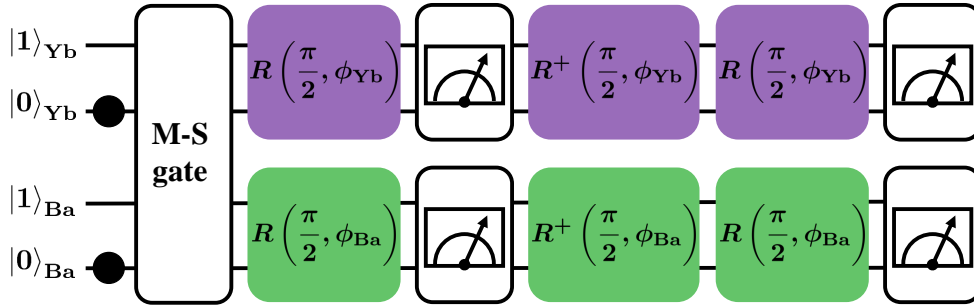


Figure 7.2 Repeatability measurement sequence. Whole sequence include six steps: 1, Pump two qubits to $|0\rangle$ and then prepare the entangled state with M-S gate; 2, Rotate the measurement basis to the observable basis; 3, Projective measurement; 4, Rotate the measurement basis back; 5, Rotate the measurement basis to the observable basis again; 6, Projective measurement again. $R(\frac{\pi}{2}, \phi_{Yb})$ in the pink box and $R(\frac{\pi}{2}, \phi_{Ba})$ in the green box are $\pi/2$ rotations between $\hat{\sigma}_z$ basis and observable basis for $^{171}\text{Yb}^+$ qubit and $^{138}\text{Ba}^+$ qubit, respectively. Only rotations in the pink box will be applied when observable \hat{O}_0 or \hat{O}_2 are measured since they only performed on $^{171}\text{Yb}^+$ ion. $\phi_{Yb} = 5\pi/4$ and $3\pi/4$ for observable \hat{O}_0 and \hat{O}_2 . On the other hand, only rotations in the green box will be applied for observable \hat{O}_1 and \hat{O}_3 , where $\phi_{Ba} = 3\pi/2$ and π , respectively.

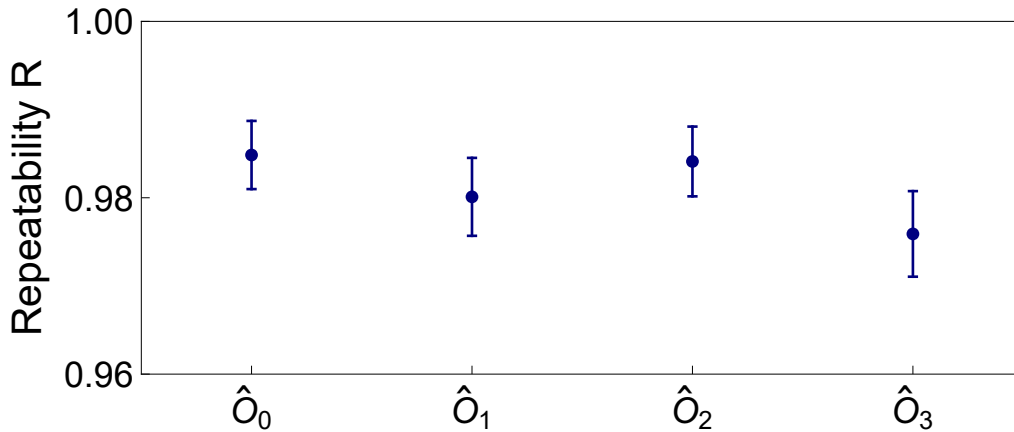


Figure 7.3 Repeatability of four observable measurements. Each observable measurement repeat 1000 times. Error bar is the standard error of the mean (SEM).

7.3.3 Compatibility of measurements

Compatibility is assured by spatial separation and enforced by the adoption of ions of different species as measurements on each species use different operation laser wavelengths, fluorescence wavelengths, and detectors as shown in Fig. 6.1. The 355 nm and 532 nm laser beams are designed to perform coherent operations on $^{171}\text{Yb}^+$ and $^{138}\text{Ba}^+$ ions, respectively. In principle, these laser beams can also influence the other ions. This disturbance is too small to be detected and we theoretically estimate that the amounts are in the order of 10^{-6} .

Moreover, the effect of the possible disturbance between the two ions can be excluded by introducing the quantity of disturbance ε in the inequality (7.6) as^[167]

$$C' = \langle \hat{O}_0 \hat{O}_1 \rangle + \langle \hat{O}_1 \hat{O}_2 \rangle + \langle \hat{O}_2 \hat{O}_3 \rangle - \langle \hat{O}_3 \hat{O}_0 \rangle - \varepsilon \leq 2, \quad (7.6)$$

where $\varepsilon = \sum_{i=0}^3 \left| \langle \hat{O}_i^{i\oplus 1} \rangle - \langle \hat{O}_i^{i\ominus 1} \rangle \right|$, \oplus is right shift ($0 \rightarrow 1 \rightarrow 2 \rightarrow 3 \rightarrow 0$) and \ominus is left shift ($0 \leftarrow 1 \leftarrow 2 \leftarrow 3 \leftarrow 0$). $\langle \hat{O}_i \hat{O}_j \rangle$ is the correlation between observable \hat{O}_i and \hat{O}_j , and $\langle \hat{O}_i^j \rangle$ is the expectation value of observable \hat{O}_i measured jointly with observable \hat{O}_j . As shown in Table 7.1, the ε is 0.023 ± 0.027 , which reduces the value of C by 0.9%. Including the term of ε , $C' = 2.503 \pm 0.033$ also shows the violation by 15 standard deviation.

7.3.4 Crosstalk between qubits and their undesirable Raman beams

The 355 (532) nm Raman laser is designed to drive the transition of $^{171}\text{Yb}^+$ ($^{138}\text{Ba}^+$), but in principle, they can also drive $^{138}\text{Ba}^+$ ($^{171}\text{Yb}^+$). As shown in Fig. 7.4 and Fig. 7.5, neither qubit have noticeable excitation when the other one is drove by the Raman beam. This part of crosstalk is too small to be detected due to the state preparation and measurement (SPAM) error.

But this part of crosstalk can be estimated in theory. Firstly, we assume the pulse laser comb differences are resonant with the qubits transition and only consider the energy structure of ions and laser wavelength. Detunings between 355 (532) nm laser and $^{138}\text{Ba}^+$ ($^{171}\text{Yb}^+$) $S_{1/2} \Leftrightarrow P_{1/2}, P_{3/2}$ transition are 238 (248) THz and 187 (347) THz. The Raman transition strengths of $^{171}\text{Yb}^+$ and $^{138}\text{Ba}^+$ depends on the laser wavelength are^[74]:

$$\Omega_{\text{Yb}} = \frac{I}{12} \left[-\frac{k_1}{\Delta_1} + \frac{k_2}{\Delta_2} \right], \quad (7.7)$$

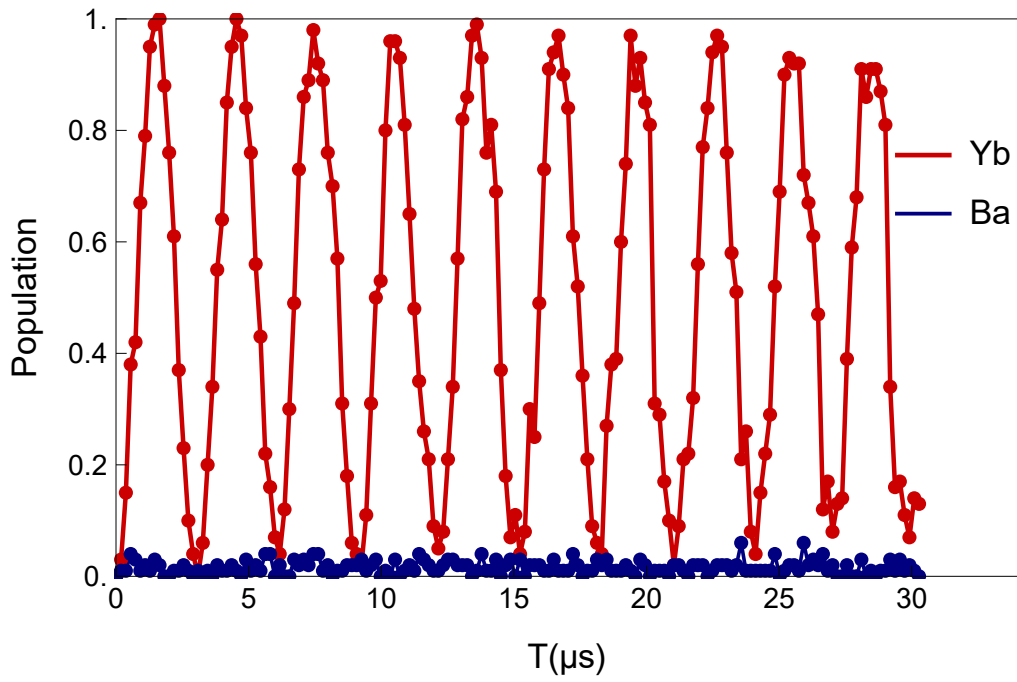


Figure 7.4 Crosstalk of $^{171}\text{Yb}^+$ carrier transition to $^{138}\text{Ba}^+$ ion.

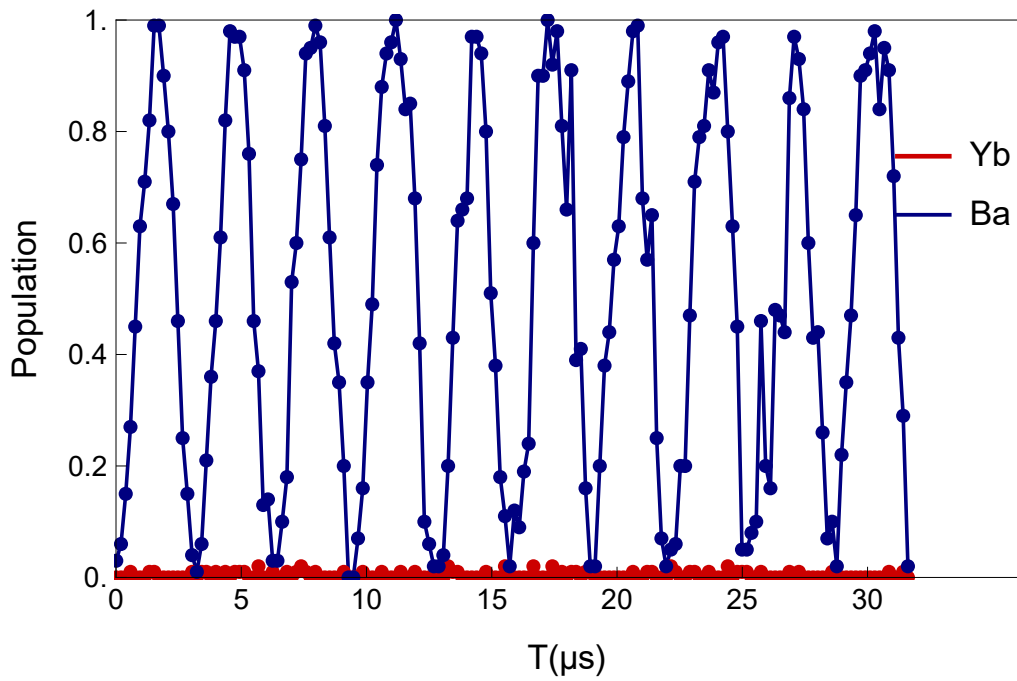


Figure 7.5 Crosstalk of $^{138}\text{Ba}^+$ carrier transition to $^{171}\text{Yb}^+$ ion.

$$\Omega_{\text{Ba}} = \frac{\sqrt{2}I}{12} \left[-\frac{k_1}{\Delta_1} + \frac{k_2}{\Delta_2} \right], \quad (7.8)$$

where subscript 1 and 2 refer to $P_{1/2}$ level and $P_{3/2}$ level. I is the laser intensity and $k_i = \gamma_i^2/I_{\text{sat},i}$. γ_i , $I_{\text{sat},i}$ and Δ_i are the natural linewidth, saturation intensity and detuning for corresponding level. For $^{171}\text{Yb}^+$, $k_1 = 3.00 \times 10^{13}$ s/Kg and $k_2 = 2.76 \times 10^{13}$ s/Kg. For $^{138}\text{Ba}^+$, $k_1 = 5.49 \times 10^{13}$ s/Kg and $k_2 = 3.46 \times 10^{13}$ s/Kg. In our experiment situation, the transition strength $\Omega_{\text{Yb},355} = \Omega_{\text{Ba},532} = (2\pi) 0.18$ MHz, which leads to $I_{532} = 1.11 \times 10^7$ W/m², $I_{355} = 1.06 \times 10^7$ W/m². Then the unwanted crosstalk transition strengths are:

$$|\Omega_{\text{Yb},532}| = \frac{I_{532}}{12} \left[\frac{k_1}{248} - \frac{k_2}{347} \right] = (2\pi) 0.006 \text{ MHz}, \quad (7.9)$$

$$|\Omega_{\text{Ba},355}| = \frac{\sqrt{2}I_{355}}{12} \left[\frac{k_1}{187} - \frac{k_2}{238} \right] = (2\pi) 0.009 \text{ MHz}, \quad (7.10)$$

Here, two ions are assumed to be uniformly illuminated by two lasers. However, in the real experiment, both beams are alignment to the target ion, which will further reduce the crosstalk.

Second part is the comb difference between two lasers. The repetition rate of our pulse laser is 80.097 MHz. The frequency shift between two 355 (532) nm beam combs is 12.5 (16.3) MHz to meet the $^{171}\text{Yb}^+$ ($^{138}\text{Ba}^+$) qubit splitting of 12642.8 (16.3) MHz. Then the undesirable Raman transitions have detuning of at least $|\Delta|/2\pi = 16.8 - 12.5 = 4.3$ MHz for both $^{138}\text{Ba}^+$ and $^{171}\text{Yb}^+$ qubit transition. This far-detuned coupling will have a limited maximum population for a single pulse of^[168]:

$$P_{\text{max,Yb},532} = \frac{\Omega_{\text{Yb},532}^2}{\Delta^2 + \Omega_{\text{Yb},532}^2} = \frac{0.006^2}{4.3^2 + 0.006^2} = 1.9 \times 10^{-6}, \quad (7.11)$$

$$P_{\text{max,Ba},355} = \frac{\Omega_{\text{Ba},355}^2}{\Delta^2 + \Omega_{\text{Ba},355}^2} = \frac{0.009^2}{4.3^2 + 0.009^2} = 4.3 \times 10^{-6}, \quad (7.12)$$

This amount of crosstalk is negligible for our experiment. And it is also possible to further suppress the crosstalk by design different polarization arrangements for two lasers, which has not been applied in our experiment.

7.4 Summary

In summary, we demonstrate the first loophole-free contextuality test with two species of trapped-ion system by using “Bell-like” inequality. For the loophole-free test of the quantum contextuality. We do not need the space-like separation that requires for the test of Bell inequality. Instead, we need to experimentally guarantee the measurements are ideal, which contains the property of reputability and compatibility without detection loophole. Therefore, it can be demonstrated in a local system without space-like separation and can be applicable to the self-testing randomness generation^[169].

We also demonstrate the technique to manipulate two different species of ion system, including entanglement, ground-state cooling, and individual readout. These techniques can also be applied to the field of ion-trap based quantum computing and quantum networking^[74]. For quantum computing, the measurement of one subsystem will not perturb the other one. Together with the two different species of ion entanglement gate, the individual readout can be performed with a single readout ion, and without perturbing neighbor ions. Which is suitable for quantum error correction. For quantum networking, two different species of ion system can be used to build photonic connection between separate traps. Subsystem with long coherence time can be used as memory ion^[37,69], and subsystem with suitable photon emission lines can be used as communication ion. Besides, the two species of ion system can perform sympathetic cooling technique to solve the thermal heating problem.

CHAPTER 8 QUANTUM FLUCTUATION THEOREMS AND QUANTUM TRAJECTORIES MEASUREMENT

This chapter is related to one of our ongoing projects: quantum fluctuation theorems and quantum trajectories measurement. We collaborate with Hyukjoon Kwon and M. S. Kim for the theory part^[170]. They have developed all the related theories of this chapter. Their quantum fluctuation theorems^[170] can be used to analyze the reversibility of quantum channels and can be straightforwardly verified in our system.

8.1 Classical fluctuation theorems

Assume $A = \{p(a)\}$ and $B = \{p'(b)\}$ are two physics systems, where $p(a)$ is the probability distributions of a in system A and $p'(b)$ is the probability distributions of b in system B . As shown in Fig. 8.1, C is a physical process from system A to B . And the microscopic entities a, b have forward process $a \xrightarrow{C} b$ with a forward transition probability $P_{\rightarrow}(a, b)$; And if there exists a reverse process \mathcal{R} , and this backward process $a \xleftarrow{\mathcal{R}} b$ can reverse the state of entity a with a backward transition probability $P_{\leftarrow}(a, b)$.

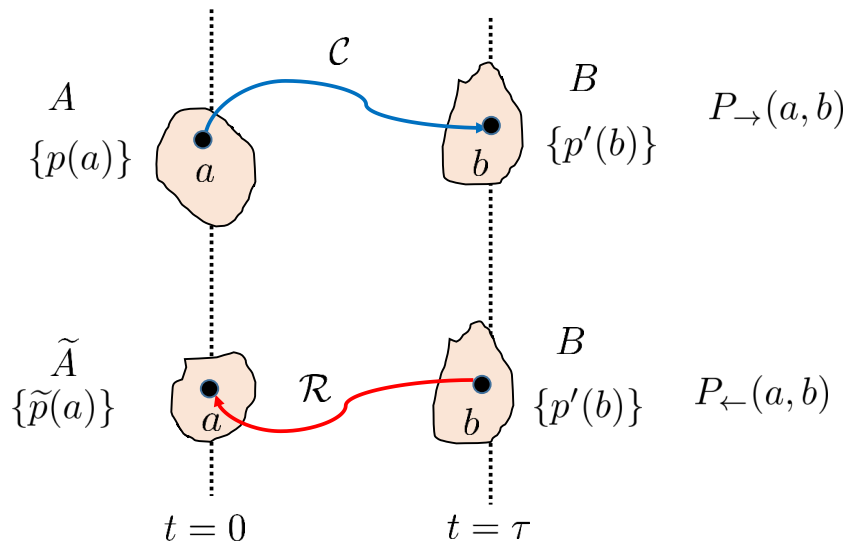


Figure 8.1 Fluctuation theorem model.

For the forward process $a \xrightarrow{C} b$, there are several definitions in the classical fluctuation theorems.

The information exchange $\delta s_{a \rightarrow b}$ and single-shot entropy difference $\delta q_{a \rightarrow b}$ ^[170] are:

$$\delta q_{a \rightarrow b} := -\log \left[\frac{Pt(a \rightarrow b)}{Pt(a \leftarrow b)} \right], \quad (8.1)$$

$$\delta s_{a \rightarrow b} := -\log p'(b) + \log p(a). \quad (8.2)$$

The single-shot entropy production is the difference between $\delta s_{a \rightarrow b}$ and $\delta q_{a \rightarrow b}$ ^[170]:

$$\sigma_{a \rightarrow b} := \delta s_{a \rightarrow b} - \delta q_{a \rightarrow b}. \quad (8.3)$$

The probability to get σ amount of entropy production is^[170]:

$$P_{\rightarrow}(\sigma) = \sum_{a,b} P_{\rightarrow}(a,b) \delta(\sigma - \sigma_{a \rightarrow b}). \quad (8.4)$$

Two important conclusions for classical fluctuation theorems are^[170]:

$$\frac{P_{\rightarrow}(\sigma)}{P_{\leftarrow}(-\sigma)} = e^{\sigma}, \quad (8.5)$$

$$\langle e^{-\sigma} \rangle = 1, \quad (8.6)$$

where Eq. 8.6 is the Jarzynski equality.

8.2 Quantum fluctuation theorems

Similar to classical theorems, a reverse process is necessary for contract quantum version fluctuation theorems. The Petz recovery map $\mathcal{R}_{\beta}^{\theta}(C(\beta)) = \beta$ is adopted as the reverse process, where $\beta = \sum_i r_i |i\rangle \langle i|$ is the reference state and can be recovered by $\mathcal{R}_{\beta}^{\theta}$. And $C(\beta) = \sum_{k'} r'_{k'} |k'\rangle \langle k'|$ is the state after forward process C . Petz recovery map has a freedom of θ :

$$\mathcal{R}_{\beta}^{\theta}(\rho) := (\mathcal{J}_{\beta}^{1/2+i\theta} \circ C^{\dagger} \circ \mathcal{J}_{C(\beta)}^{-1/2-i\theta})(\rho). \quad (8.7)$$

8.2.1 $\theta = 0$ case in Petz recovery map

$\mathcal{R}_{\beta}^{\theta}(C(\beta)) = \beta$ holds for all θ , which means that there are lots of chooses for the reverse process depending on the value of θ . For the simple case of $\theta = 0$,

$$\mathcal{R}_{\beta}(\rho) := (\mathcal{J}_{\beta}^{1/2} \circ C^{\dagger} \circ \mathcal{J}_{C(\beta)}^{-1/2})(\rho), \quad (8.8)$$

where

$$\begin{aligned} \mathcal{J}_A^a(\cdot) &= A^a(\cdot)A^{a\dagger} \\ \mathcal{C}(\cdot) &= \sum_m K_m(\cdot)K_m^\dagger \\ \mathcal{N}^\dagger(\cdot) &= \sum_m K_m^\dagger(\cdot)K_m. \end{aligned} \quad (8.9)$$

Based on this reverse process, quantum version fluctuation theorems are developed following the structure of classical fluctuation theorems. The forward process is denoted as $\rho \xrightarrow{C} C(\rho)$, where $\rho = \sum_\mu p_\mu |\psi_\mu\rangle\langle\psi_\mu|$ and $C(\rho) = \sum_{\nu'} p'_{\nu'} |\psi_{\nu'}\rangle\langle\psi_{\nu'}|$ are the input and output state. The transition probability of forward process $|i\rangle\langle j| \xrightarrow{C} |m'\rangle\langle n'|$ is $Pt(ij \rightarrow m'n') := \langle m' | C(|i\rangle\langle j|) |n'\rangle$. The backward probability for reverse process $|i\rangle\langle j| \leftarrow \mathcal{R}_\beta |m'\rangle\langle n'|$ is $Pt(ij \leftarrow m'n') := \langle i | \mathcal{R}_\beta(|m'\rangle\langle n'|) |j\rangle$.

Same as the classical theorems, quantum version definition of the information exchange $\delta q_{ij \rightarrow m'n'}$ and single-shot entropy difference $\delta s^{\mu \rightarrow \nu'}$ are:

$$\delta q_{ij \rightarrow m'n'} := -\log \left[\frac{Pt(ij \rightarrow m'n')}{\widetilde{Pt}^*(ij \leftarrow m'n')} \right] = \frac{1}{2} \log \frac{r_i r_j}{r'_{m'} r'_{n'}}, \quad (8.10)$$

$$\delta s^{\mu \rightarrow \nu'} := -\log p'(v') + \log p(\mu). \quad (8.11)$$

The single-shot entropy production is:

$$\sigma_{ij \rightarrow m'n'}^{\mu \rightarrow \nu'} := \delta s^{\mu \rightarrow \nu'} - \delta q_{ij \rightarrow m'n'}. \quad (8.12)$$

The probability to get σ amount of entropy production is:

$$P_{\rightarrow}(\sigma) = \sum_{\mu, i, j} \sum_{\nu', m', n'} P_{ij, m'n'}^{\mu, \nu'} \delta(\sigma - \sigma_{ij \rightarrow m'n'}^{\mu \rightarrow \nu'}), \quad (8.13)$$

where

$$P_{ij, m'n'}^{\mu, \nu'} := p_\mu \langle \phi'_{\nu'} | \Pi_{m'} C(\Pi_i |\psi_\mu\rangle\langle\psi_\mu| \Pi_j) \Pi_{n'} | \phi'_{\nu'} \rangle, \quad (8.14)$$

and $\Pi_i = |i\rangle\langle i|$.

Two conclusions for quantum fluctuation theorems are same as classical one:

$$\frac{P_{\rightarrow}(\sigma)}{P_{\leftarrow}(-\sigma)} = e^\sigma. \quad (8.15)$$

Jarzynski equality:

$$\langle e^{-\sigma} \rangle = 1. \quad (8.16)$$

8.2.2 $\theta \neq 0$ case in Petz recovery map

On the other side, if $\theta \neq 0$, information exchange $\delta q_{ij \rightarrow m'n'}$ is:

$$(\delta q_I)_{ij \rightarrow m'n'} := -\frac{1}{2} \log \frac{r'_{m'}}{r'_{n'}} + \frac{1}{2} \log \frac{r_i}{r_j}. \quad (8.17)$$

The single-shot entropy production is:

$$\sigma_{ij \rightarrow m'n'}^{\mu \rightarrow \nu'} := \delta s^{\mu \rightarrow \nu'} - [(\delta q_R)_{ij \rightarrow m'n'} + i(\delta q_I)_{ij \rightarrow m'n'}]. \quad (8.18)$$

The relation between single-shot entropy production in backward and forward process is:

$$\frac{P_{\rightarrow}(\sigma)}{P_{\leftarrow}^{\theta}(-\sigma^*)} = e^{\sigma_R - 2i\theta\sigma_I}. \quad (8.19)$$

8.3 Two point measurement (TPM) for quantum fluctuation theorems

To verify the conclusions of Eq. 8.15 and Eq. 8.16 in quantum fluctuation theorems, the central part is how to measure the value of $P_{ij, m'n'}^{\mu, \nu'}$ in Eq. 8.14, which can't be measured directly. This can be solved by two point measurement (TPM) shown in Fig. 8.2. $P(s, s')$

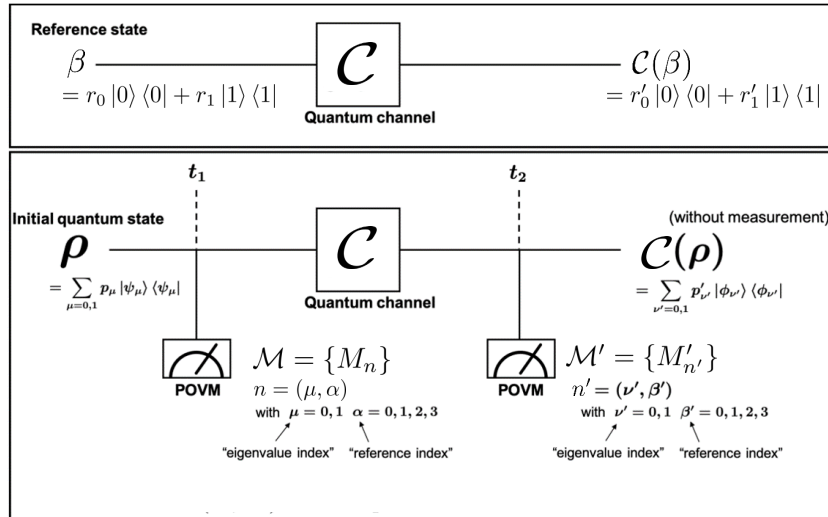


Figure 8.2 Two point measurement scheme.

is the two point measurement distribution and has the formula of:

$$P(s, s') = \text{Tr}[M'_{s'} C(M_s \rho M_s^\dagger) M'_{s'}^\dagger]. \quad (8.20)$$

This two-point measurement needs a two-step measurement shown in Fig. 8.3. And the first measurement is only applied to one of the qubit and the other one shouldn't be

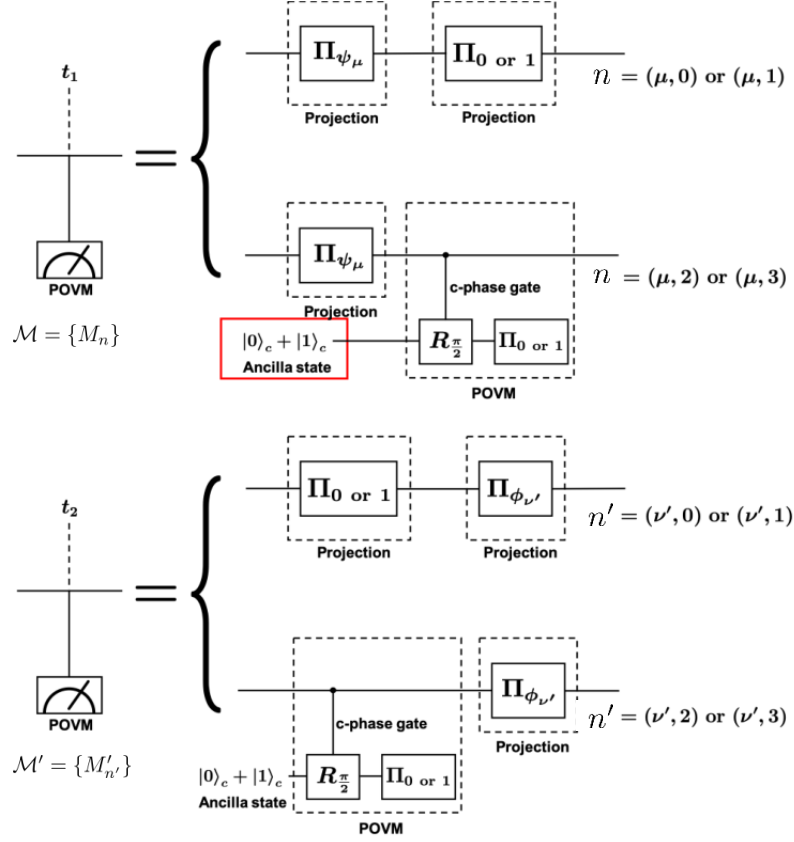


Figure 8.3 Measurements in the two point measurement.

affected, which is exactly what our multi-species ion trap system is good at. We use $^{138}\text{Ba}^+$ ion as the ancilla qubit to perform measurement due to the higher detection fidelity. We use the $^{171}\text{Yb}^+$ ion as the operation qubit due to the longer coherence time.

Once all the two-point measurement distributions are measured, we can get the value of $P_{ij,m'n'}^{\mu,\nu'}$. For mathematical simplicity, we define

$$P(a, b') := \text{Tr} \left[M'_{(\nu', b')} C \left(M_{(\mu, a)} \rho M_{(\mu, a)}^\dagger \right) M'_{(\nu', b')}^\dagger \right] \quad (8.21)$$

for fixed values of μ and ν' . First, we note that

$$P_{ii, k'k'}^{\mu, \nu'} = 4P(i, k') \quad (8.22)$$

with $i = 0, 1$ and $k' = 0, 1$. For $i = j$ and $k' \neq l'$, we define

$$Q(a, b') := P(a, b') - \frac{1}{2} \sum_{k'=0,1} P(a, k') \quad (8.23)$$

for $a \in \{0, 1\}$ and $b' \in \{2, 3\}$. We then obtain

$$\begin{aligned} P_{i,01}^{\mu,\nu'} &= 4[Q(i, 2) + iQ(i, 3)] \\ P_{i,10}^{\mu,\nu'} &= 4[Q(i, 2) - iQ(i, 3)]. \end{aligned} \quad (8.24)$$

Similarly, for $i \neq j$ and $k' = l'$, we obtain

$$P_{01,k'k'}^{\mu,\nu'} = 4 [Q(2, k') + iQ(3, k')] \quad (8.25)$$

and

$$P_{10,k'k'}^{\mu,\nu'} = 4 [Q(2, k') - iQ(3, k')], \quad (8.26)$$

where

$$Q(a, b') := P(a, b') - \frac{1}{2} \sum_{i=0,1} P(i, b') \quad (8.27)$$

for $a \in \{2, 3\}$ and $b' \in \{0, 1\}$. In order to obtain the TPM quasi-probability for $i \neq j$ and $k' \neq l'$, we additionally define

$$Q(a, b') := P(a, b') - \frac{1}{2} \left[\sum_{i=0,1} Q(i, b') - \sum_{k'=0,1} Q(a, k') \right] - \frac{1}{4} \bar{P} \quad (8.28)$$

for $a \in \{2, 3\}$ and $b' \in \{2, 3\}$, where $\bar{P} = \sum_{i=0,1} \sum_{k'=0,1} P(i, k')$. Finally, we obtain

$$\begin{pmatrix} P_{0101'}^{\mu,\nu'} \\ P_{0110'}^{\mu,\nu'} \\ P_{1001}^{\mu,\nu'} \\ P_{1010}^{\mu,\nu'} \end{pmatrix} = 4 \begin{pmatrix} 1 & i & i & -1 \\ 1 & -i & i & 1 \\ 1 & i & -i & 1 \\ 1 & -i & -i & -1 \end{pmatrix} \begin{pmatrix} Q(2, 2) \\ Q(2, 3) \\ Q(3, 2) \\ Q(3, 3) \end{pmatrix}, \quad (8.29)$$

thus we conclude that every element of $P_{ij,k'l'}^{\mu,\nu'}$ is expressed in terms of $P(m, m')$. Then, $P_{\rightarrow}(\sigma)$ for both real and imaginary σ can be obtained from the TPM quasi-probability distribution $P_{ij,k'l'}^{\mu,\nu'}$.

8.4 Quantum trajectories measurement

The two-point measurement can be used to construct some parameters that can't be measured directly or even not observable, such as the quantum correlation function. If we extend the sequential measurement to more than two-point, it may have more interesting applications. Here we extend the measurement step to as long as possible, which is basically limited by our gate fidelity. With this long sequential measurement, we can get a series of measurement results, which are the so-called quantum trajectory. The quantum trajectory can be measured in the scheme shown in

Fig. 8.4. And the quantum trajectory can be used to construct other parameters that can't be measured directly. The theoretical and experimental details are still under developing.

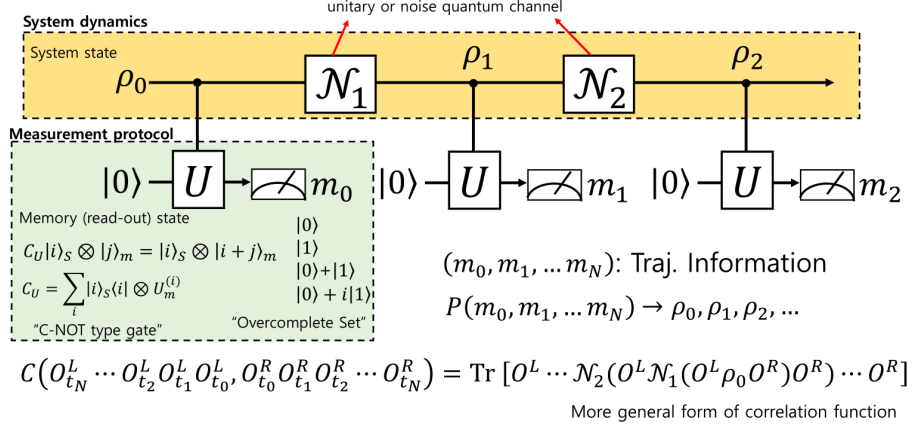


Figure 8.4 Experiment scheme to measure quantum trajectory. The yellow box shows the dynamics of the system. ρ_0 is the input mixed state. \mathcal{N}_1 and \mathcal{N}_2 and so on are the unitary or noise quantum channel. ρ_1 and ρ_2 are the states after channels. For the measurement protocol, an ancilla qubit is used to get the information of operation qubit. A C-NOT type gate is applied between two qubits and then the ancilla qubit is measured in an overcomplete set.

CHAPTER 9 SUMMARY AND OUTLOOK

My Ph.D. research only focuses on the trapped $^{171}\text{Yb}^+ - ^{138}\text{Ba}^+$ ion system. In the very beginning, my plan was first to improve the entanglement fidelity of $^{171}\text{Yb}^+ - ^{138}\text{Ba}^+$ ion and then develop the 1762 nm laser individual addressing system to increase the number of $^{138}\text{Ba}^+$ ion. However, due to the brokenness of the HighQ Raman laser, which was essential for $^{171}\text{Yb}^+ - ^{138}\text{Ba}^+$ entanglement gate, this plan was interrupted. Since the waiting time in the laser repair process is too long, I changed to the project about extending coherence time of $^{171}\text{Yb}^+$ ion qubit. I spend about one year increasing the coherence time to hour level. Then I restarted the $^{171}\text{Yb}^+ - ^{138}\text{Ba}^+$ entanglement project after the HighQ Raman laser was fixed. But the project was delayed for another half a year due to the COVID-19 campus closure. Fortunately, the fidelity of $^{171}\text{Yb}^+ - ^{138}\text{Ba}^+$ MS gate has now been improved to more than 98%. Further improvement of the fidelity is possible if the system is updated to the blade trap and laser modulation techniques are used, such as phase modulation and frequency modulation. Then based on the entangled state obtained by MS gate, we implemented the first loophole-free quantum contextuality test.

I believe our $^{171}\text{Yb}^+ - ^{138}\text{Ba}^+$ platform will play an important role in the future, since sympathetic cooling and entanglement between different species of ions are key techniques for realizing large-scale ion-based quantum computers. And individual shelving is also a possible solution for feedback-involved quantum circuit. In order to further develop this platform, we first need to develop the individual shelving system of $^{138}\text{Ba}^+$ ion. And it is also interesting to change $^{138}\text{Ba}^+$ to other isotopes, such as $^{137}\text{Ba}^+$ or $^{133}\text{Ba}^+$.

REFERENCES

- [1] DiVincenzo D P. Quantum computation[J]. *Science*, 1995, 270(5234):255-261.
- [2] Lidar D A, Chuang I L, Whaley K B. Decoherence-free subspaces for quantum computation [J]. *Phys. Rev. Lett.*, 1998, 81(12):2594-2597.
- [3] Divincenzo D P. The physical implementation of quantum computation[J]. *Fortschritte der Physik*, 2000, 48(9-11):771-783.
- [4] Ladd T D, Jelezko F, Laflamme R, et al. Quantum computers[J]. *Nature*, 2010, 464:45-53.
- [5] Sangouard N, Simon C, De Riedmatten H, et al. Quantum repeaters based on atomic ensembles and linear optics[J]. *Rev. Mod. Phys.*, 2011, 83(1):33.
- [6] Briegel H J, Dür W, Cirac J I, et al. Quantum repeaters: The role of imperfect local operations in quantum communication[J]. *Phys. Rev. Lett.*, 1998, 81:5932-5935.
- [7] Hartmann L, Kraus B, Briegel H J, et al. Role of memory errors in quantum repeaters[J]. *Phys. Rev. A*, 2007, 75(17):032310.
- [8] Razavi M, Piani M, Lutkenhaus N. Quantum repeaters with imperfect memories: Cost and scalability[J]. *Phys. Rev. A*, 2009, 80(3):032301.
- [9] Duan L M, Monroe C. Quantum networks with trapped ions[J]. *Rev. Mod. Phys.*, 2012, 82: 1209-1224.
- [10] Dudin Y O, Li L, Kuzmich A. Light storage on the time scale of a minute[J]. *Phys. Rev. A*, 2013, 87(3):031801.
- [11] Pezze L, Smerzi A, Oberthaler M K, et al. Quantum metrology with nonclassical states of atomic ensembles[J]. *Rev. Mod. Phys.*, 2018, 90(3):035005.
- [12] Kotler S, Akerman N, Glickman Y, et al. Single-ion quantum lock-in amplifier[J]. *Nature*, 2011, 473(7345):61-65.
- [13] Degen C L, Reinhard F, Cappellaro P. Quantum sensing[J]. *Rev. Mod. Phys.*, 2017, 89(3): 035002.
- [14] Feynman R P. Simulating physics with computers[J]. *Int. J. Theor. Phys.*, 1982, 21(6-7):467-488.
- [15] Shor P W. Algorithms for quantum computation: discrete logarithms and factoring[C]// *Proceedings 35th annual symposium on foundations of computer science*. Ieee, 1994:124-134.
- [16] Vandersypen L M, Steffen M, Breyta G, et al. Experimental realization of shor's quantum factoring algorithm using nuclear magnetic resonance[J]. *Nature*, 2001, 414(6866):883-887.
- [17] Ekert A, Jozsa R. Quantum computation and shor's factoring algorithm[J]. *Rev. Mod. Phys.*, 1996, 68(3):733.
- [18] Grover L K. Quantum computers can search arbitrarily large databases by a single query[J]. *Phys. Rev. Lett.*, 1997, 79(23):4709.
- [19] Long G L. Grover algorithm with zero theoretical failure rate[J]. *Phys. Rev. A*, 2001, 64(2): 022307.

REFERENCES

- [20] O'Brien J L. Optical quantum computing[J]. *Science*, 2007, 318(5856):1567-1570.
- [21] Prawer S, Greentree A D. Diamond for quantum computing[J]. *Science*, 2008, 320(5883):1601-1602.
- [22] Figgatt C, Ostrander A, Linke N M, et al. Parallel entangling operations on a universal ion-trap quantum computer[J]. *Nature*, 2019, 572(7769):368-372.
- [23] Lu Y, Zhang S, Zhang K, et al. Global entangling gates on arbitrary ion qubits[J]. *Nature*, 2019, 572(7769):363-367.
- [24] Nakamura Y, Pashkin Y A, Tsai J S. Coherent control of macroscopic quantum states in a single-cooper-pair box[J]. *Nature*, 1999, 398(6730):786-788.
- [25] Morsch O, Oberthaler M. Dynamics of bose-einstein condensates in optical lattices[J]. *Rev. Mod. Phys.*, 2006, 78(1):179.
- [26] Wiesner S. Conjugate coding[J]. *SIGACT News*, 1983, 15:78-88.
- [27] Pastawski F, Yao N Y, Jiang L, et al. Unforgeable noise-tolerant quantum tokens[J]. *Proc. Natl. Acad. Sci. U.S.A.*, 2012, 109:16079-16082.
- [28] Steger M, Saeedi K, Thewalt M, et al. Quantum information storage for over 180 s using donor spins in a ²⁸si "semiconductor vacuum"[J]. *Science*, 2012, 336(6086):1280-1283.
- [29] Saeedi K, Simmons S, Salvail J Z, et al. Room-temperature quantum bit storage exceeding 39 minutes using ionized donors in silicon-28[J]. *Science*, 2013, 342(6160):830-833.
- [30] Zhong M, Hedges M P, Ahlefeldt R L, et al. Optically addressable nuclear spins in a solid with a six-hour coherence time[J]. *Nature*, 2015, 517(7533):177-180.
- [31] Bollinger J, Heizen D, Itano W, et al. A 303-mhz frequency standard based on trapped be⁺ ions[J]. *IEEE Trans. Instrum. Meas.*, 1991, 40:126-128.
- [32] Fisk P, Sellars M, Lawn M, et al. Very high q microwave spectroscopy on trapped ¹⁷¹yb⁺ ions: application as a frequency standard[J]. *IEEE Trans. Instrum. Meas.*, 1995, 44:113-116.
- [33] Langer C, Ozeri R, Jost J D, et al. Long-lived qubit memory using atomic ions[J]. *Phys. Rev. Lett.*, 2005, 95:060502.
- [34] Häffner H, Schmidt-Kaler F, Hänsel W, et al. Robust entanglement[J]. *Appl. Phys. B*, 2005, 81:151-153.
- [35] Harty T P, Allcock D T C, Ballance C J, et al. High-fidelity preparation, gates, memory, and readout of a trapped-ion quantum bit[J]. *Phys. Rev. Lett.*, 2014, 113:220501.
- [36] Kotler S, Akerman N, Navon N, et al. Measurement of the magnetic interaction between two bound electrons of two separate ions[J]. *Nature*, 2014, 510(7505):376-380.
- [37] Wang Y, Um M, Zhang J, et al. Single-qubit quantum memory exceeding ten-minute coherence time[J]. *Nat. Photonics*, 2017, 11(10):646-650.
- [38] Nielsen M A, Chuang I L. *Quantum computation and quantum information*[M]. Cambridge university press, 2010.
- [39] May V, Kühn O. *Charge and energy transfer dynamics in molecular systems*[M]. John Wiley and Sons, Ltd, 2007.

REFERENCES

- [40] Sarvepalli P K, Klappenecker A, Rotteler M. Asymmetric quantum codes: constructions, bounds and performance[J]. *Proceedings of the Royal Society London, Ser. A*, 2009, 465(2105): 1645-1672.
- [41] DiVincenzo D P, Leung D W, Terhal B M. Quantum data hiding[J]. *IEEE Trans. Inf. Theory*, 2002, 48(3):580-598.
- [42] Winter A, Yang D. Operational resource theory of coherence[J]. *Phys. Rev. Lett.*, 2016, 116(12):120404.
- [43] Streltsov A, Adesso G, Plenio M B. Colloquium : Quantum coherence as a resource[J]. *Rev. Mod. Phys.*, 2017, 89(4):041003.
- [44] Hensen B, Bernien H, Dréau A E, et al. Loophole-free bell inequality violation using electron spins separated by 1.3 kilometres[J]. *Nature*, 2015, 526(7575):682-686.
- [45] Giustina M, Versteegh M A M, Wengerowsky S, et al. Significant-loophole-free test of bell's theorem with entangled photons[J]. *Phys. Rev. Lett.*, 2015, 115:250401.
- [46] Shalm L K, Meyer-Scott E, Christensen B G, et al. Strong loophole-free test of local realism [J]. *Phys. Rev. Lett.*, 2015, 115:250402.
- [47] Rosenfeld W, Burchardt D, Garthoff R, et al. Event-ready bell test using entangled atoms simultaneously closing detection and locality loopholes[J]. *Phys. Rev. Lett.*, 2017, 119:010402.
- [48] Kochen S, Specker E P. The problem of hidden variables in quantum mechanics[J]. *J. Math. Mech.*, 1967, 17:59-87.
- [49] Klyachko A A, Can M A, Binicioglu S, et al. Simple test for hidden variables in spin-1 systems [J]. *Phys. Rev. Lett.*, 2008, 101(2):020403.
- [50] Cabello A. Experimentally testable state-independent quantum contextuality[J]. *Phys. Rev. Lett.*, 2008, 101:210401.
- [51] Chiribella G, Yuan X. Measurement sharpness cuts nonlocality and contextuality in every physical theory[J]. *arXiv preprint arXiv:1404.3348*, 2014.
- [52] Chiribella G, Yuan X. Bridging the gap between general probabilistic theories and the device-independent framework for nonlocality and contextuality[J]. *Inf. Comput.*, 2016, 250:15-49.
- [53] Cabello A. Quantum correlations from simple assumptions[J]. *Phys. Rev. A*, 2019, 100:032120.
- [54] Pearle P M. Hidden-variable example based upon data rejection[J]. *Phys. Rev. D*, 1970, 2:1418.
- [55] Clauser J F, Horne M A, Shimony A, et al. Proposed experiment to test local hidden-variable theories[J]. *Phys. Rev. Lett.*, 1969, 23:880-884.
- [56] Horodecki R, Horodecki M, Horodecki P. Teleportation, bell's inequalities and inseparability [J]. *Phys. Lett. A*, 1996, 222(1-2):21-25.
- [57] Collins D, Gisin N. A relevant two qubit bell inequality inequivalent to the chsh inequality[J]. *J. Phys. A: Math. Gen.*, 2004, 37(5):1775.
- [58] Wehner S. Tsirelson bounds for generalized clausner-horne-shimony-holt inequalities[J]. *Phys. Rev. A*, 2006, 73(2):022110.
- [59] Cabello A. Simple explanation of the quantum violation of a fundamental inequality[J]. *Phys. Rev. Lett.*, 2013, 110(6):060402.

REFERENCES

- [60] Araújo M, Quintino M T, Budroni C, et al. All noncontextuality inequalities for the n -cycle scenario[J]. *Phys. Rev. A*, 2013, 88(2):022118.
- [61] Cabello A. The problem of quantum correlations and the totalitarian principle[J]. *Phil. Trans. R. Soc. A.*, 2019, 377:20190316.
- [62] Gisin N, Gisin B. A local hidden variable model of quantum correlation exploiting the detection loophole[J]. *Phys. Lett. A*, 1999, 260(5):323-327.
- [63] Brunner N, Gisin N, Scarani V, et al. Detection loophole in asymmetric bell experiments[J]. *Phys. Rev. Lett.*, 2007, 98(22):220403.
- [64] Christensen B G, McCusker K T, Altepeter J B, et al. Detection-loophole-free test of quantum nonlocality, and applications[J]. *Phys. Rev. Lett.*, 2013, 111(13):130406.
- [65] Karimi E, Leach J, Slussarenko S, et al. Spin-orbit hybrid entanglement of photons and quantum contextuality[J]. *Phys. Rev. A*, 2010, 82(2):022115.
- [66] Um M, Zhang X, Zhang J, et al. Experimental certification of random numbers via quantum contextuality[J]. *Sci. Rep.*, 2013, 3(1):1627.
- [67] Um M, Zhao Q, Zhang J, et al. Randomness expansion secured by quantum contextuality[J]. *Phys. Rev. Appl.*, 2020, 13:034077.
- [68] Gühne O, Kleinmann M, Cabello A, et al. Compatibility and noncontextuality for sequential measurements[J]. *Phys. Rev. A*, 2010, 81:022121.
- [69] Wang P, Luan C Y, Qiao M, et al. Single ion qubit with estimated coherence time exceeding one hour[J]. *Nat. Commun.*, 2021, 12(1):1-8.
- [70] Paul W. Electromagnetic traps for charged and neutral particles[J]. *Rev. Mod. Phys.*, 1990, 62(3):531.
- [71] Ramsey N F. Experiments with separated oscillatory fields and hydrogen masers[J]. *Science*, 1990, 248(4963):1612-1619.
- [72] Dehmelt H. Experiments with an isolated subatomic particle at rest[J]. *Rev. Mod. Phys.*, 1990, 62(3):525.
- [73] Santra S, Muralidharan S, Lichtman M, et al. Quantum repeaters based on two species trapped ions[J]. *New J. Phys.*, 2019, 21(7):073002.
- [74] Inlek I V, Crocker C, Lichtman M, et al. Multispecies trapped-ion node for quantum networking [J]. *Phys. Rev. Lett.*, 2017, 118:250502.
- [75] Larson D, Bergquist J C, Bollinger J J, et al. Sympathetic cooling of trapped ions: A laser-cooled two-species nonneutral ion plasma[J]. *Phys. Rev. Lett.*, 1986, 57(1):70.
- [76] Kielpinski D, King B, Myatt C, et al. Sympathetic cooling of trapped ions for quantum logic [J]. *Phys. Rev. A*, 2000, 61(3):032310.
- [77] Pino J M, Dreiling J M, Figgatt C, et al. Demonstration of the qccd trapped-ion quantum computer architecture[J]. *arXiv preprint arXiv:2003.01293*, 2020.
- [78] Wübbena J B, Amairi S, Mandel O, et al. Sympathetic cooling of mixed-species two-ion crystals for precision spectroscopy[J]. *Phys. Rev. A*, 2012, 85(4):043412.

REFERENCES

- [79] Negnevitsky V, Marinelli M, Mehta K K, et al. Repeated multi-qubit readout and feedback with a mixed-species trapped-ion register[J]. *Nature*, 2018, 563(7732):527-531.
- [80] Cory D G, Price M, Maas W, et al. Experimental quantum error correction[J]. *Phys. Rev. Lett.*, 1998, 81(10):2152.
- [81] Chiaverini J, Leibfried D, Schaetz T, et al. Realization of quantum error correction[J]. *Nature*, 2004, 432(7017):602-605.
- [82] Calderbank A R, Rains E M, Shor P W, et al. Quantum error correction and orthogonal geometry [J]. *Phys. Rev. Lett.*, 1997, 78(3):405.
- [83] Zhang J. Entanglement of multi-species ions mediated by phonons[D]. Tsinghua University, 2018.
- [84] Um M. Quantum randomness certification secured by quantum contextuality with trapped ion system[D]. Tsinghua University, 2019.
- [85] Olmschenk S M. Quantum teleportation between distant matter qubits[D]. University of Michigan, 2009.
- [86] Leibbrandt D R, Clark R J, Labaziewicz J, et al. Laser ablation loading of a surface-electrode ion trap[J]. *Phys. Rev. A*, 2007, 76(5):055403.
- [87] Sheridan K, Lange W, Keller M. All-optical ion generation for ion trap loading[J]. *Appl. Phys. B*, 2011, 104(4):755-761.
- [88] Zimmermann K, Okhapkin M, Herrera-Sancho O, et al. Laser ablation loading of a radiofrequency ion trap[J]. *Appl. Phys. B*, 2012, 107(4):883-889.
- [89] Vrijsen G, Aikyo Y, Spivey R F, et al. Efficient isotope-selective pulsed laser ablation loading of 174 yb^+ ions in a surface electrode trap[J]. *Opt. Express*, 2019, 27(23):33907.
- [90] Araneda G, Cerchiarri G, Higginbottom D B, et al. The panopticon device: An integrated paul-trap–hemispherical mirror system for quantum optics[J]. *Rev. Sci. Instrum.*, 2020, 91(11):113201.
- [91] Leschhorn G, Hasegawa T, Schaetz T. Efficient photo-ionization for barium ion trapping using a dipole-allowed resonant two-photon transition[J]. *Appl. Phys. B*, 2012, 108(1):159-165.
- [92] James D F V. Quantum dynamics of cold trapped ions with application to quantum computation [J]. *Appl. Phys. B*, 1998, 66(2):181-190.
- [93] Cirac J I, Zoller P. Quantum computations with cold trapped ions[J]. *Phys. Rev. Lett.*, 1995, 74 (20):4091-4094.
- [94] Wright K, Beck K M, Debnath S, et al. Benchmarking an 11-qubit quantum computer[J]. *Nat. Commun.*, 2019, 10(1):5464.
- [95] Sangouard N, Dubessy R, Simon C. Quantum repeaters based on single trapped ions[J]. *Phys. Rev. A*, 2009, 79(4):042340.
- [96] Epstein R J, Seidelin S, Leibfried D, et al. Simplified motional heating rate measurements of trapped ions[J]. *Phys. Rev. A*, 2007, 76:033411.
- [97] Wesenberg J, Epstein R, Leibfried D, et al. Fluorescence during doppler cooling of a single trapped atom[J]. *Phys. Rev. A*, 2007, 76(5):053416.

REFERENCES

- [98] Yuan X, Zhou H, Cao Z, et al. Intrinsic randomness as a measure of quantum coherence[J]. *Phys. Rev. A*, 2015, 92:022124.
- [99] Yuan X, Liu Y, Zhao Q, et al. Universal and operational benchmarking of quantum memories [J]. arXiv preprint arXiv:1907.02521, 2019.
- [100] Ruster T, Schmiegelow C T, Kaufmann H, et al. A long-lived Zeeman trapped-ion qubit[J]. *Appl. Phys. B*, 2016, 122(10):254.
- [101] Biercuk M J, Uys H, VanDevender A P, et al. Optimized dynamical decoupling in a model quantum memory[J]. *Nature*, 2009, 458(7241):996-1000.
- [102] Kotler S, Akerman N, Glickman Y, et al. Nonlinear single-spin spectrum analyzer[J]. *Phys. Rev. Lett.*, 2013, 110(11):110503.
- [103] Ball H, Oliver W D, Biercuk M J. The role of master clock stability in quantum information processing[J]. *npj Quantum Information*, 2016, 2(1):16033.
- [104] Sepiol M A, Hughes A C, Tarlton J E, et al. Probing qubit memory errors at the part-per-million level[J]. *Phys. Rev. Lett.*, 2019, 123:110503.
- [105] Shen C, Duan L. Correcting detection errors in quantum state engineering through data processing[J]. *New J. of Phys.*, 2012, 14(5):053053.
- [106] Khodjasteh K, Sastrawan J, Hayes D, et al. Designing a practical high-fidelity long-time quantum memory[J]. *Nat. Commun.*, 2013, 4(1):1-8.
- [107] Souza A M, Álvarez G A, Suter D. Robust dynamical decoupling for quantum computing and quantum memory[J]. *Phys. Rev. Lett.*, 2011, 106(24):240501.
- [108] Fiurášek J, Hradil Z. Maximum-likelihood estimation of quantum processes[J]. *Phys. Rev. A*, 2001, 63(2):020101.
- [109] Gilchrist A, Langford N K, Nielsen M A. Distance measures to compare real and ideal quantum processes[J]. *Phys. Rev. A*, 2005, 71:062310.
- [110] O'Brien J L, Pryde G J, Gilchrist A, et al. Quantum process tomography of a controlled-not gate[J]. *Phys. Rev. Lett.*, 2004, 93:080502.
- [111] Riebe M, Kim K, Schindler P, et al. Process tomography of ion trap quantum gates[J]. *Phys. Rev. Lett.*, 2006, 97:220407.
- [112] Lundberg M, Svensson L. The haar measure and the generation of random unitary matrices[C]// *Processing Workshop Proceedings, 2004 Sensor Array and Multichannel Signal. IEEE*, 2004: 114-118.
- [113] Emerson J, Alicki R, Życzkowski K. Scalable noise estimation with random unitary operators [J]. *J. Opt. B: Quantum Semiclassical Opt.*, 2005, 7(10):S347.
- [114] Walter T. Characterizing frequency stability: a continuous power-law model with discrete sampling[J]. *IEEE Transactions on Instrumentation and Measurement*, 1994, 43(1):69-79.
- [115] Ozeri R, Langer C, Jost J, et al. Hyperfine coherence in the presence of spontaneous photon scattering[J]. *Phys. Rev. Lett.*, 2005, 95(3):030403.
- [116] Uys H, Biercuk M, VanDevender A, et al. Decoherence due to elastic rayleigh scattering[J]. *Phys. Rev. Lett.*, 2010, 105(20):200401.

REFERENCES

- [117] Campbell W, Mizrahi J, Quraishi Q, et al. Ultrafast gates for single atomic qubits[J]. *Phys. Rev. Lett.*, 2010, 105(9):090502.
- [118] Hankin A M, Clements E R, Huang Y, et al. Systematic uncertainty due to background-gas collisions in trapped-ion optical clocks[J]. *Phys. Rev. A*, 2019, 100:033419.
- [119] Knill E, Leibfried D, Reichle R, et al. Randomized benchmarking of quantum gates[J]. *Phys. Rev. A*, 2008, 77:012307.
- [120] Fitzpatrick R. Quantum mechanics[M]. World Scientific, 2015.
- [121] Kielpinski D, Monroe C, Wineland D J. Architecture for a large-scale ion-trap quantum computer[J]. *Nature*, 2002, 417(6890):709-711.
- [122] Lekitsch B, Weidt S, Fowler A G, et al. Blueprint for a microwave trapped ion quantum computer[J]. *Sci. Adv.*, 2017, 3(2):e1601540.
- [123] Monroe C, Kim J. Scaling the ion trap quantum processor[J]. *Science*, 2013, 339(6124):1164-1169.
- [124] Pagano G, Hess P W, Kaplan H B, et al. Cryogenic trapped-ion system for large scale quantum simulation[J]. *Quantum Sci. Technol.*, 2018, 4(1):014004.
- [125] Keller J, Kalincev D, Burgermeister T, et al. Probing time dilation in coulomb crystals in a high-precision ion trap[J]. *Phys. Rev. Applied*, 2019, 11:011002.
- [126] Hayes D, Matsukevich D N, Maunz P, et al. Entanglement of atomic qubits using an optical frequency comb[J]. *Phys. Rev. Lett.*, 2010, 104:140501.
- [127] Lechner R, Maier C, Hempel C, et al. Electromagnetically-induced-transparency ground-state cooling of long ion strings[J]. *Phys. Rev. A*, 2016, 93:053401.
- [128] Roos C, Zeiger T, Rohde H, et al. Quantum state engineering on an optical transition and decoherence in a paul trap[J]. *Phys. Rev. Lett.*, 1999, 83:4713-4716.
- [129] Morigi G, Walther H. Two-species coulomb chains for quantum information[J]. *The European Physical Journal D-Atomic, Molecular, Optical and Plasma Physics*, 2001, 13(2):261-269.
- [130] Home J P. Quantum science and metrology with mixed-species ion chains[J]. *Adv. At. Mol. Opt. Phys.*, 2013, 62:231-277.
- [131] Bell J S. On the problem of hidden variables in quantum mechanics[J]. *Rev. Mod. Phys.*, 1966, 38(3):447-452.
- [132] Anders J, Browne D E. Computational power of correlations[J]. *Phys. Rev. Lett.*, 2009, 102:050502.
- [133] Raussendorf R. Contextuality in measurement-based quantum computation[J]. *Phys. Rev. A*, 2013, 88:022322.
- [134] Howard M, Wallman J, Veitch V, et al. Contextuality supplies the 'magic' for quantum computation[J]. *Nature*, 2014, 510(7505):351-5.
- [135] Delfosse N, Allard Guerin P, Bian J, et al. Wigner function negativity and contextuality in quantum computation on rebits[J]. *Phys. Rev. X*, 2015, 5:021003.
- [136] Kirchmair G, Zähringer F, Gerritsma R, et al. State-independent experimental test of quantum contextuality[J]. *Nature*, 2009, 460(7254):494-497.

REFERENCES

- [137] Zhang X, Um M, Zhang J, et al. State-independent experimental test of quantum contextuality with a single trapped ion[J]. *Phys. Rev. Lett.*, 2013, 110(7):070401.
- [138] Leupold F M, Malinowski M, Zhang C, et al. Sustained state-independent quantum contextual correlations from a single ion[J]. *Phys. Rev. Lett.*, 2018, 120:180401.
- [139] Malinowski M, Zhang C, Leupold F M, et al. Probing the limits of correlations in an indivisible quantum system[J]. *Phys. Rev. A*, 2018, 98:050102.
- [140] Michler M, Weinfurter H, Żukowski M. Experiments towards falsification of noncontextual hidden variable theories[J]. *Phys. Rev. Lett.*, 2000, 84:5457-5461.
- [141] Huang Y F, Li C F, Zhang Y S, et al. Experimental test of the kochen-specker theorem with single photons[J]. *Phys. Rev. Lett.*, 2003, 90:250401.
- [142] Amsellem E, Rådmark M, Bourennane M, et al. State-independent quantum contextuality with single photons[J]. *Phys. Rev. Lett.*, 2009, 103(16):160405.
- [143] Lapkiewicz R, Li P, Schaeff C, et al. Experimental non-classicality of an indivisible quantum system[J]. *Nature*, 2011, 474(7352):490-493.
- [144] Zu C, Wang Y X, Deng D L, et al. State-independent experimental test of quantum contextuality in an indivisible system[J]. *Phys. Rev. Lett.*, 2012, 109:150401.
- [145] D'Ambrosio V, Herbauts I, Amsellem E, et al. Experimental implementation of a kochen-specker set of quantum tests[J]. *Phys. Rev. X*, 2013, 3:011012.
- [146] Ahrens J, Amsellem E, Cabello A, et al. Two fundamental experimental tests of nonclassicality with qutrits[J]. *Sci. Rep.*, 2013, 3(1):2170.
- [147] Marques B, Ahrens J, Nawareg M, et al. Experimental observation of hardy-like quantum contextuality[J]. *Phys. Rev. Lett.*, 2014, 113:250403.
- [148] Hasegawa Y, Loidl R, Badurek G, et al. Violation of a bell-like inequality in single-neutron interferometry[J]. *Nature*, 2003, 425(6953):45-48.
- [149] Bartosik H, Klepp J, Schmitzer C, et al. Experimental test of quantum contextuality in neutron interferometry[J]. *Phys. Rev. Lett.*, 2009, 103:040403.
- [150] Moussa O, Ryan C A, Cory D G, et al. Testing contextuality on quantum ensembles with one clean qubit[J]. *Phys. Rev. Lett.*, 2010, 104:160501.
- [151] Jerger M, Reshitnyk Y, Oppliger M, et al. Contextuality without nonlocality in a superconducting quantum system[J]. *Nat. Commun.*, 2016, 7:12930.
- [152] van Dam S B, Cramer J, Taminiau T H, et al. Multipartite entanglement generation and contextuality tests using nondestructive three-qubit parity measurements[J]. *Phys. Rev. Lett.*, 2019, 123:050401.
- [153] Lüders G. Concerning the state-change due to the measurement process[J]. *Annalen der Physik*, 2006, 15(9):663-670.
- [154] Neumark M. Self-adjoint extensions of the second kind of a symmetric operator[J]. *Bull. Acad. Sci. USSR. Ser. Math.*, 1940, 4:90-104.
- [155] Neumark M. Spectral functions of a symmetric operator[J]. *Izvestiya Rossiiskoi Akademii Nauk. Seriya Matematicheskaya*, 1940, 4(3):277-318.

REFERENCES

- [156] Naimark M A. On a representation of additive operator set functions[C]//Dokl. Akad. Nauk SSSR: volume 41. 1943:373-375.
- [157] Holevo A S. Probabilistic and statistical aspects of quantum theory: volume 1[M]. Springer Science & Business Media, 2011.
- [158] Pokorny F, Zhang C, Higgins G, et al. Tracking the dynamics of an ideal quantum measurement [J]. Phys. Rev. Lett., 2020, 124:080401.
- [159] Peres A. Quantum theory: concepts and methods: volume 57[M]. Springer Science & Business Media, 2006.
- [160] Heinosaari T, Miyadera T, Ziman M. An invitation to quantum incompatibility[J]. J. Phys. A-Math. Theor., 2016, 49(12):123001.
- [161] Tan T R, Gaebler J P, Lin Y, et al. Multi-element logic gates for trapped-ion qubits[J]. Nature, 2015, 528(7582):380-3.
- [162] Ballance C J, Schafer V M, Home J P, et al. Hybrid quantum logic and a test of bell's inequality using two different atomic isotopes[J]. Nature, 2015, 528(7582):384-6.
- [163] Bruzewicz C D, McConnell R, Stuart J, et al. Dual-species, multi-qubit logic primitives for ca+/sr+ trapped-ion crystals[J]. NPJ Quantum Inf., 2019, 5(1):102.
- [164] Vorob'ev N N. Consistent families of measures and their extensions[J]. Theory of Probability & Its Applications, 1962, 7(2):147-163.
- [165] Vorob'ev N. Markov measures and markov extensions[J]. Theory of Probability & Its Applications, 1963, 8(4):420-429.
- [166] Garg A, Mermin N D. Detector inefficiencies in the einstein-podolsky-rosen experiment[J]. Phys. Rev. D, 1987, 35:3831.
- [167] Kujala J V, Dzhafarov E N, Larsson J A. Necessary and sufficient conditions for an extended noncontextuality in a broad class of quantum mechanical systems[J]. Phys. Rev. Lett., 2015, 115:150401.
- [168] Piltz C, Sriarunothai T, Varón A, et al. A trapped-ion-based quantum byte with 10^{-5} next-neighbour cross-talk[J]. Nat. commun., 2014, 5:4679.
- [169] Lunghi T, Brask J B, Lim C C W, et al. Self-testing quantum random number generator[J]. Phys. Rev. Lett., 2015, 114:150501.
- [170] Kwon H, Kim M. Fluctuation theorems for a quantum channel[J]. Phys. Rev. X, 2019, 9(3):031029.
- [171] Meleshkevich M, Drozhzhin A, Platonov N, et al. 10 w single-mode single frequency tm-doped fiber amplifiers optimized for 1800–2020-nm band[C]//Fiber Lasers II: Technology, Systems, and Applications: volume 5709. International Society for Optics and Photonics, 2005:117-124.

APPENDIX A

A.1 Current stabilization circuit

The trapped ion system needs a Gauss level stable external magnetic field to realize efficient Doppler cooling. Helmholtz coils are commonly used to generate the magnetic field. To make the magnetic field stable, the current noise of the coil has to be suppressed. Fig. A.1 shows a circuit used to stabilize the current of the coil. First, a sampling resistor is used to monitor the current. Then the current signal is compared with a reference signal through an operational amplifier. In the end, the output of the operational amplifier is sent to two triodes to adjust the current. This circuit can suppress current noise to less than 100 PPM at hour level time duration.

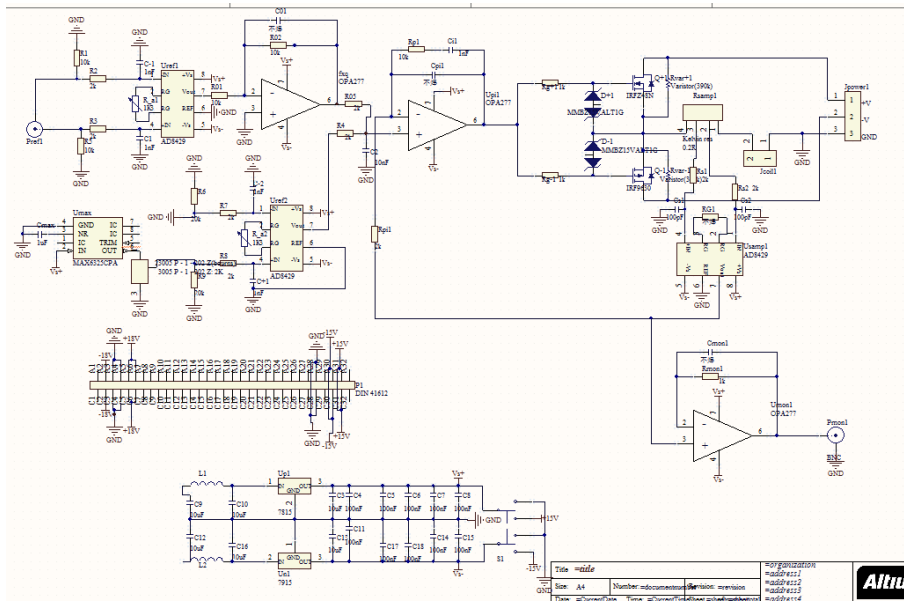


Figure A.1 Stabilized current source.

A.2 Switch of RF power

When we compensate the ion's micromotion, the trap's RF power needs to be switched between high power and low power. But it always has some chance to lose the ion when we switch the power. As shown in Fig. A.2, one of the main problems is found to be the small mechanical switch. It has a jitter problem, which is common to all mechanical switches. We solve this problem by using a shutter controller to generate the

digital signal to control the power switch. And the controller can be used in manual mode or remote mode to facilitate remote control.



Figure A.2 Mechanical manual switch and shutter controller.

A.3 1762 nm optical amplifier design

To manipulate more $^{138}\text{Ba}^+$ ions in the trap, 1762 nm laser power needs to be amplified. We design a two-step 1762 nm optical amplifier and expect to have an output of watt level. Most of the ideas came from a paper of Meleshkevich^[171]. This protocol hasn't been verified experimentally, but PreciLasers (a laser company) already have a commercial product based on a similar protocol. The structure of our amplifier design is shown in Fig. A.3. The power is first amplified to 100 mW by a BOA amplifier from Thorlabs. Then an isolator is added to prevent the reflection from the second stage amplifier. In the second stage amplifier, 1762 nm laser is first mixed with 5 W 1567 nm pump laser by a Wavelength Division Multiplexing (WDM) and then amplified through a 2.5 m long Tm-fiber. Finally, a 1567 nm grating is added to reflect the remaining 1567 nm laser to ensure that the output only have 1762 nm laser.

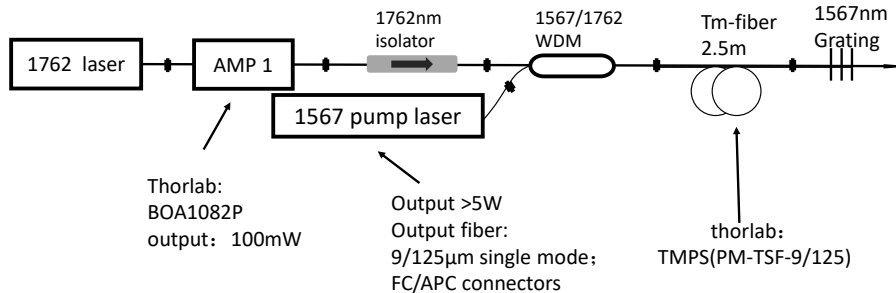


Figure A.3 Scheme for two-step 1762 nm laser amplifier.

A.4 Multi-ion's hopping problems in $^{171}\text{Yb}^+$ - $^{138}\text{Ba}^+$ system

Due to the mass difference between $^{171}\text{Yb}^+$ ion and $^{138}\text{Ba}^+$ ion, their pseudo-potentials caused by the RF electric field are different. The two needles in the four-rod trap lead to RF leakage in the axial direction. Then it also causes the axial mode frequency difference between $^{171}\text{Yb}^+$ and $^{138}\text{Ba}^+$ ions. When we have more ions in the trap, hopping between $^{171}\text{Yb}^+$ and $^{138}\text{Ba}^+$ ions is not simply position exchange. The overall structure of the ion chain will also change. As shown in Fig. A.4, there are five $^{171}\text{Yb}^+$ ions and one $^{138}\text{Ba}^+$ ion in the trap. After the $^{138}\text{Ba}^+$ hops from position 2 to position 6, position 3, 4, and 5 also have obvious shifts.

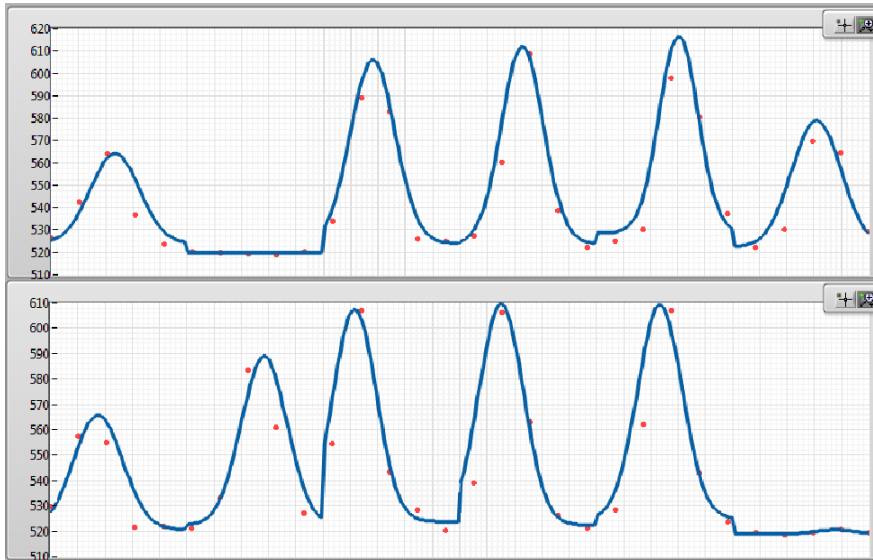


Figure A.4 Ion positions shift caused by $^{138}\text{Ba}^+$ ion hopping. The horizontal axis is the relative pixel position of each ion. The vertical axis is the count for each pixel. There are five $^{171}\text{Yb}^+$ ions and one $^{138}\text{Ba}^+$ ion in the trap. Only Yb ion counts are shown here. Five peaks correspond to five $^{171}\text{Yb}^+$ ions locations. The remain flat part is the position of $^{138}\text{Ba}^+$ ion. The $^{138}\text{Ba}^+$ ion is located at position 2 in the top figure and position 6 in the bottom figure. The data taking program has predetermined center position for each ion. Only these pixels near the center positions are shown in the figure. Some pixels between ions are not shown here.

Fig. A.5 shows the record of 4 times hopping during 20 min. It is clear that hopping of $^{138}\text{Ba}^+$ ion changes the ion chain structure a lot. One way to solve this problem is using blade or surface trap due to the fact that they don't have electrodes in the axial direction. Then the RF leakage in the axial direction will be smaller.

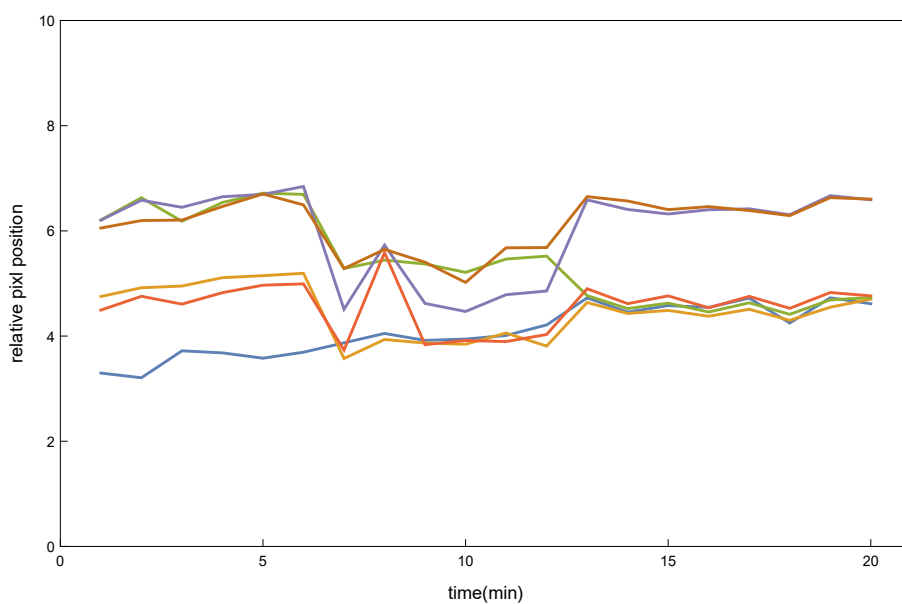


Figure A.5 Ion positions shift caused by $^{138}\text{Ba}^+$ ion hopping. There are 6 ions in the trap and one of them is $^{138}\text{Ba}^+$. The vertical axis is 6 ion's pixel positions relative to their predetermined center positions. 5 means the position of the predetermined center position. 0 means left side, and 10 means right side.

ACKNOWLEDGEMENTS

衷心感谢导师 Kihwan Kim 副教授对本人博士生涯的精心指导。他严谨的科学态度以及事无巨细的悉心培养帮助我建立了良好的科研习惯，他对学生独立学术研究能力的着重培养也让我受益匪浅。金老师除了学业和科研之外对我的个人生活也给予了很多关心和帮助，让我度过了非常欢快且有意义的五年时光。

感谢离子阱量子计算课题组的每一位同学。和你们一起分析实验问题，一同讨论科研想法，以及一块熬夜做实验的过程都是我进步的来源，感谢你们让我的生活如此丰富多彩。

感谢严马可、张君华、汪野师兄。入学初期你们对我的悉心教导让我快速地熟悉实验平台，承担实验任务。你们教会了我大部分基础的实验操作，打下了坚实的基础功，这些能力后来证明都是实验必不可少的。感谢安硕明、吕定顺、沈杨超、路尧、张宽、张帅宁等师兄在日常的答疑解惑。你们来自隔壁屋的帮助缓解了我很多接手实验室初期的压力。感谢苏晓禄、乔木、陈文涛、蔡正阳、张家梁等，你们的陪伴和日常爆梗给我带来了许多欢乐和收获。感谢栾春阳帮我分担了很多实验上的压力。你的实验习惯也让实验室更加整洁有序。感谢谢天、金乃君、黄冠豪、杜博涛、周子楠等众师弟们提供强大的辅助战斗力。感谢室友张胜同学在实验技巧上的探讨和寝室生活中的帮助。感谢张静宁、Mile Gu、袁骁、Adán Cabello 等在理论上的合作与帮助。

感谢我的父母以及爱人一直以来的支持和无私奉献。解决我的后顾之忧，让我更有动力投入到科研生活。

声 明

本人郑重声明：所呈交的学位论文，是本人在导师指导下，独立进行研究工作所取得的成果。尽我所知，除文中已经注明引用的内容外，本学位论文的研究成果不包含任何他人享有著作权的内容。对本论文所涉及的研究工作做出贡献的其他个人和集体，均已在文中以明确方式标明。

签 名： _____ 日 期： _____

RESUME

个人简历

1993年2月2日出生于河南太康县。

2012年9月考入哈尔滨工业大学物理系应用物理专业，2016年7月本科毕业并获得理学学士学位。

2016年9月免试进入清华大学交叉信息研究院攻读物理学博士至今。

在学期间完成的相关学术成果

学术论文:

- [1] **Pengfei Wang**, Chun-Yang Luan, Mu Qiao, Mark Um, Junhua Zhang, Ye Wang, Xiao Yuan, Mile Gu, Jingning Zhang, Kihwan Kim. Single ion qubit with estimated coherence time exceeding one hour. *Nat Commun* 12, 233 (2021).
- [2] Mark Um, Qi Zhao, Junhua Zhang, **Pengfei Wang**, Ye Wang, Mu Qiao, Hongyi Zhou, Xiongfeng Ma, and Kihwan Kim. Randomness Expansion Secured by Quantum Contextuality, *Phys. Rev. Applied.* 13, 034077 (2020).
- [3] Mu Qiao, Ye Wang, Zhengyang Cai, Botao Du, **Pengfei Wang**, Chunyang Luan, Wentao Chen, Heung-Ryoul Noh, Kihwan Kim. Double-EIT Ground-State Cooling of Stationary Two-Dimensional Ion Lattices. *Phys. Rev. Lett.* 126, 023604 (2021).
- [4] Ye Wang, Mu Qiao, Zhengyang Cai, Kuan Zhang, Naijun Jin, **Pengfei Wang**, Wentao Chen, Chunyang Luan, Botao Du, Haiyan Wang, Yipu Song, Dahyun Yum, Kihwan Kim. Coherently Manipulated 2D Ion Crystal in a Monolithic Paul Trap. *Advanced Quantum Technologies* 3, 2000068 (2020).
- [5] Tian Xie, Naijun Jin, Ye Wang, Junhua Zhang, Mark Um, **Pengfei Wang**, and Kihwan Kim, "Frequency stabilization of a 650 nm laser to an I2 spectrum for trapped $^{138}\text{Ba}^+$ ions," *J. Opt. Soc. Am. B* 36, 243-247 (2019).

COMMENTS FROM THESIS SUPERVISOR

1. 对论文的学术评语（论文是否由作者独立完成，有何创造性成果）：

The thesis is completed independently by Pengfei Wang with my guidance. In the thesis, he described his serious experimental works for the quantum information science with trapped ions during his Ph.D period. Wang Pengfei experimentally demonstrated the longest coherence time of a single qubit in the world among all the physical platforms, which is over an hour. Quantum coherence is a vital component for any quantum information processing including quantum computer, quantum metrology, and quantum communication. If a system loses the quantum coherence, there is no advantage of a quantum system against classical system. However, in practice, the quantum coherence is extremely fragile and it is one of the major challenges in quantum information science to maintain the coherence as long as possible. With single trapped ion-qubits, Pengfei achieved the coherence time of around 5400 seconds. Pengfei also demonstrated the entanglement between two-species of trapped ion-qubits, Yb⁺ and Ba⁺. The experimental system with two-species of ions is one of the most advanced trapped-ion systems in the world. Through the entanglement, he successfully conducted the loophole-free test of fundamental principle of quantum mechanics, quantum contextuality without locality, for the first time in the world. A quantum contextuality test can provide a solution to the problem of how can we guarantee that the system is operating in the quantum regime and governed by the principle of quantum mechanics without space-likely separated sub-components.

2. 对该博士生政治表现、基础理论、专门知识、外语水平、科研能力及学术作风的综合评语，对第 2 页主要科研成果一栏的审定意见，是否同意安排博士学位论文答辩。

Basic Theories (基础理论)

Pengfei Wang has good physics background. He has clear understanding of physics with trapped ions in both of theory and experiments.

Specialized knowledge(专门知识)

Pengfei has the specialized knowledge of quantum information science with trapped ions. He has a deep understanding in foundation of quantum mechanics.

Foreign language proficiency (外语水平)

Pengfei Wang has perfect capability in communicating and conducting research in

English. He already did the oral presentation many times in various international conferences including American Physical Society Meeting. He studied all the research materials and already published many papers in English. He also took the role of the communication author for his paper published in Nature Communications.

Research skills (科研能力)

Pengfei Wang has ability of conducting experimental research with trapped ions independently. He understands what important problems in the field are and knows what to experimentally prepare to address the problems. He can also independently conclude the project with clear experimental evidence. In particular, he is the master of laser, RF, and microwave stabilization and operation.

The validation opinion on the student's main research outcomes (主要科研成果一栏的审定意见)

During his Ph. D, Pengfei Wang has realized the longest coherence time of a single qubit in the world, which was published in Nature Communications. He also demonstrated the entanglement between two-species of trapped ion-qubits, Yb⁺ and Ba⁺ with larger than 98% fidelity. Through the entanglement, he experimentally succeeded the loophole-free test of quantum contextuality without locality, for the first time in the world. He has co-published more than 4 SCI papers with his meaningful contributions. These works clearly showed that Pengfei Wang deserves Ph. D.

Therefore, I strongly recommend the Ph. D degree of Pengfei Wang.

RESOLUTION OF THESIS DEFENSE COMMITTEE

离子阱系统在量子计算、量子模拟、量子精密测量等领域发挥着越来越重要的作用，是量子信息科学领域发展最快的系统之一。本论文选题专注于离子阱系统，具有重要的学术意义。

论文基于 $171\text{Yb}^+-138\text{Ba}^+$ 离子阱系统研究了三个重要问题，取得了如下创新性成果：

1. 将单离子量子比特的相干时间延长到一小时以上，创造了该领域的新记录，对促进通用离子阱量子计算机的实现具有重要意义。

2. 实现了 $171\text{Yb}^+-138\text{Ba}^+$ 离子间高于 98% 保真度的纠缠，该技术对于提升离子阱体系可扩展性、推动纠错算法的实验实现等至关重要。

3. 在实验上利用不同种离子间操作无串扰的优势，演示了量子互文性的无漏洞测试，实现了超过 15 个标准差的互文性不等式违背。

王鹏飞同学的博士学位论文内容丰富、书写规范、表达清楚、逻辑清晰。论文工作表明作者在离子阱量子计算领域具有坚实宽广的基础知识，具有独立从事科学研究的能力。在答辩过程中，叙述准确、条例清晰、回答问题正确。

答辩委员会认为这是一篇优秀的博士论文，经投票表决，一致同意通过论文答辩，并建议授予王鹏飞理学博士学位。